12-2010

Carbon isotopic fractionation across a late Cambrian carbonate platform: A regional response to the SPICE event as recorded in the Great Basin

Jonathan Lloyd Baker
University of Nevada, Las Vegas

CARBON ISOTOPIC FRACTIONATION ACROSS A LATE CAMBRIAN CARBONATE PLATFORM: A REGIONAL RESPONSE TO THE SPICE EVENT AS RECORDED IN THE GREAT BASIN, UNITED STATES

by

Jonathan Lloyd Baker

Bachelor of Science
Weber State University
2008

A thesis submitted in partial fulfillment of
the requirements for the

Master of Science in Geoscience
Department of Geoscience
College of Science

Graduate College
University of Nevada, Las Vegas
December 2010

UNLV
UNIVERSITY OF NEVADA LAS VEGAS

THE GRADUATE COLLEGE

We recommend the thesis prepared under our supervision by

Jonathan Lloyd Baker

entitled

Carbon Isotopic Fractionation across a Late Cambrian Carbonate Platform: A Regional Response to the SPICE Event as Recorded in the Great Basin

be accepted in partial fulfillment of the requirements for the degree of

Master of Science in Geoscience

Ganquig Jiang, Committee Chair

Matthew Lachniet, Committee Member

Rodney Metcalf, Committee Member

Peter Starkweather, Graduate Faculty Representative

Ronald Smith, Ph. D., Vice President for Research and Graduate Studies
and Dean of the Graduate College

December 2010

ABSTRACT

Carbon Isotopic Fractionation Across A Late Cambrian Carbonate Platform: A Regional Response To The SPICE Event As Recorded In The Great Basin, United States

by

Jonathan Lloyd Baker

Dr. Ganqing Jiang, Examination Committee Chair
Associate Professor of Geoscience
University of Nevada, Las Vegas

Geochemical models have suggested that the late Cambrian was characterized by a greenhouse climate with high pCO_2. Furthermore, stable-isotope analyses within the Great Basin have documented a large carbonate isotope ($\delta^{13}C_{carb}$) excursion, known as the Steptoean Positive Carbon Isotope Excursion (SPICE). This event has been documented globally, and is interpreted as having resulted from enhanced organic carbon burial. Unless the size of carbon reservoirs in the Cambrian ocean was significantly different from those of the Cenozoic, this forcing should have resulted in a comparable carbon-isotope excursion in organic matter ($\delta^{13}C_{org}$). It is also predicted that increased organic carbon burial would lower atmospheric CO_2, which may cause global cooling and a reduction in carbonate-organic carbon isotope fractionation. To test these predictions, paired carbonate and organic carbon isotope data are reported here from carbonate stratigraphic sections at Shingle Pass, Nevada and in House Range, Utah. At Shingle Pass, $\delta^{13}C_{org}$ values record a positive excursion that roughly mirrors $\delta^{13}C_{carb}$ values at a similar magnitude, suggesting an oceanographic control on the carbon isotope trend. In the House Range section,

although $\delta^{13}C_{org}$ values show a rough positive shift associated with positive $\delta^{13}C_{carb}$, the magnitude is smaller and values show minor shifts across the excursion. However, constructing a time-equivalent overlay of data from both sections using key stratigraphic boundaries resolved apparent discrepancies, suggesting a regional control on carbon isotopic fractionation. The difference between carbonate and organic carbon isotope values ($\Delta^{13}C = \delta^{13}C_{carb} - \delta^{13}C_{org}$) averages 27‰ to 28‰ in both sections, but increases to 30‰ at the peak of the excursion and falls to as low as 25‰ immediately after the Sauk II/III sequence boundary. Temporal variations in $\Delta^{13}C$ do not follow the predicted atmospheric CO_2 changes before the $\delta^{13}C_{carb}$ peak of the SPICE, as might have been derived from the increased organic carbon burial model for the origin of the SPICE event, and indicates that the carbon isotope fractionation was less sensitive to atmospheric CO_2 changes when ambient CO_2 was high. The abrupt drop in $\Delta^{13}C$ after the $\delta^{13}C_{carb}$ peak of the SPICE is consistent with low atmospheric CO_2 and the potential evolution of photosynthetic organisms in adapting to CO_2-limited environments with stronger bicarbonate uptake during carbon fixation.

ACKNOWLEDGEMENTS

Foremost, I would like to thank my advisor, Dr. Ganqing Jiang, for introducing me to the discipline of chemostratigraphy and the problems related to this thesis. Through much patience and diligence, you have remained devoted to my progress beyond what I deserved. Moreover, you have inspired me to pursue my academic goals with confidence, though in a spirit of humility and self-awareness that will never leave me. Above all, you have always taught me to stay happy and healthy, regardless of the challenges that face me.

I am grateful to the Department of Geoscience at UNLV for the opportunity to study in such a unique environment, replete with camaraderie and a healthy zeal for scientific endeavor. In particular, I would like to thank Dr. Andrew Hanson, both for introducing me to the department and for helpful discussions concerning the strength of my data. Thank you also to Dr. Margaret (Peg) Rees for spending many days guiding me through the field area and offering your expertise and direction in the early stages of this manuscript. Additionally, I would like to recognize the other members of my advisory committee — Dr. Matt Lachniet, Dr. Rod Metcalf, and Dr. Peter Starkweather — for the time and effort spent reviewing this project and providing vital feedback toward the completion thereof. I greatly appreciate your support, and the time vested to discussing various topics related to this thesis on an individual basis.

It has thus far been an honor to be a part of the “Carbonate Mafia”, and I am especially thankful to fellow members thereof. To Adam “Cycle Master” Zeiza and Ratna “Wiwid” Widiarti, I am indebted to you both for your assistance in the

field, without which I could not have completed this project. I thank you also for sharing your expertise, and believe that your passion and discipline have made me a better field researcher. Thank you to Swapan Sahoo and Bobby Henry for assistance and motivation during laboratory analyses, as well as many helpful discussions in the interpretation of my data.

Special thanks goes to my undergraduate advisor, Dr. Jeff Eaton, whose unrivaled passion for field research originally inspired me to pursue a graduate degree, and whose confidence in my success proved a turning point when I doubted myself. Thanks also to my good friend Matthew Weinstock, who has taught me more than anyone what it means to be a scientist and a researcher, and to Samuel Emadi, who has never failed to remind me that no matter how busy or overwhelmed I think I am, I am simply not.

Last, but not least, I wish to thank my beautiful wife, Natasha, for her unfailing love, care, and affection, but especially for her sacrifice when I have often been present in body, though absent in spirit. You have lifted me up and given me ample motivation to pursue my goals. *Bol'shoe spasibo, dorogaya Natusya.*

This thesis was made possible through funding from the Department of Geoscience at UNLV, the Geological Society of America, the Nevada Petroleum Society, and Dr. Ganqing Jiang. Special thanks also to Dr. Adolph Yonkee for providing equipment for petrographic analysis at Weber State University.

TABLE OF CONTENTS

LIST OF FIGURES

CHAPTER 1

INTRODUCTION

Major perturbations to biogeochemical cycles, such as the oxygen and carbon cycles, have resulted in pronounced shifts in Earth's atmospheric composition and are often associated with major extinctions of organisms (e.g. Palmer, 1984; Saltzman et al., 2000), as well as global warming and cooling events. However, the relationships between perturbations and their forcing mechanisms are poorly understood, due to the complex interactions of the climate and biosphere, as well as the challenge of obtaining pristine geochemical data. Carbonate rock sequences have been used to document physiogeographic changes in Earth history, such as the expansion of carbonate shelves (e.g. Palmer, 1974) and sea level change (e.g. Catuneanu et al., 2009), while many studies have analyzed the isotopic signature of carbonate rocks.

Stratigraphic variations in the carbon isotope composition of sedimentary organic matter and carbonates record long-term changes in seawater isotope composition in response to perturbations of the global carbon cycle. While carbonate carbon isotopes ($\delta^{13}C_{carb}$) record $\delta^{13}C$ of dissolved inorganic carbon (DIC) in the ocean, organic carbon isotopes ($\delta^{13}C_{org}$) record isotope fractionation during carbon fixation by primary (photosynthetic) and secondary (e.g. chemoautrophic and methanotrophic) producers (Hayes et al., 1999). In the modern ocean, the majority of the ocean water column is oxygenated so that secondary carbon fixation is limited. Thus organic matter in the ocean is mostly produced by photosynthetic organisms. Because photosynthetic organisms use

dissolved CO_2 in seawater (which is equilibrated with atmospheric CO_2) during carbon fixation, the carbon isotope composition of organic matter ($\delta^{13}C_{org}$) reflects carbon isotope fractionation during photosynthesis in response to productivity and CO_2 concentration (Hayes et al., 1999; Kump and Arthur, 1999). Thus paired $\delta^{13}C_{carb}$ and $\delta^{13}C_{org}$ analyses of carbonate successions have been widely used in paleoceanographic and paleoclimate studies to track changes in atmospheric CO_2 and primary productivity, particularly across the major events in the geological history (e.g. Beerling et al., 2002; Riccardi and Kump, 2007; Cramer and Saltzman, 2007).

The late Cambrian was a unique time interval in Earth history, being characterized as a super-greenhouse time period with atmospheric CO_2 level possibly exceeding 4,500 ppm (Berner, 2001, 2003), and also preceding the great Ordovician biodiversification event. Furthermore, a large carbonate carbon isotope ($\delta^{13}C_{carb}$) excursion, known as the Steptoean Positive Carbon Isotope Excursion (SPICE), has been documented from global successions, recording a 2-4 m.y. disruption in the global carbon cycle (Saltzman et al., 1998). The 4‰ to 5‰ positive shift in $\delta^{13}C_{carb}$ has been interpreted to be the result of enhanced organic burial, which removes ^{13}C-depleted organic carbon from the reactive carbon pool of the ocean and atmosphere. In general, if increased organic carbon burial causes a positive shift in $\delta^{13}C_{carb}$, a parallel positive shift in carbon isotopes of organic matter ($\delta^{13}C_{org}$) would be expected, as well as a significant reduction in atmospheric carbon dioxide and a pulse of oxygen to the ocean-atmosphere system (Kump and Arthur, 1999). Consequently, the positive

excursion may have been followed by a significant reduction in global temperatures. However, these predictions have not been adequately tested with regard to the SPICE event. My thesis research attempts to use paired carbonate and organic carbon isotope analyses ($\delta^{13}C_{carb}$ and $\delta^{13}C_{org}$) to characterize the $\delta^{13}C_{org}$ trend across the SPICE event, to test model predictions with regard to the proposed forcing mechanism, and to discuss the biotic and climatic response to the SPICE event.

CHAPTER 2

GEOLOGIC BACKGROUND

2.1 Overview of field localities within this study

Samples were taken from two measured Cambrian sections within the Great Basin (Figure 1): 1) Shingle Pass, southern Egan Range, Nevada; and 2) Orr Ridge, southern House Range, Utah. Saltzman et al. (1998) documented the SPICE event at both localities, providing a clear guide in sampling the intended interval for organic carbon isotopes. Deposition was relatively continuous during the Steptoean stage (Hintze and Palmer, 1976; Rowell and Brady, 1976), and biostratigraphically, both sections are well constrained and complete in comparison to other North American localities (Lochman-Balk, 1974; Saltzman, 1999). Thus both sections are ideal for investigating biogeochemical trends in Upper Cambrian strata of North America.

2.1.1 Shingle Pass

At Shingle Pass, Cambrian rocks are exposed within a faulted horst block located 3 km east of U.S. Highway 318 and approximately 18 km south of Lund, NV. Middle-Upper Paleozoic rocks are exposed at the north end of the horst block, where the Patterson Pass Road cuts into the range. Our section begins 0.6 miles south of this road (Fig. 1), where the block is significantly less deformed than near the road. The base of our section at Shingle Pass lies ~40 meters above the boundary between the A and B members of the Emigrant Springs Formation (Fig. 2), which Saltzman et al. (1998) considered to be the base of the Pterocephaliid biomere. The 302-meter section traverses a series of oolitic-

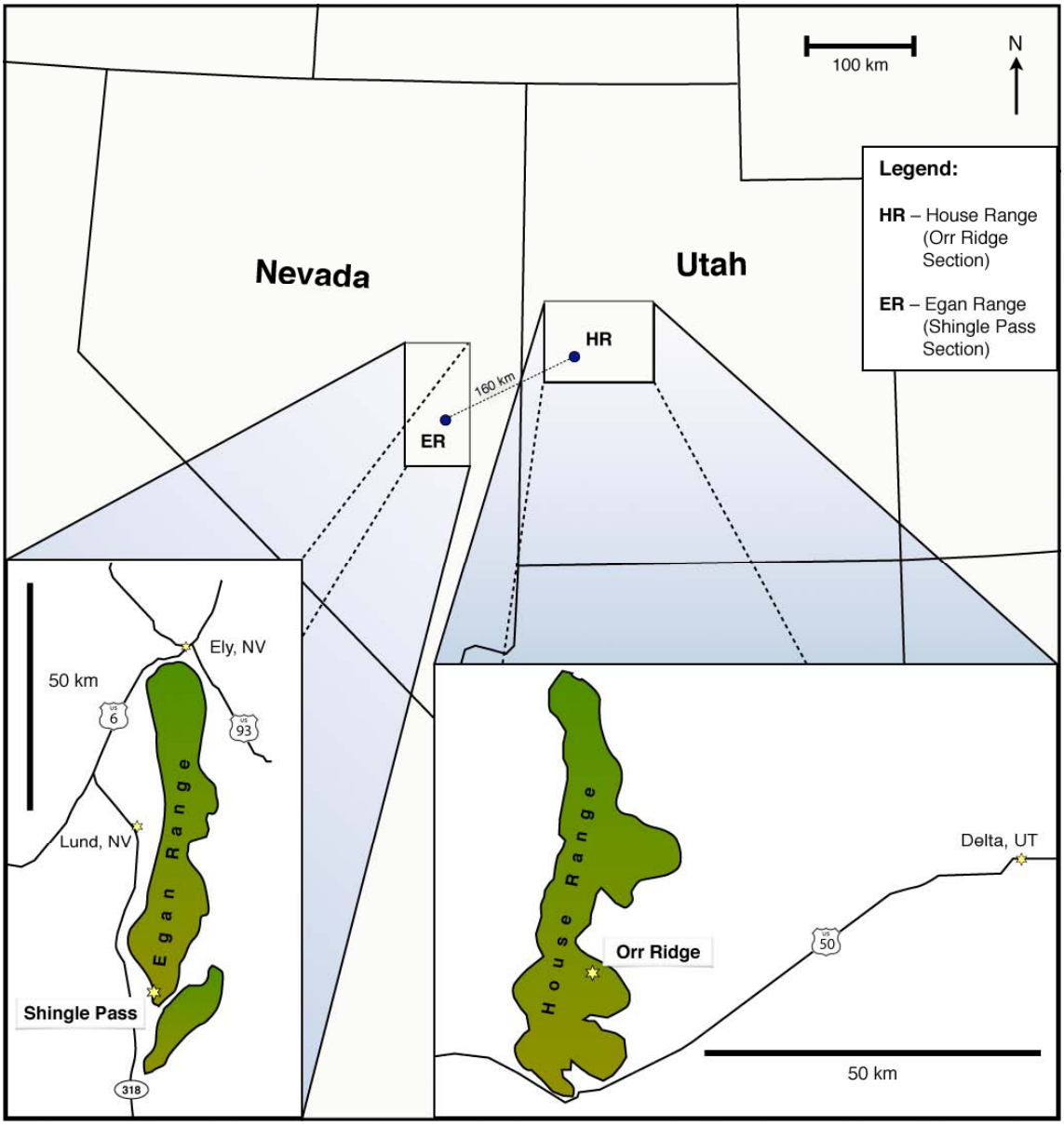

Figure 1: Map showing location of field sections within this study from the Great Basin.

grainstone cliffs, which are comprised of the uppermost Emigrant Springs Formation, before following a steep wash that cuts through the fine-grained limestone facies of the Dunderberg Formation. The wash transitions sharply to a canyon surrounded by steep dolomitic walls of the lower Whipple Cave Formation, where the section terminates. Distinct mudcracks are present in wavy

laminated boundstone at 302 meters, and define the top of the Shingle Pass section.

2.1.2 House Range

The southern edge of the House Range is easily seen from U.S. Highway 50, approximately 40 miles west of Delta, UT. Our section was taken along Orr Ridge (Fig. 1; Hintze and Palmer, 1976), which marks the southwestern boundary of Little Horse Canyon, a gentle-sloping catchment that opens to the eastern edge of the House Range. The base of our section lies several meters above a laterally continuous, stromatolitic horizon, and 21 meters below the boundary between the Big Horse Limestone and Candland Shale members of the Orr Formation. This boundary also marks the base of the Pterocephaliid biomere (Saltzman et al., 1998). The 340-meter section follows the ridgeline and terminates within the Sneakover Limestone member of the Orr Formation, where the upper *Elvinia* trilobite subzone marks the end of the Pterocephaliid biomere (Rees et al., 1976).

2.2 Paleogeography and sedimentary framework

While the depositional record of the rocks comprising stratigraphic successions within the Great Basin is complex (e.g. Dickinson, 2006), the lower Paleozoic record is remarkably continuous, and constitutes an ideal setting to test hypotheses concerning long-term disruptions in marine cycles. Using data from the Great Basin, Saltzman (2005) compiled a globally correlated Paleozoic carbon-isotope record. Nonetheless, interpreting paleogeographic features such

as the House Range Embayment (Fig. 2) and the complex structural and diagenetic history of the Great Basin provides key challenges to interpreting carbon-isotopic records.

Following the breakup of the Rodinian supercontinent ~750 Ma, and subsequent rifting from Baltica ~600 Ma, the North American craton (Laurentia) drifted toward an equatorial position (Torsvik et al., 1996), where it remained for much of Paleozoic time. By the onset of the Middle Cambrian, the western Laurentian margin was characterized by a north-south trending passive margin, wherein carbonate production dominated the low-latitude, shallow-shelf environments (Kellogg, 1963). Thermally driven subsidence continued through the Cambro-Ordovician transition (Bond et al., 1983) until the Devonian (Lund, 2008) with the emergence of the Antler allochthon, resulting in a relatively conformable record of the Lower Paleozoic margin. The basin was likely unrestricted and well-mixed with global ocean reservoirs, as the margin represents a distally steepened ramp (Osleger, 1991a). One exception to this model is the House Range Embayment, an east-

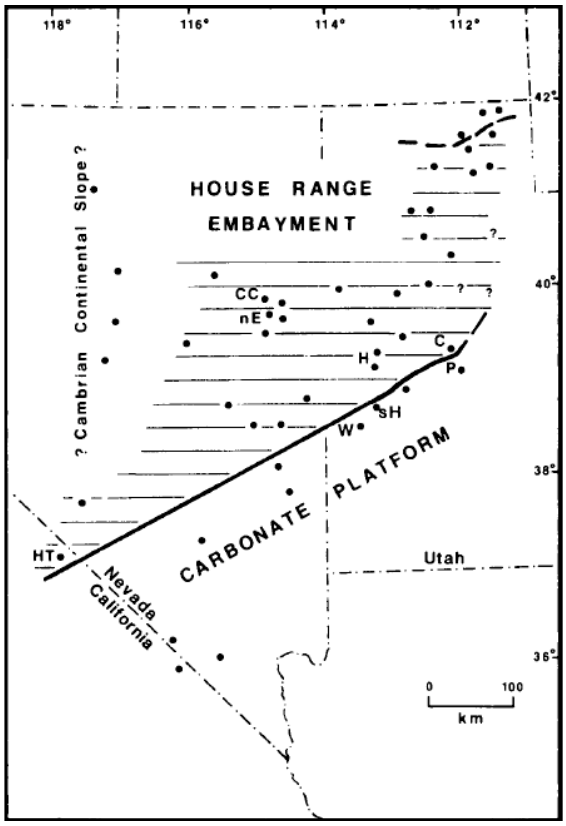

Figure 2: From Rees (1986); extent of the House Range Embayment. Bold line shows approximate strike of the normal fault bounding the half-graben structure.

west trending reentrant amid the platform (Rees, 1986; Fig. 2), in which both sections from this study are located. Therefore, it is imperative to carefully consider the local depositional framework before considering respective carbon isotope records as global representatives of the Cambrian ocean.

Rees (1986) documented the geographic pattern of Middle Cambrian sections dominated by deep-water facies, which comprise the House Range Embayment. The zone is triangular, opening to the west (basinward). Paleobathymetrically, it deepens to the south and defines a southwest-striking boundary, which has been interpreted to represent a normal fault zone that is parallel to the Mina transform zone in southwestern Nevada (Lund, 2008). Therefore, deposition within the House Range Embayment would have been partially fault-controlled during the Middle Cambrian. While the paleobathymetric contrast between sections across this boundary peaks in the middle Cambrian, its influence on depositional facies seems to have diminished into the late Cambrian. The diminished contrast is evident at Patterson Pass within the Emigrant Springs Formation, the lowermost member of which encompasses the Middle-Upper Cambrian boundary, where oolitic and bioclastic grainstones commonly cap carbonate cycles, even into the Dunderberg Shale (Kellogg, 1963). Furthermore, Cook and Taylor (1977) interpreted the lowermost Whipple Cave Formation as representing shallow-water shelf facies — a stark contrast to the distal shelf facies of the Patterson Pass Shale and Member A of the Emigrant Springs Formation. The shallowing trend of lithofacies is evident in the Upper Cambrian strata of the House Range, where the Orr Formation is dominated by

shallow subtidal facies, or carbonate-capped shaly cycles (Osleger, 1991b), indicating a possible infilling of the trough from enhanced carbonate production rates or decreased movement along the fault. However, carbonate-siliciclastic transitions are present at the base of the Candland Shale and Corset Springs members of the Orr Formation and may represent periods of renewed tectonic subsidence, during which the House Range Embayment could have acted as a sediment bypass for terrigenous siliciclastic sediments (Osleger, 1991a). The John's Wash Limestone is a shallow-subtidal to supratidal carbonate interval amid the deeper-water facies of the Candland Shale and Corset Springs Shale members that bound it (Rees et al., 1976). This 40 to 80-meter carbonate interval, which is absent to the northeast (Wah Wah Mountains) and to the south (Steamboat Pass), has been interpreted to record the growth and westward progradation of oolitic shoals (Rees et al., 1976). Evans (1997) reported a biostratigraphic hiatus during the Dunderbergia zone at Steamboat Pass, which is not missing at the Wah Wah Mountains section of Rees et al. (1976). This implies differential subsidence within the House Range embayment immediately following the Sauk II/III sequence boundary, and may have been the result of renewed tectonic activity.

Rapid, lateral variability in shallow-water facies is common throughout the Upper Cambrian section, and may represent the migration of localized depositional environments across a remarkably flat platform (Kepper, 1969; Rees et al., 1976). Progradation of facies across the shelf was likely driven by a temporary reduction in thermal subsidence (Bond et al., 1988). Although a

combination of autocyclic mechanisms may provide the favorable interpretation for a shallow-water depositional framework, a regional disconformity is present at the Dresbachian-Franconian boundary (Osleger and Read, 1993), which is expressed in both field sections by thrombolitic and algal boundstone facies that comprise the cycle top. The stage boundary also represents the Sauk II/III sequence boundary (Palmer, 1981) and a craton-wide sea level minimum. Since falling sea level can enhance nutrient delivery to the oceans and increase the carbon isotopic composition of riverine carbon inputs (Saltzman et al., 2000), the sequence boundary should carefully considered when interpreting the paired carbon isotope record of the Great Basin.

2.3 Steptoean stage nomenclature, biostratigraphy, and relation to trilobite extinction

The Steptoean stage of the Late Cambrian was proposed and defined by Ludvigsen and Westrop (1985) in order to replace the rather arbitrary and obsolete Dresbachian and Franconian stages. It is roughly equivalent to the Pterocephaliid biomere (Palmer, 1998) and Furongian Series (Peng et al., 2004), which includes the *Aphelaspis*, *Dicanthopyge*, *Prehousia*, *Dunderbergia*, and lower *Elvinia* trilobite zones (Palmer, 1965b). The lower stage boundary is marked by the sharp transition between the *Crephicephalus* and *Aphelaspis* trilobite zones of North America, which can be globally correlated by the first appearance of *Glyptagnostus reticulatus* (Palmer, 1998; Zhu et al., 2004).

Palmer (1962) noted that the oldest units containing *Aphelaspsis* also represent the most distal marine settings, perhaps indicating a shallow-shelf invasion by deep-water species. Such an invasive migration may have also been driven by shifting ocean chemistry or global cooling (Ahlberg et al., 2009), since the direction is counterintuitive to migratory patterns of deep-water fauna during sea-level fall later in the stage. Furthermore, no evidence of faunal turnover has been documented in shallow-water settings associated with the Sauk II/III sequence boundary (i.e. maximum regression and reflooding of the continent), which is present within the Steptoean stage (Palmer, 1981). On the contrary, the Sauk II/III boundary is coincident with maximum faunal diversity during the Steptoean stage (Rowell and Brady, 1976). Trilobite extinction in response to shifting ocean chemistry is consistent with carbon isotopes, which begin to shift positive at the global appearance of *G. reticulatus* (Saltzman et al., 2000), but the physical connection remains uncertain outside of further chemostratigraphic investigation of the SPICE interval in deeper-water stratigraphic sections.

The Steptoean stage ends at the First Appearance Datum (FAD) of the *Irvingella major* subzone within the *Elvinia* trilobite zone, which marks the onset of Laurentian transgression (Ludvigsen and Westrop, 1985), an additional faunal turnover in Laurentian trilobites (Palmer, 1965a), and the end of the SPICE event (Saltzman et al., 2000). Saltzman et al. (1995) documented a 1.5‰ positive excursion in $\delta^{13}C_{carb}$ at this interval in Great Basin sections, the magnitude of which diminishes east toward Wyoming (landward). While they attribute the apparent isotopic gradient to differential expression of the unconformity

associated with platform drowning, the excursion is interpreted to represent enhanced burial from renewed production, which may have resulted from oceanic overturn of nutrient-rich waters during shelf-wide transgression. Thus extinction events at both boundaries of the Pterocephaliid biomere are marked by productivity-driven ocean anoxia and subsequent positive carbon isotope excursions (Saltzman et al., 1995; Saltzman, 1999).

Auerbach (2004) documented a trace-elemental enrichment in nearshore, lingulid brachiopods over the SPICE interval, accompanied by a 6-10 fold increase in toxic metals, perhaps suggesting a poisonous aspect to bounding extinction events. However, the period of maximum toxicity, attributed to shelf exposure during regression, occurs between extinction events, which are associated with rapid sea-level rise (Saltzman et al., 1995). Nonetheless, such a shift in nearshore chemistry may have had detrimental implications for primary oceanic production during the SPICE event.

CHAPTER 3

BACKGROUND ON CARBON ISOTOPES AND PALEOCLIMATE

3.1 Applicability of paired carbon isotope analysis to paleoclimatology

Kump and Arthur (1999) emphasized consideration of $\delta^{13}C$ from both carbonate and organic matter when interpreting isotopic excursions, given the variability of $\Delta^{13}C$ (Fig. 3; $\Delta^{13}C = \delta^{13}C_{carb} - \delta^{13}C_{org}$) in the Phanerozoic record (Hayes et al., 1999) and its potential relationship to atmospheric composition (Arthur et al., 1988; Freeman and Hayes, 1992). The $\delta^{13}C_{carb}$ value records the isotope composition of Dissolved Inorganic Carbon (DIC = HCO_3^- + $[CO_2]_{aq}$ + CO_3^{2-}), in which $[CO_2]_{aq}$ is the dissolved CO_2 in surface ocean seawater and is

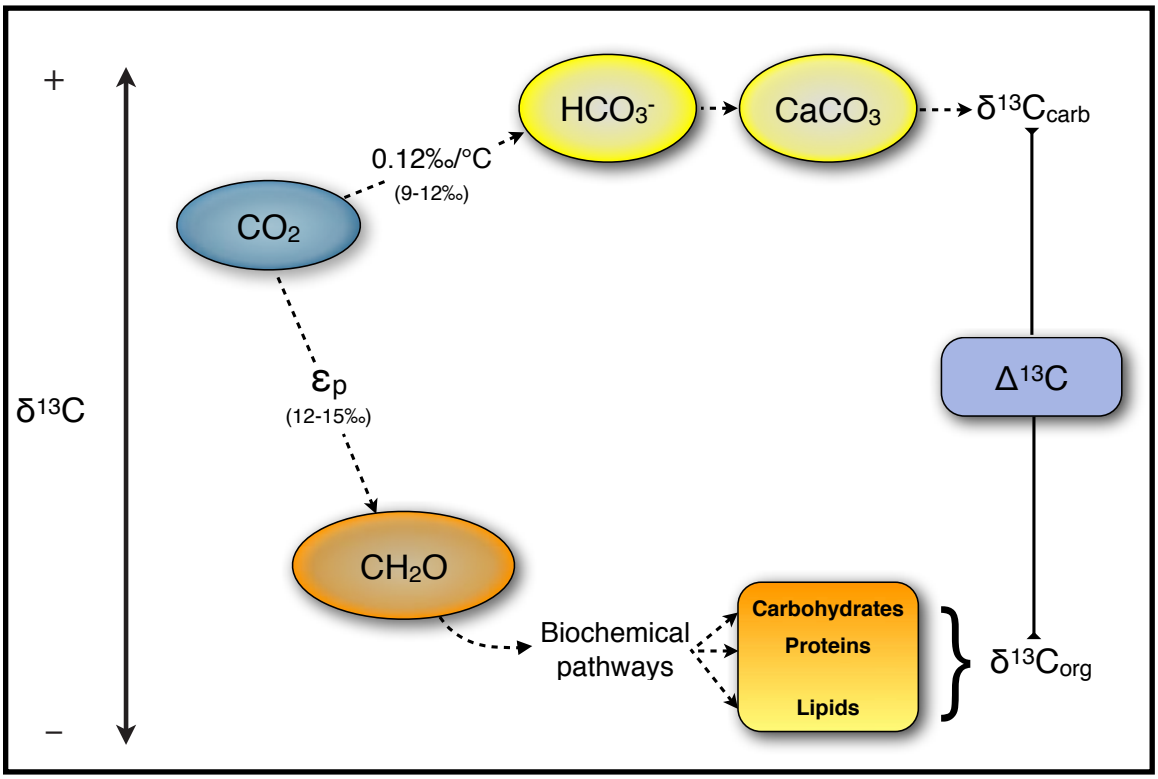

Figure 3: Simplified schematic showing distribution of carbon isotopes through various pathways, from aqueous CO_2 to preserved carbonate and organic carbon (after Hayes et al., 1999). ε_p = carbon isotopic fractionation associated with photosynthesis.

equilibrated with atmospheric CO_2 in the surface ocean. Photosynthetic organisms (commonly referred to as primary producers) use $[CO_2]_{aq}$ during carbon fixation and the resulting organic matter records isotopic composition of $[CO_2]_{aq}$ plus the isotopic fractionation during photosynthesis (ε_p). Ideally, if the isotope fractionation of primary producers remains at a constant value, $\delta^{13}C_{org}$ would covary with $\delta^{13}C_{carb}$ with a constant offset, meaning that $\Delta^{13}C$ would be a constant.

The carbon isotope fractionation of primary producers during photosynthesis, however, is variable and dependent on a number of factors such as the $[CO_2]_{aq}$ concentration and the dominant biological species in particular depositional environments. When $[CO_2]_{aq}$ is high, photosynthetic organisms would use $[CO_2]_{aq}$ through a diffusive pathway during carbon fixation (commonly referred to as the Calvin cycle) and the fractionation (ε_p) through this process would be close to 25‰. When the $[CO_2]_{aq}$ is low, organisms would not have sufficient $[CO_2]_{aq}$ for carbon fixation and are forced to take more carbon from HCO_3^- (commonly referred to as CCM–Carbon Concentration Mechanism, Raven et al., 2008a). Because the carbon isotope composition of HCO_3^- is 8.2‰ (at 30ºC) to 11.6‰ (at 0ºC) less negative than co-existing $[CO_2]_{aq}$ in seawater, primary producers that have taken more HCO_3^- as their carbon source would produce organic matter with higher $\delta^{13}C_{org}$ and lower $\Delta^{13}C$.

The $[CO_2]_{aq}$ concentration in seawater is controlled by the atmospheric CO_2 concentration and primary productivity. Higher atmospheric CO_2 would certainly result in higher $[CO_2]_{aq}$ in seawater, leading to higher diffusive CO_2

uptake by photosynthetic organisms and lower $\delta^{13}C_{org}$ of organic matter. Higher primary productivity uses more $[CO_2]_{aq}$ and resulting in $[CO_2]_{aq}$ deficit in seawater, forcing photosynthetic HCO_3^- uptake. Consequently, higher primary productivity would result in higher $\delta^{13}C_{org}$ and lower $\Delta^{13}C$ values of organic matter.

Carbon isotope fractionation is also controlled by physiological variations of photosynthetic organisms, including their growth rate, cellular volume, surface area, and ability to concentrate CO_2, as expressed by the following equation (Popp et al., 1998):

$$\varepsilon_p = 25.3 - 182(\mu/C_e)(V/S)$$

Where ε_p is the isotope fractionation (in ‰); 25.3‰ is the isotope effect associated with fixation of carbon; μ is the specific growth rate (per day); V/S is the cellular volume/surface area ratio (μm); and C_e is the concentration of dissolved CO_2 (μmol/kg). Therefore, organisms that grow under nutrient-limited conditions or have lower V/S ratios (e.g., small phytoplankton) would have a larger carbon isotope fractionation and produce organic matter with lower $\delta^{13}C_{org}$.

Despite the complex control on $\delta^{13}C_{org}$ of organic matter (and thus $\Delta^{13}C$), statistical review of the isotope record in geological history indicates that long-term changes in $\delta^{13}C_{org}$ and $\Delta^{13}C$ may be primarily controlled by changes in atmospheric CO_2 and productivity (Hayes et al., 1999). Variations in phytoplankton ecological structure of particular environments or over a certain time interval may add noise to the long-term trends of $\delta^{13}C_{org}$ and $\Delta^{13}C$, but do

not change the global pattern. Therefore, one may use $\Delta^{13}C$ as a proxy for atmospheric CO_2 at the time of deposition (Bidigare et al., 1997).

Variations of this proxy have been used to estimate the response of atmospheric CO_2 to climatic shifts in the Cenozoic (e.g. Jasper et al., 1994; Pagani, 2002) and Mesozoic (e.g. Price, 2010; Damsté et al., 2008). However, these studies often focus on individual biomarkers to constrain taxa-dependent controls on fractionation, which arise from cell diameter and structure, specific pathway of carbon fixation, and growth rate (Bidigare et al., 1997; Hayes et al., 1999). When carbon isotope values are obtained from rocks older than the Mesozoic, this atmospheric proxy becomes increasingly complicated and uncertain, which is evident in the wide range of values (10-200 times modern pCO_2) estimated for the Mesoproterozoic, based on Secondary-Ion Microprobe Spectroscopy (SIMS) analysis of carbonate and organic carbon isotopes in individual microfossils (Kaufman and Xiao, 2003). Despite this limitation, however, it may be possible to track relative shifts in atmospheric CO_2 over time if other variables can be constrained or estimated (Kump and Arthur, 1999).

3.2 Organic carbon contribution from secondary producers

In addition to the complexity of processes governing the variation in organic carbon isotope values from primary producers, organic biomass contribution from secondary producers also contributes to $\delta^{13}C_{org}$ of total organic matter. Secondary producers include heterotrophic organisms and chemoautotrophic/ methanotrophic organisms. These organisms are more common in anoxic

environments, but in the open ocean where the seawater is well-ventilated and oxygenated, primary producers dominate. Thus in restricted environments such as the shelf lagoon, isolated basins and lakes, secondary producers may make a significant biomass contribution to the total organic matter and change the $\delta^{13}C_{org}$ values. Organic matter produced by heterotrophic organisms is commonly ^{13}C-enriched relative to those of oxygenic photosynthesizers (Hayes et al., 1983; Teece and Fogel, 2007). Chemoautotrophic organisms including sulfur oxidizing bacteria use recycled carbon during carbon fixation and their biomass is up to 15‰ lower in $\delta^{13}C$ relative to primary photosynthate (Hollander and McKenzie, 2001). Methanotrophic bacteria assimilate carbon from ^{13}C-depleted methane and their biomass can be ^{13}C-depleted relative to photosynthetic organic matter by −15‰ to −40‰ (Summons et al., 1998). Thus the increase of chemoautotrophic and methanotrophic biomass contribution to TOC would significantly low the $\delta^{13}C_{org}$ of sedimentary organic matter and increase $\Delta^{13}C$.

3.3 Local environmental controls on carbon isotopic values

Local environmental controls may significantly affect both $\delta^{13}C_{carb}$ and $\delta^{13}C_{org}$ values. For example, the modern Florida Bay records $\delta^{13}C_{carb}$ 1‰-2‰ lower than the open ocean (Patterson and Walter, 1994), reflecting a higher influence of respired CO_2, while Pufahl et al. (2006) documented $\delta^{13}C_{carb}$ 0.5‰-1‰ higher than open marine values in a Miocene epeiric sea, reflecting semi-restricted exchange and more effective organic carbon burial. A combination of similar paleoceanographic factors produced ~4‰ variations in

$\delta^{13}C_{carb}$ between coeval Ordovician carbonates, which spanned an area of more than 150,000 km^2 across the midwestern United States (Panchuk et al., 2006). In a recent study, Lara et al. (2010) documented a 20‰ gradient in $\delta^{13}C_{org}$ values of marine particulate organic matter from the Argentine shelf to open Antarctic ocean waters. The steady decrease in $\delta\ ^{13}C_{org}$ was positively correlated to temperature, which enhances CO_2 solubility and hence isotopic fractionation (Hayes et al., 1999), and nutrient supply.

The importance of having a clear regional, stratigraphic and sedimentological framework alongside a chemostratigraphic analysis becomes evident in light of these factors. Major carbonate-siliclastic transitions and shifts in carbonate facies, for example, may suggest changes in carbonate production and water depth associated with regressive surfaces. Furthermore, the regional stratigraphic framework, as determined by correlating multiple sections in the same basin, may help substantiate the validity of our assertion that the basin was well mixed with the open ocean, or otherwise suggest susceptibility of carbon isotopes to the effects of semi-restricted basins (e.g. Young et al., 2008).

3.4 Diagenetic modification of $\delta^{13}C$

While chemostratigraphic studies provide compelling evidence for the robust nature of the marine carbon isotope record (e.g. Kump, 1991; Kump and Arthur, 1999; Zhu et al., 2004), diagenesis plays a significant role in the isotopic homogenization of carbonate components (González and Lohmann, 1985). Thus many authors have characterized the ^{13}C-depletion effect of early diagenesis on

carbonate sequences, particularly at exposure surfaces (e.g. Allan and Matthews, 1982) and sequence boundaries (e.g. Burns et al., 2005), which occurs through interactions with soil-gas CO_2 and meteoric fluids.

The isotopic composition of various stages of carbonate cements can vary substantially (Ali, 1995), as the fluid source ranges from meteoric (low $\delta^{13}C$) to microbially mediated pore waters (^{13}C-enrichment). However, Kaufman et al., (1991) noted that although heterogeneity can exist across carbonate grains and meteoric cements, the $\delta^{13}C$ variation is relatively insignificant (less than 1‰) when considering whole rock values. Decreasing water temperature, resulting from increasing water depth, contributes to heavier $\delta^{18}O$ values for carbonate components during cementation, but has no significant effect on $\delta^{13}C$ (Frank and Bernet, 2000).

Although the preferential chemical breakdown of labile organic compounds in the water column results in ^{13}C depletion of the residual POM (Prahl et al., 1997), thermal degradation of organic matter (including methanogenesis) in during burial (Tang et al., 2005) and the addition of heterotrophic biomass often effectively negate this process (Schouten et al., 1997; Chen et al., 2008). The degree of thermal maturation is difficult to assess in organic-poor carbonate rocks, but significant covariation of $\delta^{13}C_{org}$ with TOC may imply a dependence of the isotopic value on the degree of kerogen maturation. Furthermore, stability in C/N elemental ratios near the Redfield ratio (6.6:1) may imply low alteration as the chemical breakdown of particulate organic nitrogen (PON) contributes to the preferential removal of nitrogen-rich, labile substances such as amino acids and

proteinaceous compounds, effectively increasing the atomic C/N ratio of residual organic matter (Chen et al., 2008).

CHAPTER 4

PREVIOUS WORK

4.1 Global documentation of the SPICE event

The $\delta^{13}C$ record of the Paleozoic is relatively stable, with the exception of intermittent positive excursions (Saltzman, 2005). Since Brasier (1993) first recognized a ~4‰ positive $\delta^{13}C_{carb}$ excursion in Late Cambrian sediments, the SPICE event has been documented throughout the Great Basin (Saltzman et al., 1998) and numerous other North American localities (e.g. Glumac and Walker, 1998; Saltzman et al., 2004; Cowan et al., 2005); across various continents (e.g. Lindsay et al., 2005; Kouchinsky et al., 2008; Sial et al., 2008; Zhu et al., 2006),

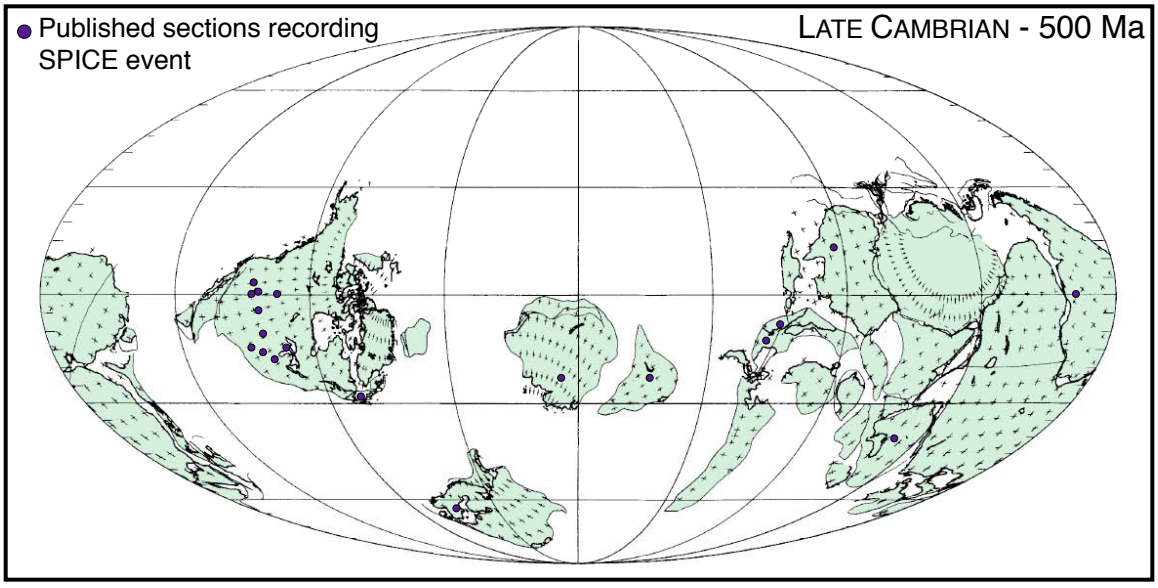

Figure 4: Global documentation of the SPICE event, modified from Scotese and McKerrow (1990), showing paleolocalities of sections from: Sweden (Ahlberg et al., 2009), France (Álvaro et al.,2008), Colorado (Brasier, 1993), Missouri, Minnesota, and Wisconsin (Cowan et al., 2005), Tennessee (Glumac and Walker, 1998), Siberia (Kouchinsky et al., 2005), Australia (Lindsay et al., 2005), South Dakota (Perfetta et al., 1999), Great Basin (Saltzman et al., 1998), Iowa and Newfoundland (Saltzman et al., 2004), China and Kazakhstan (Saltzman et al., 2000), and Argentina (Sial et al., 2007).

lithologies (Ahlberg et al., 2009), and paleolatitudes (Álvaro et al., 2008). Figure 4 summarizes all localities at which the SPICE event has been documented to date. In addition to the extent and correlative nature of this signal that highly substantiate the use of the carbon-isotope record for a global oceanographic event, the absence of the excursion in key locations provides an independent witness of its strength. Coeval sections in Wyoming that do *not* contain the Pterocephaliid biomere (see below) also do not record a positive carbon isotope excursion (Figure 8 *in* Saltzman et al., 1998). In other words, these sections record a depositional hiatus (inferred from missing trilobite zones) coincident with the Sauk II/III sequence boundary and the peak of the SPICE event, thereby precluding any argument that the excursion might be a post-depositional or diagenetic feature.

4.2 Interpretations regarding the forcing mechanism of the SPICE event

Marine carbonates are precipitated in isotopic equilibrium with seawater bicarbonate (HCO_3^-) with a fractionation effect of ~1.2‰ (Michaelis et al., 1985). Since $\delta^{13}C$ values of modern seawater are typically 0±2‰ (Kroopnick, 1974) and there is no known ^{13}C-enriched source of carbon in the natural carbon cycle, positive carbon isotope excursions are commonly interpreted to represent organic carbon burial beyond steady state (e.g. Arthur et al., 1988; Cramer et al., 2008). Organic carbon burial (Kump and Arthur, 1999) preferentially removes isotopically light carbon (~-25‰), which would otherwise be oxidized and returned to the ocean/atmosphere system. The +4‰-5‰ $\delta^{13}C_{carb}$ anomalies in

the stratigraphic record can be explained by a 50% increase in organic carbon burial.

4.3 Reported values of $\delta^{13}C_{org}$ during the SPICE event

No published studies have reported paired $\delta^{13}C_{carb}$ and $\delta^{13}C_{org}$ data for the SPICE interval. Buggisch et al. (2003) provided low-resolution $\delta^{13}C_{carb}$ and $\delta^{13}C_{or}$ for Cambro-Ordovician Argentine shelf deposits, but the SPICE event was not recorded. Ahlberg et al. (2009) documented a +1.5-2.0‰ shift in $\delta^{13}C_{org}$ from the organic-rich Alum Shale of Sweden, which they interpreted as a record of the SPICE event based on trilobite zones. However, a lack of coeval carbonates in the region prohibited analysis for d13Ccarb. Álvaro et al. (2008) reported both $\delta^{13}C_{carb}$ and $\delta^{13}C_{org}$ from alternating shales and carbonates, respectively, across the SPICE interval, from one section in southern France that represents a mid-latitude, proximal to distal shelf setting. At this locality, $\delta^{13}C_{org}$ increased sharply by ~2‰ at the base of the interval, before steadily decreasing from -22‰ to -28‰. Over the SPICE interval, the authors noted a negative correlation between $\delta^{13}C_{carb}$ and $\delta^{13}C_{org}$, in contrast to the expected positive correlation, which may be explained by a post-depositional alteration, or enhanced ocean stratification and anoxia. Neither the alteration nor the ocean stratification explanations for their data can be interpreted as temporal variations in primary production fractionation in $\Delta^{13}C$.

4.4 $\delta^{34}S$, organic burial, and the SPICE event

Pyrite occurs as an accessory mineral in some peloidal wackestone facies at the base of the Middle Cambrian Wheeler Formation (Rees, 1986). Rees (1986) argued for periods of anoxic bottom waters during this interval, based on a recurring paucity of infaunal disturbance and lack of shelly fauna in laminated lithofacies. Sedimentological evidences for anoxia are sparse through Late Cambrian strata of the Great Basin (Cook and Taylor, 1977), but Gill et al. (2007) presents geochemical evidence from sulfur isotopes for expanding anoxic conditions during the Steptoean stage. Fifteen samples from Shingle Pass, NV were analyzed for $\delta^{34}S$ of carbonate-associated sulfur (CAS), and revealed a ~15‰ positive shift that peaked with the SPICE event. Gill et al. (2007) attributed the excursion to an increase in pyrite burial, which is isotopically light compared to oceanic sulfate. The sensitivity of sulfate $\delta^{34}S$ to shifts in the rate of pyrite burial over this interval has been interpreted to represent an oceanic sulfate reservoir that was much smaller than in the modern ocean (Hurtgen et al., 2009), while the more positive background values documented following the $\delta^{13}C$ excursion may suggest increased sulfate delivery from higher oxidative weathering.

CHAPTER 5

METHODS

5.1 Stratigraphic sections and sampling

Detailed, meter-scale stratigraphic sections were measured at the Shingle Pass and House Range localities to construct a sedimentological framework for the chemostratigraphic data. Each section was initially marked using a Jacob Staff, while preliminary notes of lithofacies present were taken in the field. Detailed descriptions of lithofacies, sedimentary structures, and contacts were made during sampling, accompanied by digital photographs.

Samples for isotopic analysis were taken every 1-2 meters, depending on lithology, and rocks showing obvious evidence of alteration (veins, fractures, or surface weathering) were avoided. Furthermore, all samples were taken from freshly broken surfaces, using a rock hammer. In order to improve the accuracy of organic carbon isotope analysis, fine-grained, organic-rich rocks were preferentially sampled where practical. A total of approximately 300 samples were labeled and taken back to the laboratory, where they were washed with deionized water and cut using a diamond-bladed rock saw.

Two sections were sampled in this study to test for replication of geochemical data, obtain a regional carbon-isotope signal, and to distinguish local controls on $\delta^{13}C$ values. In House Range, 340 meters were measured, beginning 20 meters below the Candland Shale and ending within the Sneakover Limestone, thereby encompassing the Pterocephaliid biomere (Palmer, 1965a). The Shingle Pass section was measured from the first exposure of the Emigrant

Springs Formation upward to the lower Whipple Cave Formation, for a total of 300 meters. Both sections were calibrated with those from Saltzman et al. (1998), based on formation and lithological boundaries, to account for analytical uncertainty in field measurements and construct an accurate comparison of isotopic data. Sections from Saltzman et al. (1998) can be compared to those of this study according to the following formulae:

House Range: $M_{HR} = (M'_{HR} \times 1.015) + 152.0$

Shingle Pass: $M_{SP} = (M'_{SP} \times 1.057) - 116.2$

Where M_{HR} and M_{SP} are section distances from this study in meters, and M'_{HR} and M'_{SP} are those from Saltzman et al. (1998) in meters. This calibration was confirmed using chemostratigraphic trends in the resulting co-plots (see Section 6.2), and allows us to incorporate previously published data into this study.

5.2 Sample preparation for isotopic analysis

All rock samples were washed to remove any dust that accumulated during transport, after which each sample was cut into at least two pieces using a diamond-bladed rock saw. Sample powders were microdrilled in micritic surfaces without visible secondary diagenetic features with an aluminum carbide bit to produce at least 50 mg of carbonate powder for analysis. To maximize the potential recovery of organic carbon, only dark, fine-grained portions of rock surfaces were drilled. All isotopic values are reported in δ-notation as per mille (‰) deviations from the Vienna Pee Dee Belemnite (V-PDB) standard. All

preparation and analyses were performed in the Las Vegas Isotope Science (LVIS) Laboratory at the University of Nevada, Las Vegas (UNLV).

5.3 Inorganic carbon ($\delta^{13}C_{carb}$) and oxygen ($\delta^{18}O$) isotope analysis

For $\delta^{13}C_{carb}$ and $\delta^{18}O$ values, approximately 50 µg of powder were reacted with orthophosphoric acid for 10 minutes at 70°C, using a Kiel IV carbonate device connected to a Finnigan Delta V Plus mass spectrometer via dual-inlet. Analytical reproducibility was better than 0.1‰ for both values, as determined by multiple measurements (6 per 44 samples) of National Bureau of Standards (NBS)-19, as well as an internal CO_2 standard (run once every 8 samples).

Reported isotopic values for each sample represent the arithmetic mean of eight measurements, for which standard deviations (1σ) were also determined (Appendix). In rare cases where 1σ exceeded 0.5‰ for the arithmetic mean, the sample was reanalyzed.

5.4 Organic carbon isotope ($\delta^{13}C_{org}$), TOC, and $\delta^{15}N$ analysis

For each sample, approximately 30-40 mg of powder was weighed and placed in an open silver capsule. Capsules were then placed in a quartz tray (holding 96 capsules), after which deionized water was added to each capsule until the samples were thoroughly moist and covered. Each tray underwent a 12-hour acid fumigation process, using a 250-ml beaker of 12 M HCl inside an airtight, glass-bell container, after which samples were dried for 6 hours at ~70°C. Individual samples were tested for unreacted carbonate material using

1-2 drops of diluted (1 M) HCl and then dried for an additional 4 hours. This process was repeated until all capsules were nonreactive with 1 M HCl. Dried samples were neutralized using a stepwise washing process, by which each capsule was immersed in deionized water (using hexagonal weighing dishes) for 6 hours and then dried for 4 hours. This process was repeated (up to 3 times) until each capsule arrived at a neutral (>5.5) pH. Caution was taken to avoid the accidental loss of sample from each capsule during immersion, in order to ensure accurate estimates of TOC.

When all samples were nonreactive and neutralized, the capsules were dried in an oven overnight at 70°C and then wrapped inside open tin capsules. Finalized samples were stored in an oven until isotopic analysis. Carbon and nitrogen isotope values were obtained using a Costech NA 2000 Elemental Analyzer with a continuous flow interface, connected to a Finnigan Delta V Plus mass spectrometer via dual-inlet. Analytical uncertainty was determined using 16 standards for each full carousel of 50 samples, comprised of 6 analytical standards: 6 Costech acetanilide; 4 cabbage; 2 USGS-24 (graphite); 2 USGS-600 (caffeine); 2 organic-rich soil; and 2 blank capsules. The results of unknown samples are calibrated using linear regression of standards. The instrument was also checked against two internal gas standards (CO_2 and N_2) during each sample analysis. Analytical reproducibility was better than 0.1‰ for both $\delta^{13}C_{org}$ and $\delta^{15}N$, and typically better than 0.05% for TOC and 0.1% for TON.

5.5 Petrographic analysis

Forty rock samples were selected to make billets for petrographic thin-sections, based on three criteria: 1) lithology, in order to produce a representative sample of lithofacies present in each section; 2) when proximal to inferred exposure surfaces and/or sequence boundaries; and 3) when secondary diagenetic features, such as styolitic or fenestral fabrics, were recognizable. In addition to providing detailed information for the description of lithofacies, petrographic analysis provided independent sedimentological evidence toward the presence and nature of correlative surfaces, thereby improving interpretations of the sequence stratigraphic framework. Furthermore, petrographic analysis allows evaluation of the nature and extent of diagenesis, to qualitatively assess its affect on $\delta^{13}C$ and $\delta^{18}O$. This may be done by the identification of grain leaching, styolitic dissolution, and multiple generations of carbonate cement, all of which indicate the interaction of secondary fluids from non-marine sources (Amieux et al., 1989; Ali, 1995).

All billets were prepared in the rock lab at UNLV, using a diamond-bladed rock saw, and, where practical, were cut from the slab surface opposite the drill spot for a direct comparison. The preparation surface was polished by hand with an abrasive slurry made from 600-grit aluminum carbide dust and deionized water. After 30-45 minutes of drying on a 65°C hot plate, each billet was set on a frosted glass slide, using 2 drops of UV-activated polymer glue. The glue was hardened by a 30-minute ultraviolet treatment, after which the billet was cut to ~2 mm thickness on a rock saw. A diamond-surfaced polishing wheel was then used

to reduce sample thickness to approximately 35-40 microns. After this, all sections were polished by hand to the appropriate 30-micron thickness, as confirmed by a petrographic microscope.

CHAPTER 6

RESULTS

6.1 Stratigraphy of measured sections

6.1.1 Orr Ridge Section — House Range, Utah

The base of the Candland Shale member of the Orr Formation coincides with the base of the Pterocephaliid biomere (Saltzman et al., 1998), thereby providing an appropriate datum for this section. However, sampling in this study began approximately 30 meters below this contact to provide a reasonable context for interpreting the sequence stratigraphic framework (Fig. 5). The uppermost 30 meters of the Big Horse Limestone member records a transition from medium-bedded, shelly bioclastic grainstone, to domal stromatolitic boundstone with an intraclastic grainstone matrix, to dominantly intraclastic grainstone bed sets with thin (<10 cm), shelly, basal lags. In contradistinction to this coarse-grained succession, the Candland Shale member is dominated by alternating bioclastic wackestone/packstone bed sets, which grades into a series of shale intervals. Coarse-grained interbeds become thinner and more sparse upsection, and typically pinch out within 100 meters. In the upper 40 meters of the member, however, the recurrence of bioclastic/oolitic grainstone and a meter-thick thrombolitic boundstone (at 125 m) indicates a reversal of this trend.

While the John's Wash Limestone member varies in thickness (45-55 meters) within the House Range, the cliff-forming expression of the coarse-grained succession is rather continuous (Fig. 6). Meter-scale, cross-bed sets are common within the oolitic grainstone that dominates the lower half of the

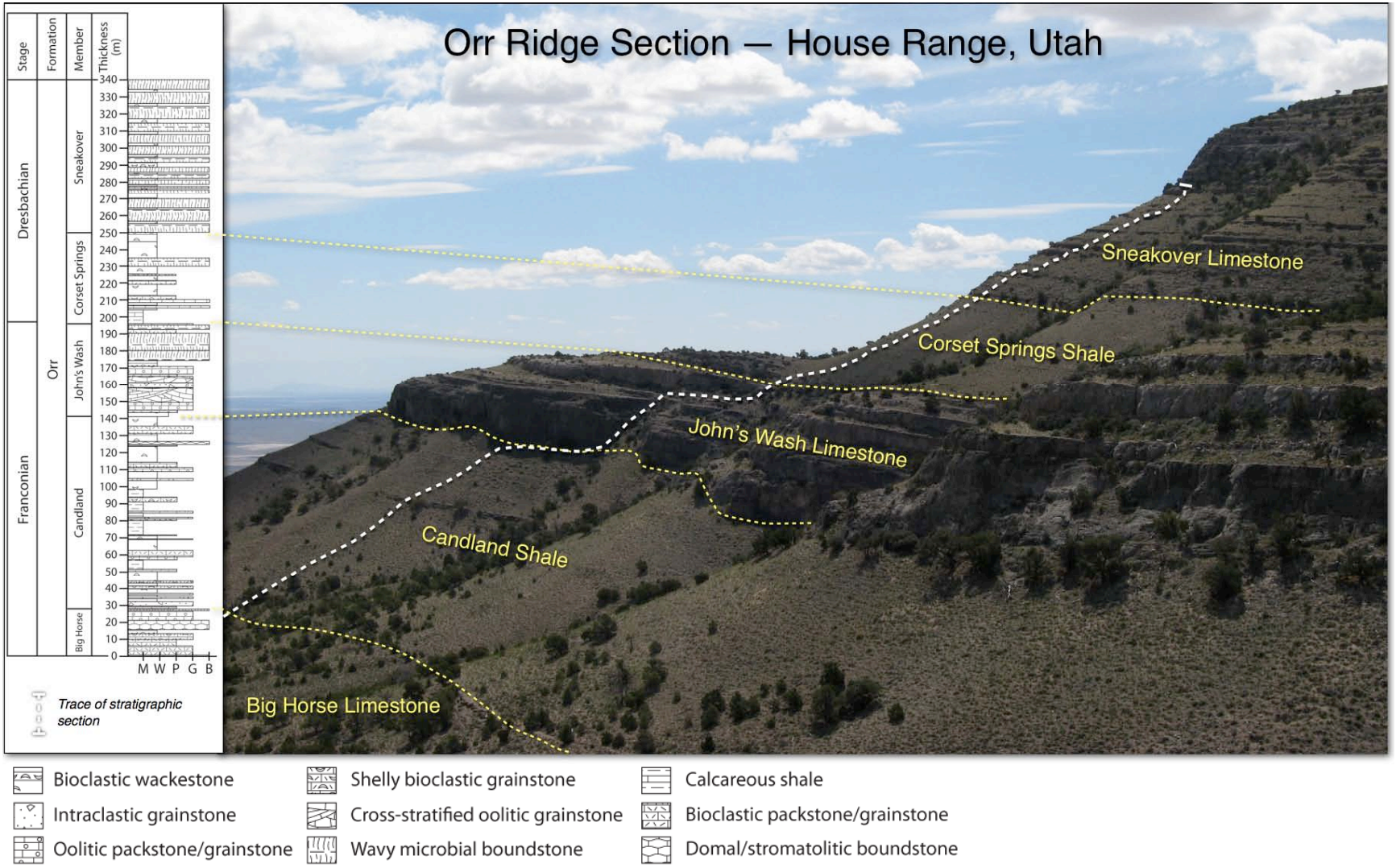

Figure 5: Meter-scale plot of lithology by facies association along Orr Ridge, western Utah. White dashed line shows approximate trace of section, along which samples for isotopic analysis were taken. Yellow dashed lines show boundaries of individual members of the Orr Formation.

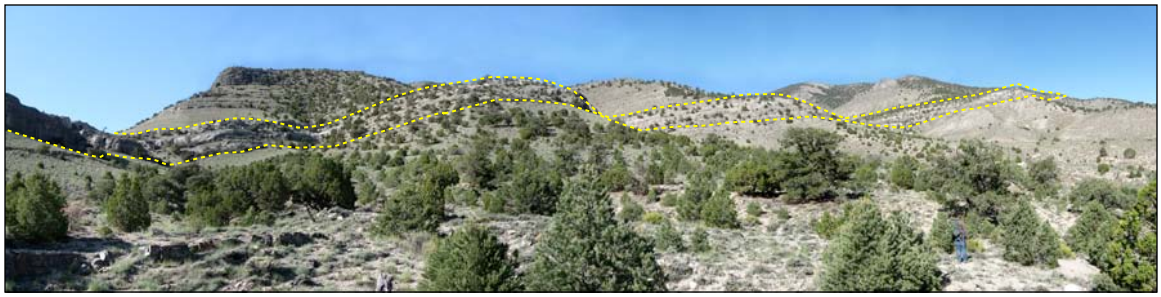

Figure 6: Outcrop of the John's Wash Limestone member of the Orr Formation. Yellow dashed line shows approximate stratigraphic boundaries. Picture facing west; Adam Zeiza for scale.

member, while fine-grained interbeds are notably absent. At 171 meters, a 2.5-meter, medium-gray, bioclastic wackestone overlies a sharp contact and marks the end of oolitic grainstone lithofacies in the John's Wash. A wavy erosional contact characterizes the top of the bed, which is overlain by a thick, chalky white boundstone. Locally, the John's Wash is capped by a thin (<10 cm) shelly bioclastic lag, marking a sharp lithologic boundary between the basal, olive-green shale beds of the Corset Springs Shale member.

With the exception of several meter-thick, bioclastic packstone and thrombolitic interbeds, the Corset Springs shale member is dominated by fine-grained lithofacies, which range from calcareous shale (basal 10

Figure 7: HR 230. Burrow-mottled, bioclastic wackestone, with silty dolomitic partings (weathered to pinkish-red).

m) to argillaceous wackestone to medium-gray, bioclastic wackestone (uppermost 38 m). Crinoidal skeletal fragments are the most common bioclast in coarse inter-beds, while brachiopod shells accompany infaunal disturbances among the thin-bedded wackestone intervals. The 5-meter, light-gray boundstone at 230 m is capped by a burrow-mottled texture with sparse, well-preserved brachiopod shells (Fig. 7). It is overlain by a dolomitic, argillaceous wackestone, making the succession comparable to the John's Wash/Corset Springs boundary. The uppermost 15 meters is characterized by moderately bioturbated, light to medium gray, argillaceous wackestone. At 250 m, a sharp lithologic boundary delineates the base of the Sneakover Limestone member, which is dominated by alternating dolomitic, bioclastic wackestone and wavy microbial boundstone. Bedding planes within both lithologies are frequently capped by undulating, red to orange, dolomitic lenses (Fig. 8). The section terminates within the Sneakover Limestone member, several meters below the base of the Notch Peak Formation, thereby en-compassing the Pterocephaliid biomere and providing sufficient data to analyze isotopic trends within the post-SPICE interval.

Figure 8: HR 406. Bioclastic wackestone (gray) capped by dolomitic lenses (weathered to pinkish-red) in bedding planes. Undulating surface signifies moderately heavy bioturbation.

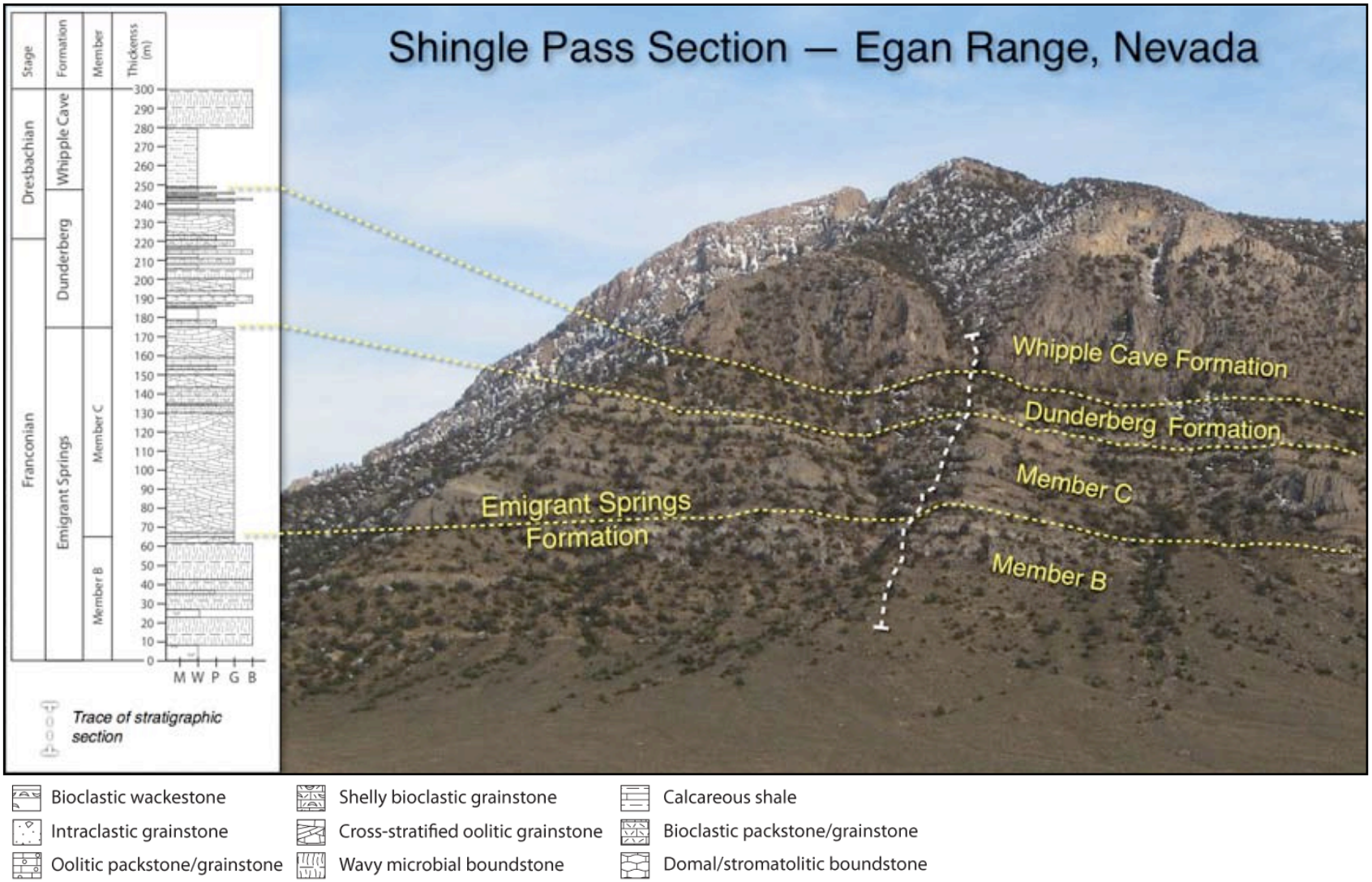

Figure 9: Meter-scale plot of lithology by facies association along section at Shingle Pass, east-central Nevada. White dashed line shows approximate trace of section. Yellow dashed lines show approximate formation and member boundaries.

6.1.2 Shingle Pass Section — Egan Range, Nevada

While carbon isotopic data from Saltzman et al. (1998) begin approximately 100 m below the Marjumiid-Pterocephaliid biomere boundary at Shingle Pass, the biostratigraphic contact was not exposed within this section. Our section begins rather at the first exposure of the Emigrant Springs Formation (Fig. 9), and likely to the south of the Saltzman et al. (1998) section, where although less of the formation is exposed, the block is less deformed and faulted. Nonetheless, this section captures the uppermost 62 meters of Member B, and all of Member C, of the Emigrant Springs Formation.

It is possible that the base of Member C should be placed nearer the sharp transition to coarse lithofacies at 9 m, given the thickness description of Kellogg (1963). However, Kellogg (1963) there differentiates Member C on its dominantly oolitic grains and cliff-forming expression, the former of which is absent from the section until 62 m. The several thick boundstone units at the

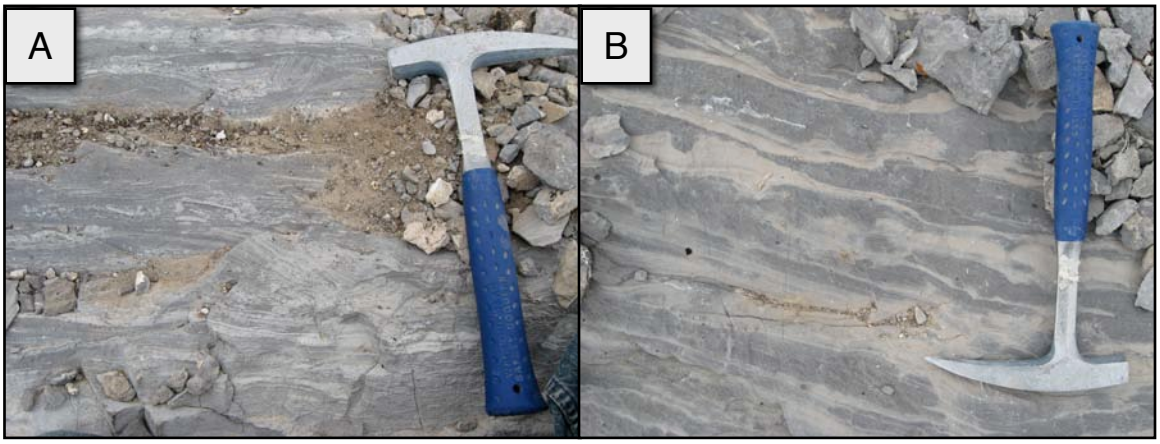

Figure 10: Bedforms within the lower Emigrant Springs Formation: A) intraclastic rudstone at SP 35, comprised of thin-laminated carbonate mudstone clasts; B) thin-laminated bioclastic wackstone at SP 5, characterized by post-depositional disruption of bedding.

base of the section, which are separated by thin-bedded, dolomitic wackestone intervals, are characterized by a chaotic matrix of wavy, chertified laminae. Various bedforms are present within intraclastic rudstone lenses (Fig. 10A) carved into laterally continuous bound-stone beds, and within fine-grained interbeds (Fig. 10B).

Member C of the Emigrant Springs Formation represents a thick succession of oolitic grainstone, which is predominantly cross-bedded. Intervals of coarse bioclastic material, rich in crinoid fragments, are also common, along with lenses of gravel to cobble-sized mud intraclasts. In the upper half of the member, however, there is a recurrence of 1-2 cm oncoids in association with more laterally continuous intraclastic rudstone beds that commonly cap the thicker intervals of oolitic grainstone. A sharp transition from intraclastic grainstone to a thick, bioclastic wackestone replete with twiggy-bodies (columnar recrystallized calcite) marks the base of the Dunderberg Shale.

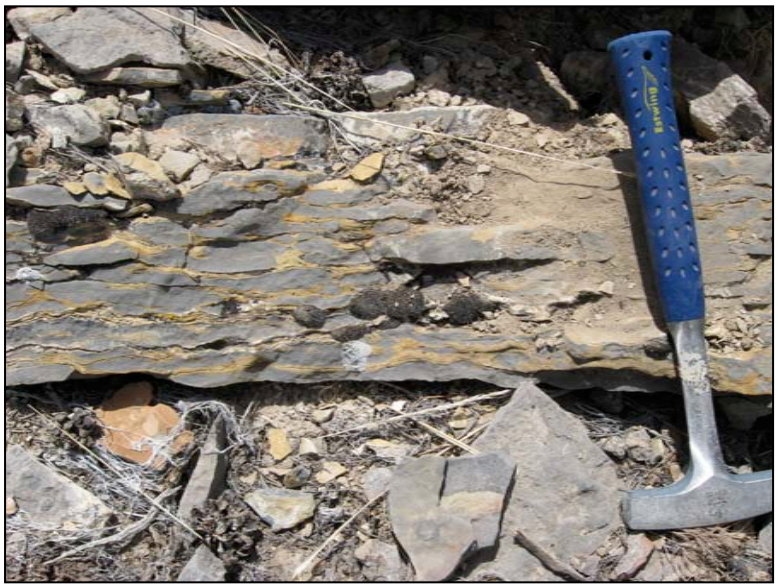

Figure 11: SP 186. Bioclastic wackestone/packstone (gray) with silty dolomitic partings (weathered to buff yellow). Undulating bedding planes likely from post-depositional compaction.

Locally, the Dunderberg Shale is comprised of four dominant lithofacies, which form four cycles within the ~70 meter unit. In each cycle,

heavily bioturbated, shelly bioclastic wackestone coarsens upward and is then overlain by thrombolitic boundstone. The bioclastic wackestone becomes more distinctly bedded to the top with silty dolomitic partings (Fig. 11), and contains some peloidal grains. Indi-vidual thrombolites are columnar and ~10-15 cm in diameter (Fig. 12), while thrombolitic-boundstone beds are ~1 meter thick and comprised of a bioclastic grainstone matrix. In each cycle, the thrombolite is overlain by intraclastic grainstone or flat-pebble conglomerate (Fig. 13), the first of which contains distinct polygonal mudcracks (at 190 m; Fig. 14). Oolitic grainstone, typically cross-bedded, is present in varying thickness at the top of each cycle, and is capped by a conformable contact with overlying fine-grained facies. At approximately 249 m in the

Figure 12: SP 242. Columnar thrombolite surrounded by grainstone matrix; typical of thrombolitic boundstone facies within the Dunderberg Formation. Quarter for scale.

Figure 13: SP 209. Carbonate mudstone clasts comprising a half-meter thick flat-pebble conglomerate (intraclastic rudstone).

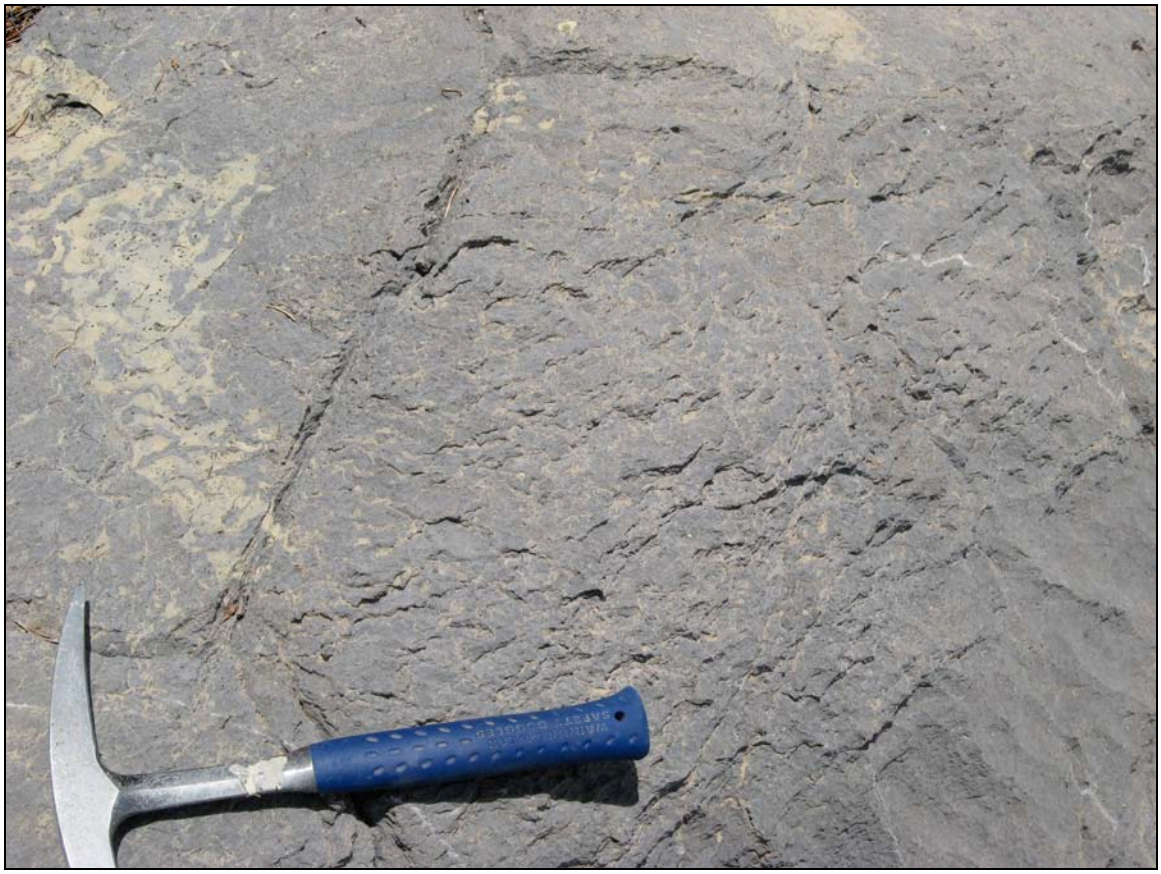

Figure 14: SP 190. Hexagonal mudcracks in a fine-grained carbonate matrix, capping an intraclastic rudstone bed and marking the cycle top. Shallow mudcracks may represent exposure within a supratidal environment and are infilled with bioclastic packestone from overlying layer. Silty dolomitic partings have weathered to yellowish tan.

section, a wavy, non-conformable contact marks the transition to thin-bedded, heavily recrystallized, dolomitic, wavy dolomitic boundstone. The contact can be seen from a distance by the sudden change in topographical expression (Fig. 9) to the more resistant dolomitic lithology of the lower Whipple Cave Formation.

6.2 Results for $\delta^{13}C_{carb}$ and $\delta^{18}O$ analysis; previously published data

Although Saltzman et al. (1998) provided a high-resolution $\delta^{13}C_{carb}$ record for the SPICE event from both sections within this study (Fig. 15), several

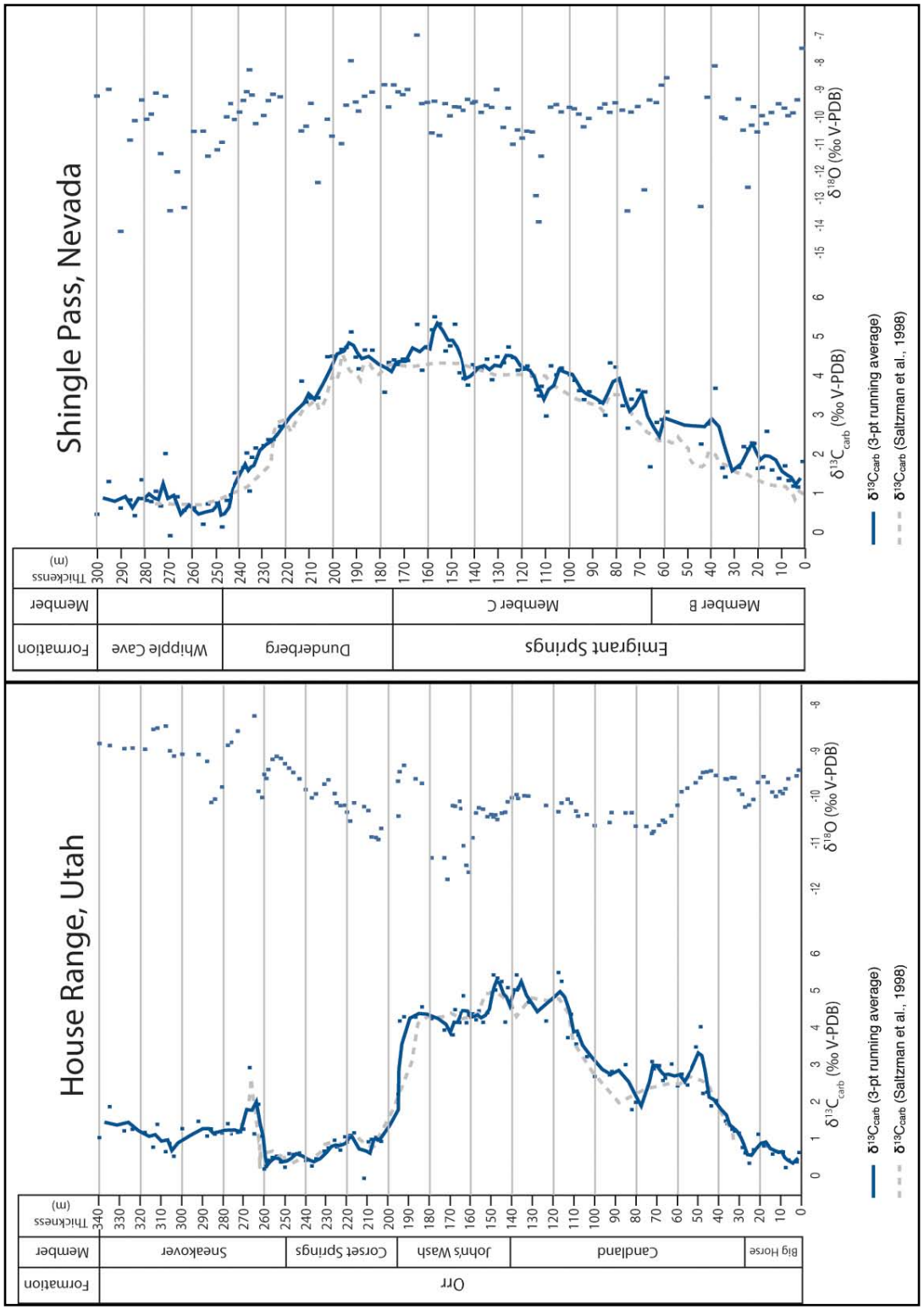

Figure 15: Carbon and oxygen isotopic results from House Range and Shingle Pass sections. Solid blue line represents a 3-point running average. Dashed gray line represents data from Saltzman et al. (1998) on a correlative depth scale.

concerns made it necessary to retrieve this value from the same samples analyzed for $\delta^{13}C_{org}$. The first was that our section must be perfectly calibrated to previously published data in order to produce a meaningful representation of $\Delta^{13}C$ trends. While this is possible using only lithological/formation boundaries, it would be unconfirmed and potentially misleading. Even assuming such a calibration, however, the nature of the carbon isotope record presents another challenge. For example, short-term variations in astronomical conditions, on the order of Milankovitch cycles, may also affect environmental conditions (temperature, solar irradiance, etc.) and thus have an impact on both carbon isotope values (Berger, 1978). Furthermore, in the House Range section of Saltzman et al. (1998), there is a paucity of data both at the onset and recovery of the SPICE event. Thus the analysis of $\delta^{13}C_{carb}$ precludes any question of calibration and allows us to accurately incorporate previously published data for each section, while providing a workable dataset for an accurate paired carbon-isotope analysis.

Carbonate carbon isotopic data from are presented in Figure 15 and Appendix 1. Both sections record a 5.5‰ excursion in $\delta^{13}C_{carb}$ above normal marine values of 0‰-1‰. Values of $\delta^{13}C_{carb}$ range from -0.09‰ to 5.47‰ in House Range and -0.10‰ to 5.49‰ in Shingle Pass, and variation between stratigraphically adjacent samples is relatively low across each section, averaging 0.39‰ (maximum 1.98‰) for House Range and 0.45‰ for Shingle Pass (maximum 2.1‰). At House Range, values begin to rise steadily at the base of the Candland Shale member, peaking in the uppermost 25 m of the

member. Throughout the overlying John's Wash member, $\delta^{13}C_{carb}$ remains relatively stable and (4‰-5‰) before rapidly (within 10 meters) falling to pre-excursion background values. This pattern is similar at Shingle Pass, where values begin to rise within Member B of the Emigrant Springs Formation and peak in the uppermost 20 meters of Member C. At 200 m (within the Dunderberg Formation), $\delta^{13}C_{carb}$ begins to fall steadily, reaching pre-excursion background values near the base of the Whipple Cave Formation. An additional minor excursion is present within the Sneakover Limestone, which peaks at 267 m and can be correlated across the shelf (Saltzman et al., 1995). The absence of this minor excursion in the Shingle Pass section suggests that either a depositional hiatus is present, or the peak exists upsection within the Whipple Cave Formation.

For comparison, data from Saltzman et al. (1998) is shown by the gray, dashed line, which represents a 3-point moving average. Minor discrepancies of up to 1‰ between the data sets (e.g. at 80-110 m in House Range) are primarily due to differences in sampling frequency, and illustrate the need to obtain both isotopic signatures from the same sample. Nonetheless, most data plot sufficiently within analytical reproducibility to confirm our calibration of each section (cf. Methods - Stratigraphic Sections and Sampling).

Oxygen isotope data ($\delta^{18}O$) are within the normal range of values for lower Paleozoic carbonates (Jaffrés et al., 2007). Strong covariation in cross-plots of $\delta^{18}O$ and $\delta^{13}C$ may suggest alteration by meteoric fluids or a salinity dependence (Bristow and Kennedy, 2008). With the exception of one anomalous point (267 m;

$\delta^{18}O$ = -4.30‰), however, values range from -12.88‰ to -7.68‰ at House Range (average -9.87‰), with no significant correlation to $\delta^{13}C_{carb}$ (Fig. 16; R^2 = 0.09). The Shingle Pass section yielded a wider range of values, from -14.19‰ to -7.04‰ (average -10.06‰), again with no significant correlation to $\delta^{13}C_{carb}$ (Fig. 16; R^2 = 0.06). There are no significant temporal trends within either data set, and there is no apparent correlation to lithology.

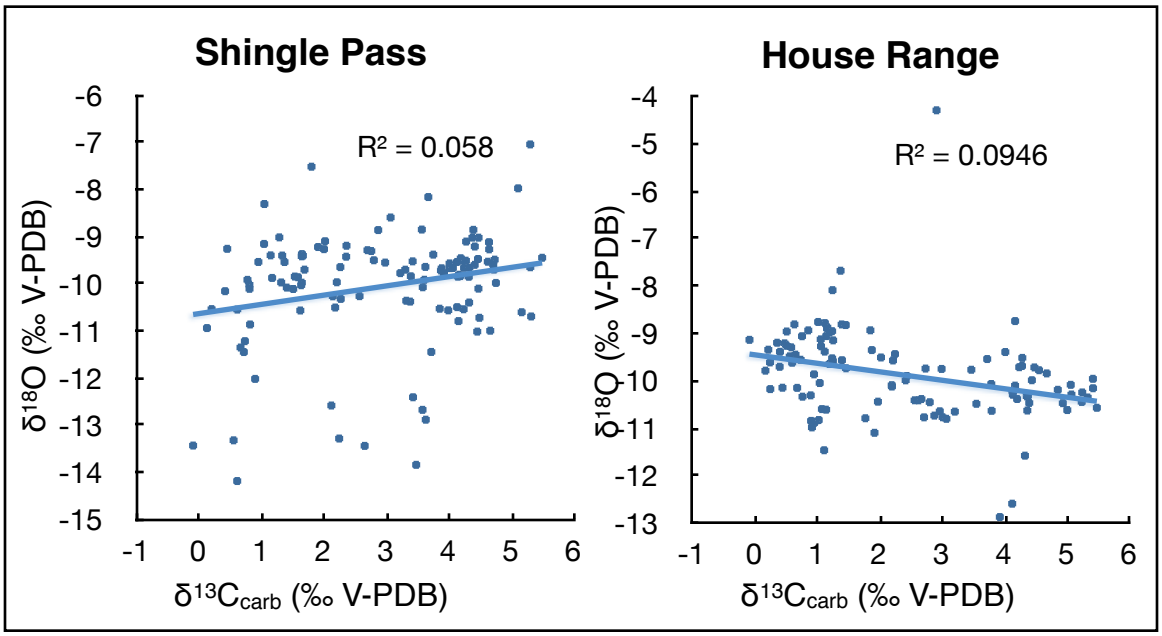

Figure 16: Cross plots of carbon and oxygen isotopes from each section. Bold line represents a least-squares regression for each data set.

6.3 Results for $\delta^{13}C_{org}$, $\delta^{15}N$, and TOC analysis

Figure 17 and 18 summarize all isotopic and elemental results for organic carbon analyses. In each section, $\delta^{13}C_{org}$ values record a 2.5-3‰ positive excursion over the SPICE interval, which is parallel to but approximately half the magnitude of the excursion documented in carbonate carbon (Saltzman et al.,

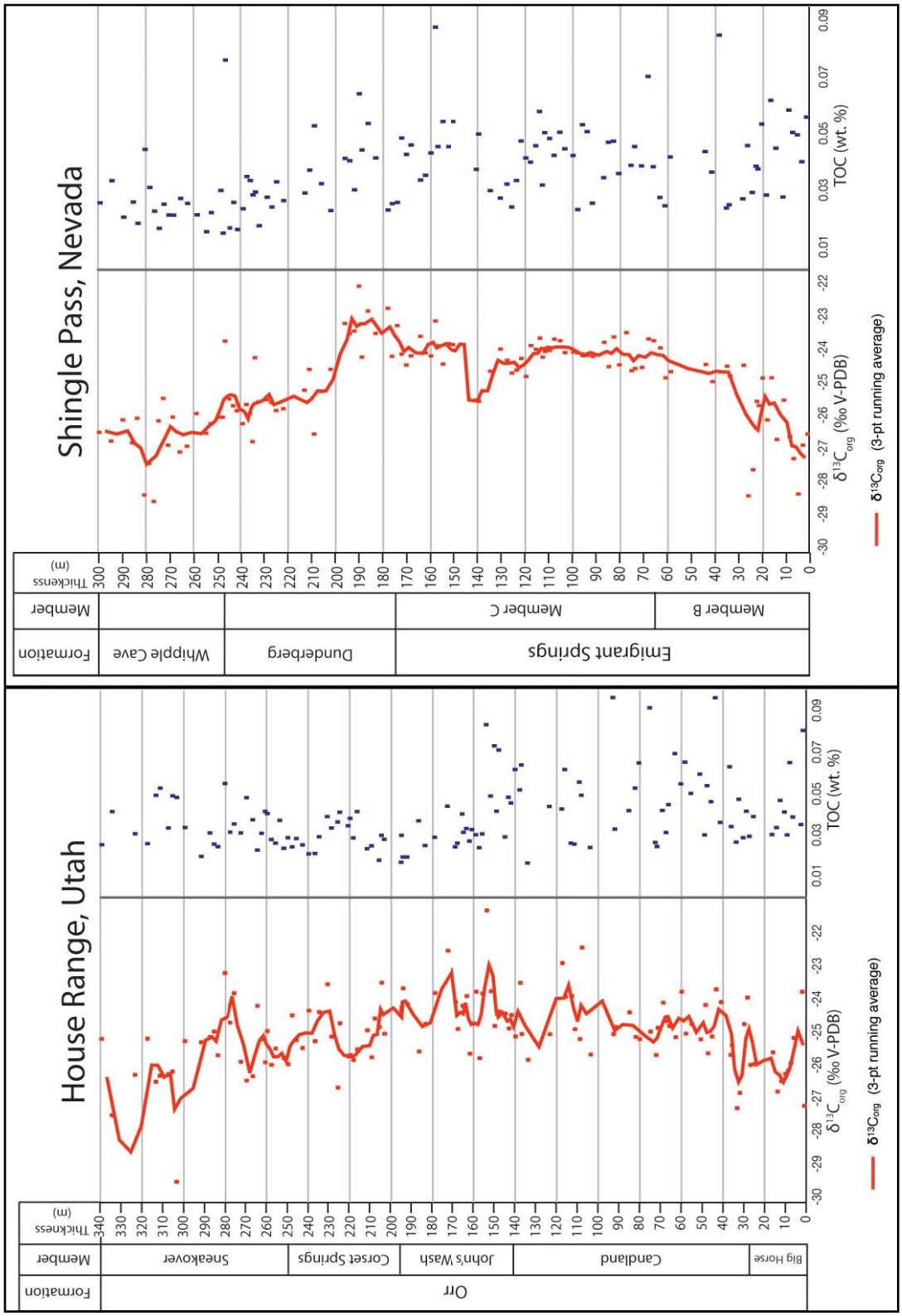

Figure 17: Organic carbon isotope and TOC results from both sections. Bold red line represents a 3-point moving average of stratigraphically adjacent samples

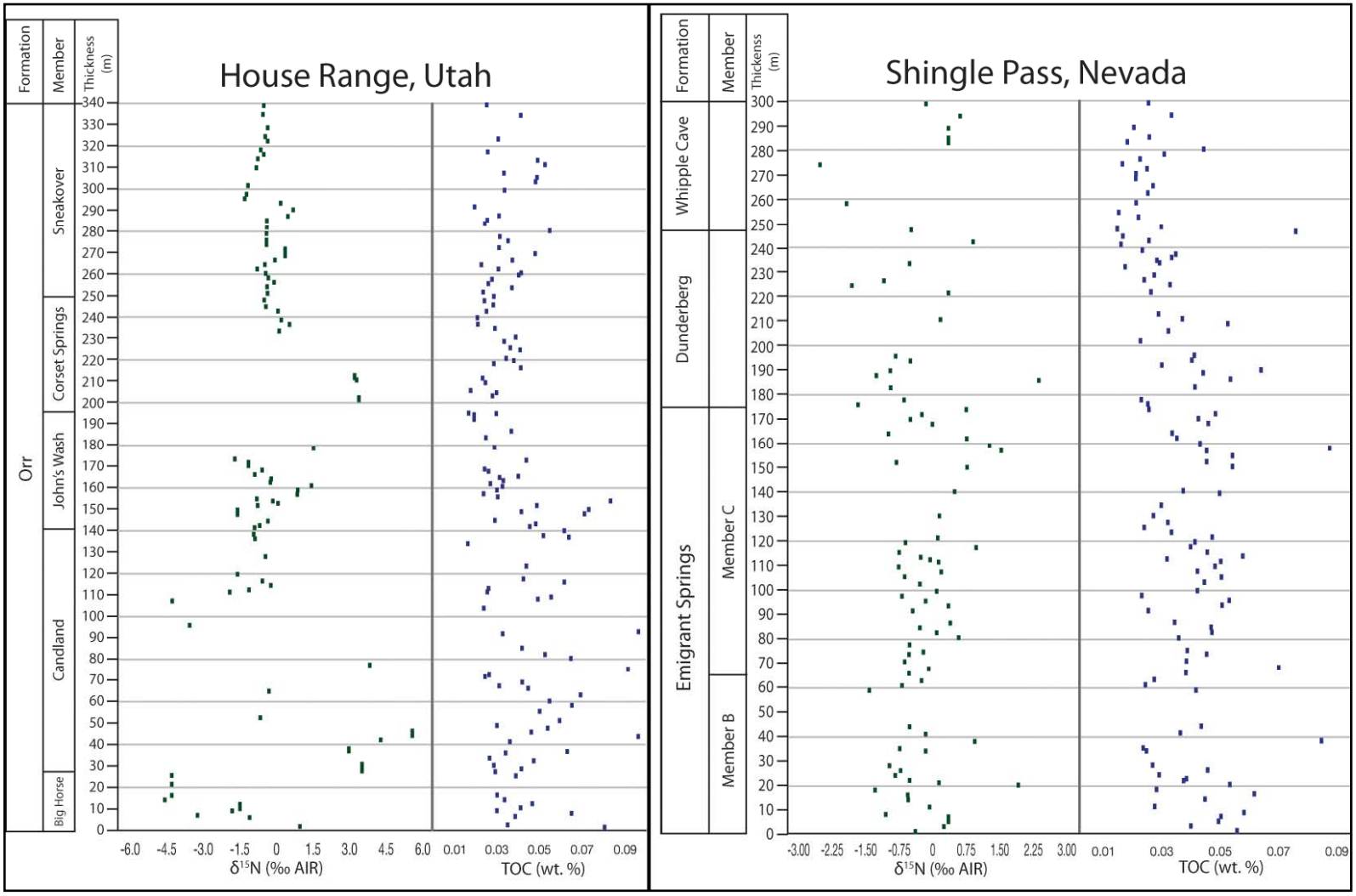

Figure 18: $\delta^{15}N$ results from both sections, alongside TOC data. Data from Shingle Pass show significant scatter, though within a relatively narrow range, while data from House Range show two distinct peaks. Temporal trends were not interpreted, however, due to the high number of samples yielding no results and the overall low TOC content.

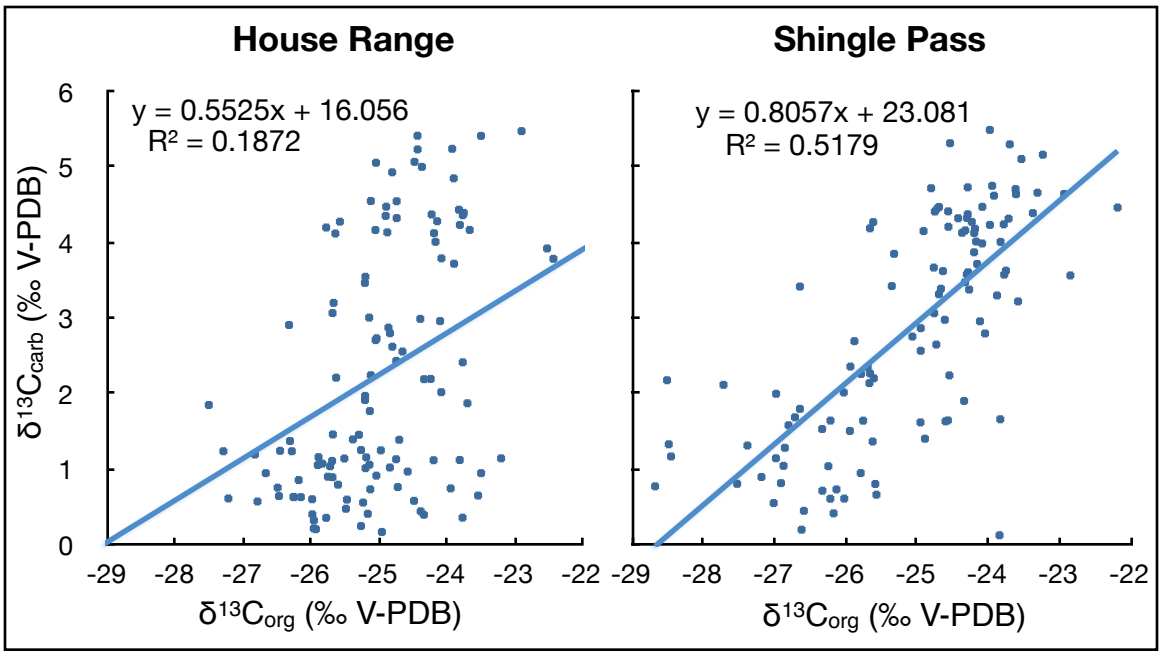

Figure 19: Cross plots of carbonate and organic carbon isotopes across the SPICE interval. Bold line represents a best-fit line from a least squares regression and reveals a significantly stronger covariation of carbon isotopic data in the Shingle Pass section.

1998). Cross plots of paired carbon isotope values ($\delta^{13}C_{carb}$ vs. $\delta^{13}C_{org}$) reveal only a moderately significant covariation, for which least-squares regression analyses yield an R^2 value of 0.19 at House Range and 0.52 at Shingle Pass (Fig. 19). Compared to the results for $\delta^{13}C_{carb}$, both plots of $\delta^{13}C_{org}$ are characterized by significantly higher variability among stratigraphically adjacent samples. This value averages 1.06‰ (max 5.78‰) in House Range and 0.71‰ (max 3.94‰) in Shingle Pass. While this contrast may in part be due to greater analytical uncertainty (σ = 0.5‰), the greater susceptibility of $\delta^{13}C_{org}$ to local environmental controls on shorter timescales and the much shorter residence time of marine organic carbon (1-6 ka) warrant the use of a moving average when considering temporal covariation. When a 3-point moving average of

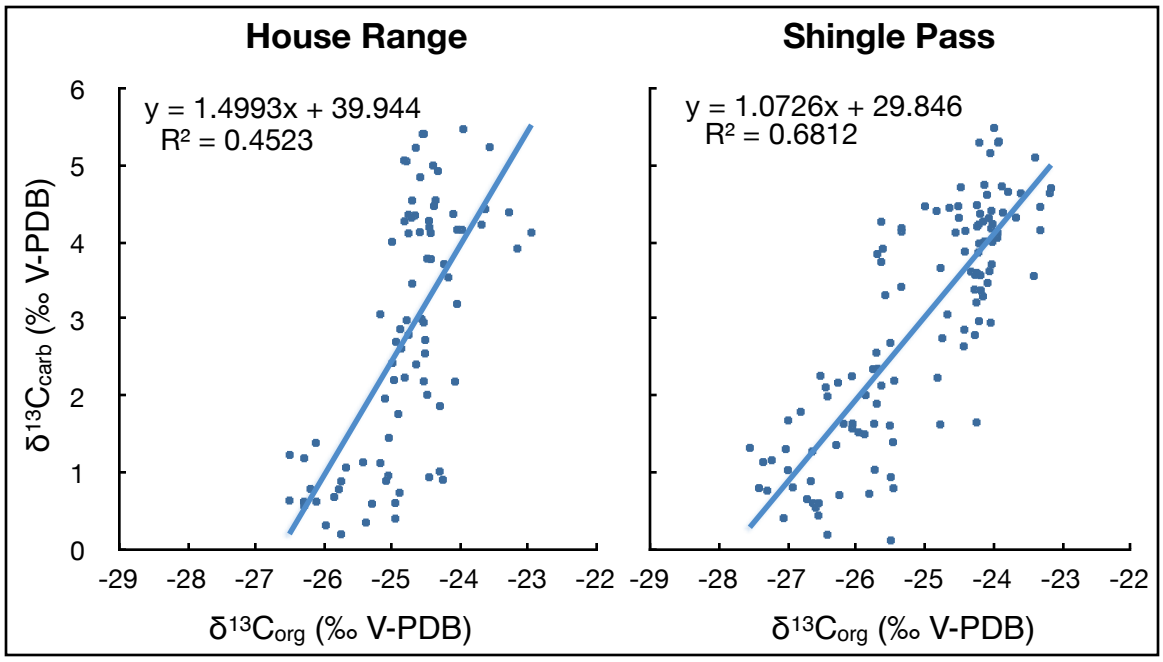

Figure 20: Cross plots of carbonate and organic carbon isotopes across the SPICE interval, using 3-pt averages of $\delta^{13}C_{org}$. Resulting best-fit line from a least squares regression reveals a significantly stronger covariation of carbon isotopic data in both sections.

$\delta^{13}C_{org}$ is plotted against $\delta^{13}C_{carb}$ (Fig. 20), the respective R^2 values increase to 0.45 for House Range and 0.68 for Shingle Pass.

Total organic carbon was calculated as a function of the starting mass of unreacted carbonate powder in each capsule, using the elemental mass of carbon acquired by the Elemental Analyzer. Thus any unreacted carbonate present in the capsule would not only result in an overestimate of $\delta^{13}C_{org}$, but also in TOC. While this provides a double check in identifying unreacted carbonate in the sample, thorough acid digestion may also dissolve a significant portion of organic carbon (Galy et al., 2007), which results in an underestimate of TOC. The acid fumigation method used within this study prevents major leaching

of hydrolized organic components. However, the minor loss of dissolved, labile organic components during washing is possible, and presents a challenge to accurate TOC estimates in organic-poor carbonate rocks. Results for estimated TOC range from 0.02% to 0.10% (average 0.04%) in House Range and 0.02 to 0.09% (average 0.04%) in Shingle Pass.

Although each sample was analyzed for $\delta^{15}N$ from total organic nitrogen (TON), the preparation methods were not specifically designed to obtain this value accurately from such a small sample, nor to guard against atmospheric contamination. Estimates of TON were consistently ~10-12% that of TOC where measured, which is sufficiently close to the detection limit of the Elemental Analyzer that many values were not obtained. For samples that resulted in recognizable peaks for the mass spectrometer, the data are shown in Figure 18. Values range from -5.2‰ to 5.6‰ (average -0.1‰) at House Range, and record two distinct positive peaks (3-5‰), possibly associated with increased denitrification (Junium and Arthur, 2007). There is considerably more scatter in data from Shingle Pass, where values range from -2.5‰ to 2.4‰ (average -0.2‰), though with no distinct temporal trends.

6.4 Plot of carbon isotopes and $\Delta^{13}C$

Figures 21 and 22 present all data for carbonate and organic carbon isotope difference alongside plots of each independent carbon isotope. The resultant scatter in data points is primarily due to the inter-sample variability in $\delta^{13}C_{org}$, and recalculating $\Delta^{13}C$ from a 3-point moving average thereof reduces

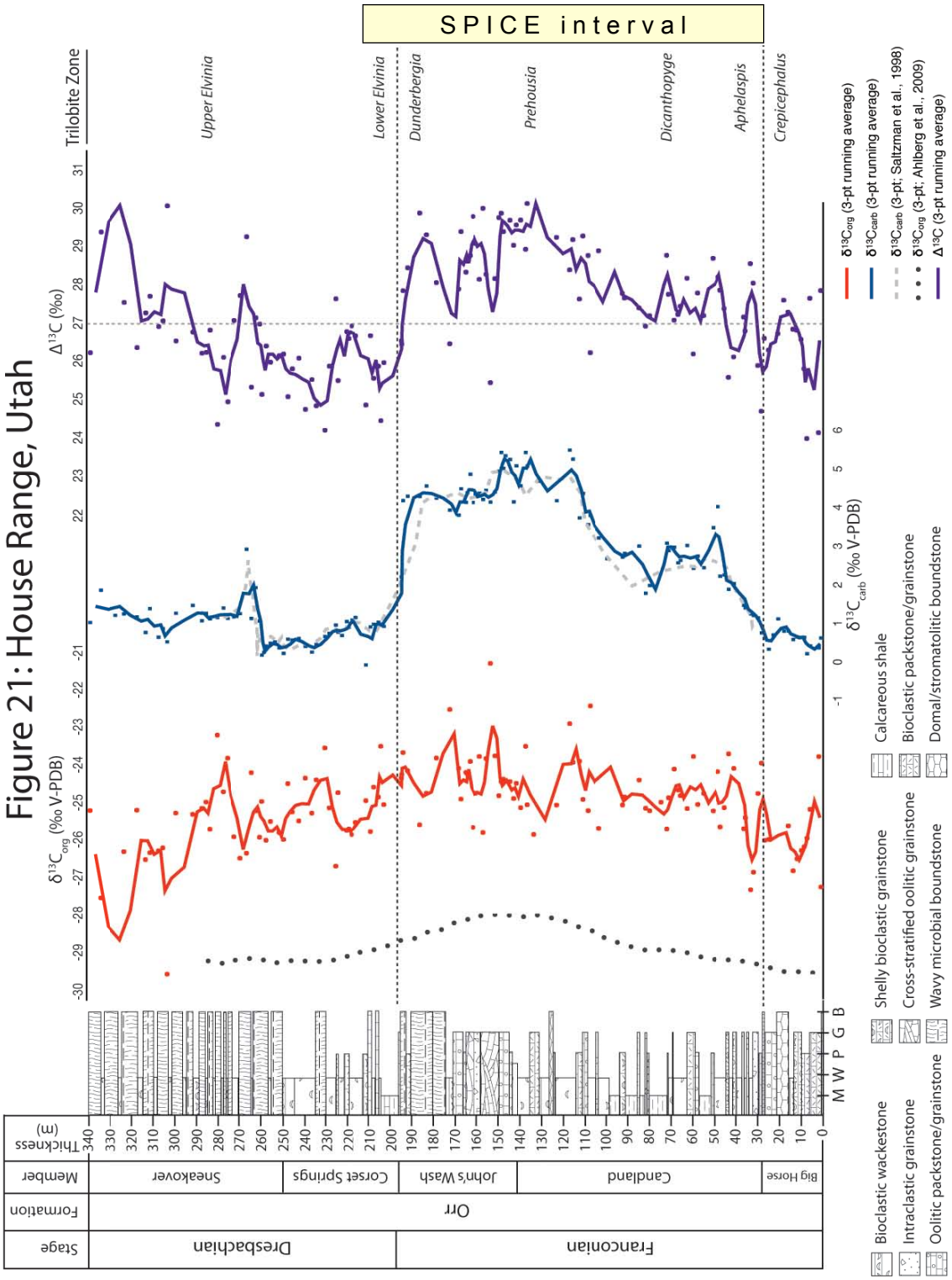
Figure 21: House Range, Utah
SPICE interval
Trilobite Zone
Upper Elvinia
Lower Elvinia
Dunderbergia
Prehousia
Dicanthopyge
Aphelaspis
Crepicephalus
Δ13C (‰)
δ13Corg (‰ V-PDB)
δ13Ccarb (‰ V-PDB)
δ13Corg (3-pt running average)
δ13Ccarb (3-pt running average)
δ13Ccarb (3-pt; Saltzman et al., 1998)
δ13Corg (3-pt; Ahlberg et al., 2009)
Δ13C (3-pt running average)
Stage
Formation
Member
Thickness (m)
Franconian
Dresbachian
Orr
Big Horse
Candland
John's Wash
Corset Springs
Sneakover
M W P G B
Bioclastic wackestone
Intraclastic grainstone
Oolitic packstone/grainstone
Shelly bioclastic grainstone
Cross-stratified oolitic grainstone
Wavy microbial boundstone
Calcareous shale
Bioclastic packstone/grainstone
Domal/stromatolitic boundstone

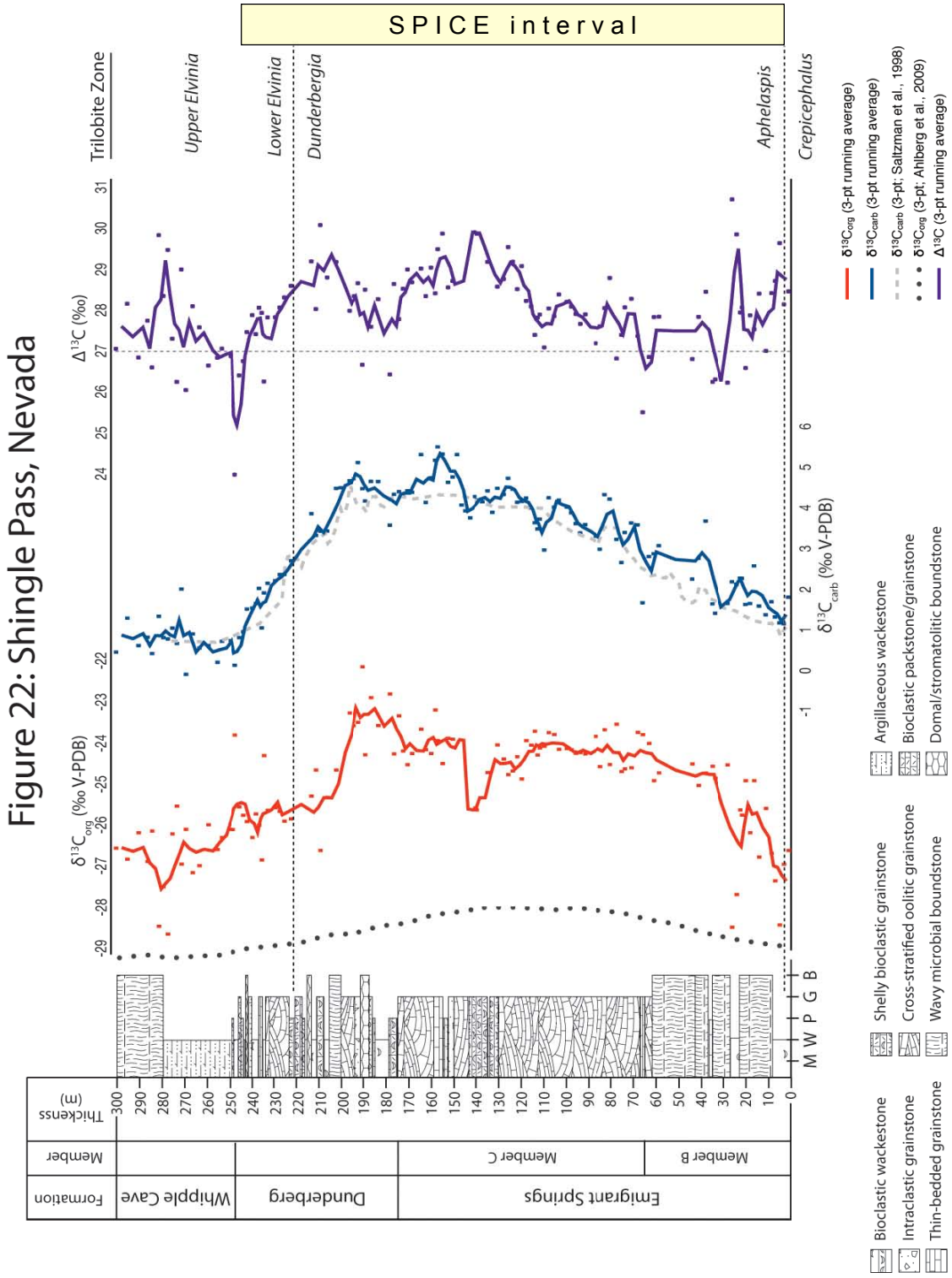
Figure 22: Shingle Pass, Nevada
SPICE interval
Trilobite Zone
Upper Elvinia
Lower Elvinia
Dunderbergia
Aphelaspis
Crepicephalus
Δ13C (‰)
δ13Corg (‰ V-PDB)
δ13Ccarb (‰ V-PDB)
Formation
Member
Thickness (m)
Whipple Cave
Dunderberg
Emigrant Springs
Member B
Member C
M W P G B
δ13Corg (3-pt running average)
δ13Ccarb (3-pt running average)
δ13Ccarb (3-pt; Saltzman et al., 1998)
δ13Corg (3-pt; Ahlberg et al., 2009)
Δ13C (3-pt running average)
Bioclastic wackestone
Shelly bioclastic grainstone
Argillaceous wackestone
Intraclastic grainstone
Cross-stratified oolitic grainstone
Bioclastic packstone/grainstone
Thin-bedded grainstone
Wavy microbial boundstone
Domal/stromatolitic boundstone

the scatter significantly. However, calculating $\Delta^{13}C$ through the difference in moving averages of $\delta^{13}C_{carb}$ or $\delta^{13}C_{org}$ does not affect temporal trends in either data set, thus all data for $\Delta^{13}C$ are reported here as the per mille (‰) difference between $\delta^{13}C_{carb}$ and $\delta^{13}C_{org}$, where the respective values were taken from the same sample. Both sections record a distinct 3‰ positive excursion in $\Delta^{13}C$ across the SPICE interval, for which values remain greater than 27‰ (up to 30‰) before falling rapidly to 25-26‰ immediately following the Sauk II-III boundary. Values of $\Delta^{13}C$ range from 24.0‰ to 30.1‰ (average 27.2‰) at House Range, and similarly from 24.0‰ to 30.7‰ (average 28.0‰) at Shingle Pass.

CHAPTER 7

DISCUSSION

7.1 Nature and strength of $\delta^{13}C_{carb}$ and $\delta^{13}C_{org}$ records

Regionally consistent isotopic results from both $\delta^{13}C_{carb}$ and $\delta^{13}C_{org}$ demonstrate the robust nature of each record, and provide a sound foundation on which to assess model predictions of the carbon cycle in response to the SPICE event. Comparison of $\delta^{13}C_{carb}$ data to that from previously published studies (Saltzman et al., 1998) revealed a negligible margin of error in the reproducibility of the record from each sampling locality, while the existing global record (e.g. Glumac and Walker, 2008; Saltzman et al., 2004) confirms that stratigraphic trends in $\delta^{13}C_{carb}$ reflect shifting chemistry in the Cambrian ocean. Nonetheless, we employed various geochemical and statistical checks, accompanied by petrographic analysis, to ensure the quality of isotopic data.

Stratigraphic plots of $\delta^{13}C_{org}$ reveal a moderately significant covariation with $\delta^{13}C_{carb}$, consistent with the hypothesis that ^{13}C-enrichment of the marine DIC also controlled the isotopic composition of bulk DOC. While the consistently low TOC content of carbonate samples raises some concern over the credibility of our results, the methods employed within this study have been proven to accurately retrieve $\delta^{13}C_{org}$ from similarly organic-poor samples (Wang et al., 2008; Young et al., 2008). A plot of $\delta^{13}C_{org}$ vs. TOC revealed no significant correlation (Fig. 23) and suggests that organic carbon isotopes were not dependent on the degree of thermal alteration during burial. Furthermore, although stratigraphic plots of $\delta^{13}C_{org}$ show moderate scatter, the data are

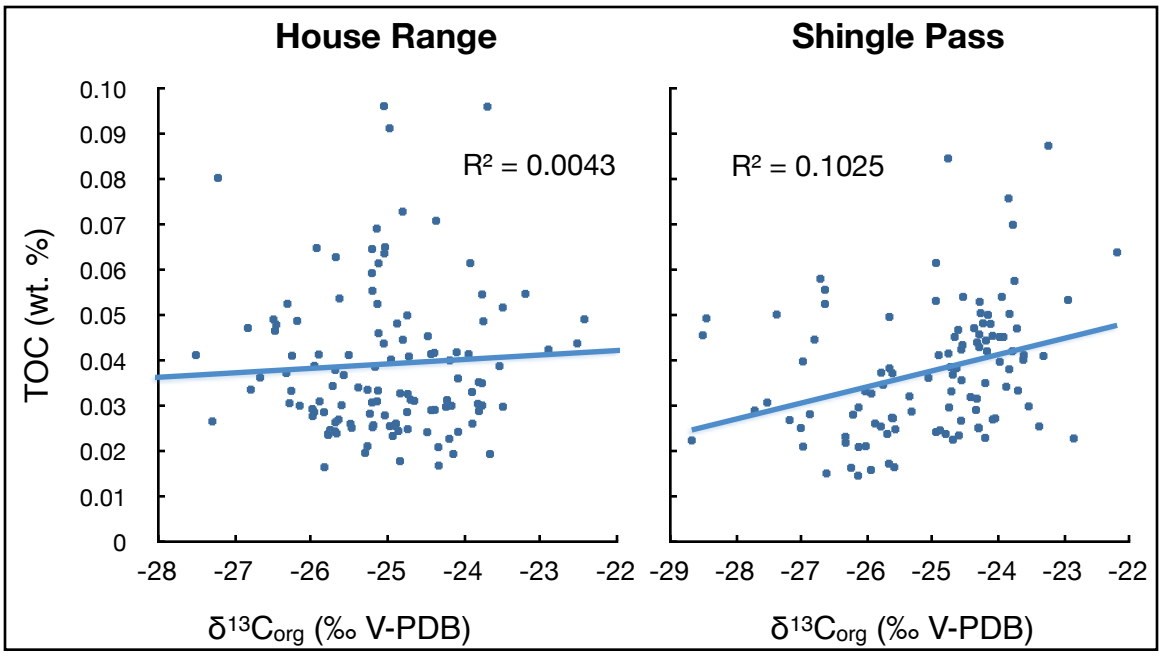

Figure 23: Cross plots of organic carbon isotopes and TOC. Resulting best-fit line from a least squares regression reveals no significant covariation between values in either section.

consistent with the short residence time of organic carbon compared to carbonate carbon (Siegenthaler and Sarmiento, 1993) and its consequent sensitivity to short-term variability in climatic/oceanographic conditions (e.g. Bekker et al., 2008; Lara et al., 2010). We interpret this scatter to reflect a secondary control on the local isotopic composition of the marine organic matter, given the regional correlation of long-term trends.

7.2 Stratigraphic $\delta^{13}C$ trends

Evaluating regional trends in $\delta^{13}C_{org}$ and carbon isotopic fractionation requires a careful control on the timing of each section. Stratigraphic sections at House Range and Shingle Pass express contrasting carbonate stacking patterns

and sedimentation rates, which precludes a direct temporal comparison of carbon isotopic trends. This is illustrated by a difference in overall thickness of the SPICE interval (180 m vs. 250 m), and in facies associations throughout each section. Any attempt to correlate the sections purely on cycle expressions is complicated by autocyclic processes of filling accommodation space, such as tectonic controls on subsidence (Rees, 1986), and the lateral migration of peritidal shoal facies. While Osleger (1991b) attempts to exclude such mechanisms in interpreting meter-scale cyclicity in shallow subtidal facies of the lower Candland Shale, opting for a Milankovitch-driven global eustatic control, this interpretation results in conflicting eustatic curves for North America (Osleger and Read, 1991). One solution is to focus on sequence stratigraphic key surfaces resulting from forced regression, rather than meter-scale cycles (Catuneanu et al., 2009). This may be done in collaboration with the $\delta^{13}C_{carb}$ record, which is less sensitive to local controls, in order to accurately compare trends in $\delta^{13}C_{org}$ and $\Delta^{13}C$.

Using a combination of bio-, sequence and chemostratigraphic data, coeval boundaries were interpreted at five points in each section (Fig. 24):

1) and 2) Boundaries Pt_B and Pt_T represent the approximate base and top of the Pterocephaliid biomere, which is well correlated across the Great Basin (Palmer, 1965a; Saltzman et al., 1998). Given the similar shelf setting and paleo-water depth of each section, the issue of diachroneity in biomere boundaries (Palmer, 1984) is likely avoided here. The uppermost positive $\delta^{13}C_{carb}$ peak in the House Range section marks the end of the Pterocephaliid

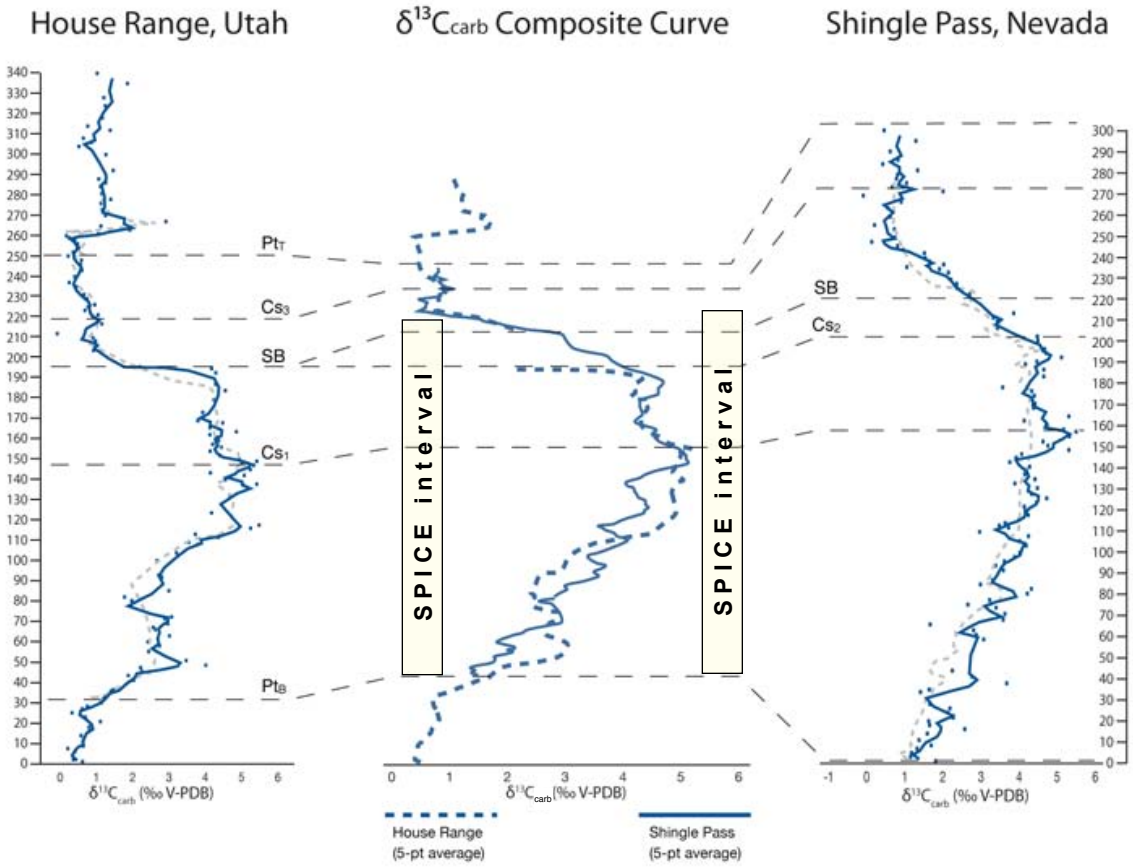

Figure 24: Time-equivalent overlay of $\delta^{13}C_{carb}$ from each section, based on interpreted coeval boundaries: top (Pt_T) and base (Pt_B) of the Pterocephaliid biomere; Sauk II/III sequence boundary (SB); peak values of the SPICE event (Cs_1); base of the falling limb of the SPICE event (Cs_2); and a minor peak in the post-SPICE interval (Cs_3).

biomere (Saltzman et al., 1995; 1998) but is not evident in data from Shingle Pass. Saltzman et al. (1995) interpreted a shelf-wide drowning unconformity at the base of the isotopic excursion, based on its absence from inner shelf sections. This may also explain the absence of the excursion in the Shingle Pass section, the top of which is marked by an exposure surface. Another possibility, however, is that the excursion simply lies further upsection.

3) The Sauk II-III boundary (SB) represents a craton-wide discontinuity that is well-defined in the Great Basin (Saltzman et al., 2004). However, the contrasting lithologic expression between the House Range and Shingle Pass sections allows at least two possible stratigraphic interpretations. The first is that deposition was continuous until the boundary in each locality, while the Corset Springs shale comprises a condensed section. However, this results in a rather stochastic overlay of the isotope records during the peak of the SPICE interval. Another interpretation is that the carbonate-siliciclastic transition at House Range represents a Type-I sequence boundary, in which a period of non-deposition or erosion can be approximated using an additional chemostratigraphic marker (Cs_2, Fig. 24). This is analogous to the regional discontinuity seen in the Llano Uplift, TX, which resulted from non-deposition or erosion during the Dunderbergia biozone immediately preceding the sequence boundary (Osleger and Read, 1993). Early meteoric cements are present in samples at the top of the John's Wash member (Fig. 25) and suggest the interaction of meteoric fluids. Fresh-water meteoric fluids are relatively depleted in ^{13}C and, along with soil-gas CO_2 interaction during exposure, could potentially explain the sharp negative shift

Figure 25: Needle-like acicular and equant cements, which grow at grain rims to fill pore spaces (seen here at the rims of bioclasts), are typical of phreatic-zone environments with some degree of freshwater input (Amieux et al., 1989).

(~2‰) seen in less than a meter from the top of the John's Wash member (Immenhauser et al., 2007). This model results in a rather conformable overlay of the isotope records for the SPICE interval, while also taking into account the nature of the sequence boundary.

4) Maximum $\delta^{13}C_{carb}$ values at 148 m in the House Range were correlated to maximum $\delta^{13}C_{carb}$ values at Shingle Pass, as both intervals end a gradual trend to rising $\delta^{13}C_{carb}$ values. Correlation of the peak (Cs_1) results in a good, though offset, correlation of carbon isotopic trends from the base (Pt_B). One explanation for the offset trend at this interval is the markedly different nature of carbonate cycles. The Candland Shale is dominated by bioclastic wackestone to grainstone sets, and has been interpreted as a record of fifth-order eustatic variations in a deep to shallow subtidal depositional setting (Osleger, 1991b). Sparse outcrops on the slope-forming unit also limit sampling resolution. However, the same interval is recorded at Shingle Pass as a succession of wavy laminated boundstone and oolitic grainstone that is ~50% thicker, and represents autocyclic deposition within a shallow subtidal to intertidal setting (Kellogg, 1963). The autocyclic control on deposition is evidenced by the laterally discontinuous nature of beds, which commonly pinch out within 1 km. Thus the contrasting nature of deposition between localities may render impossible a perfect temporal comparison. Furthermore, a difference in sampling resolution may have resulted in a biased moving average in the House Range plot, thereby masking some of the short-term isotope stages.

5) A minor peak at 219 m in the House Range is interpreted to be coincident with the minor peak at 271 m at the Shingle Pass section, based on the correlation of trends in each section until the end of the biomere (Pt_T). The resulting chemostratigraphic boundary (Cs_3) reinforces the notion that the Corset Springs member comprises a condensed section following the Sauk II-III boundary.

The resulting plot yields a relatively conformable overlay of carbon isotopic data from both sections (Fig. 24). Using the same coeval boundaries, an overlay of

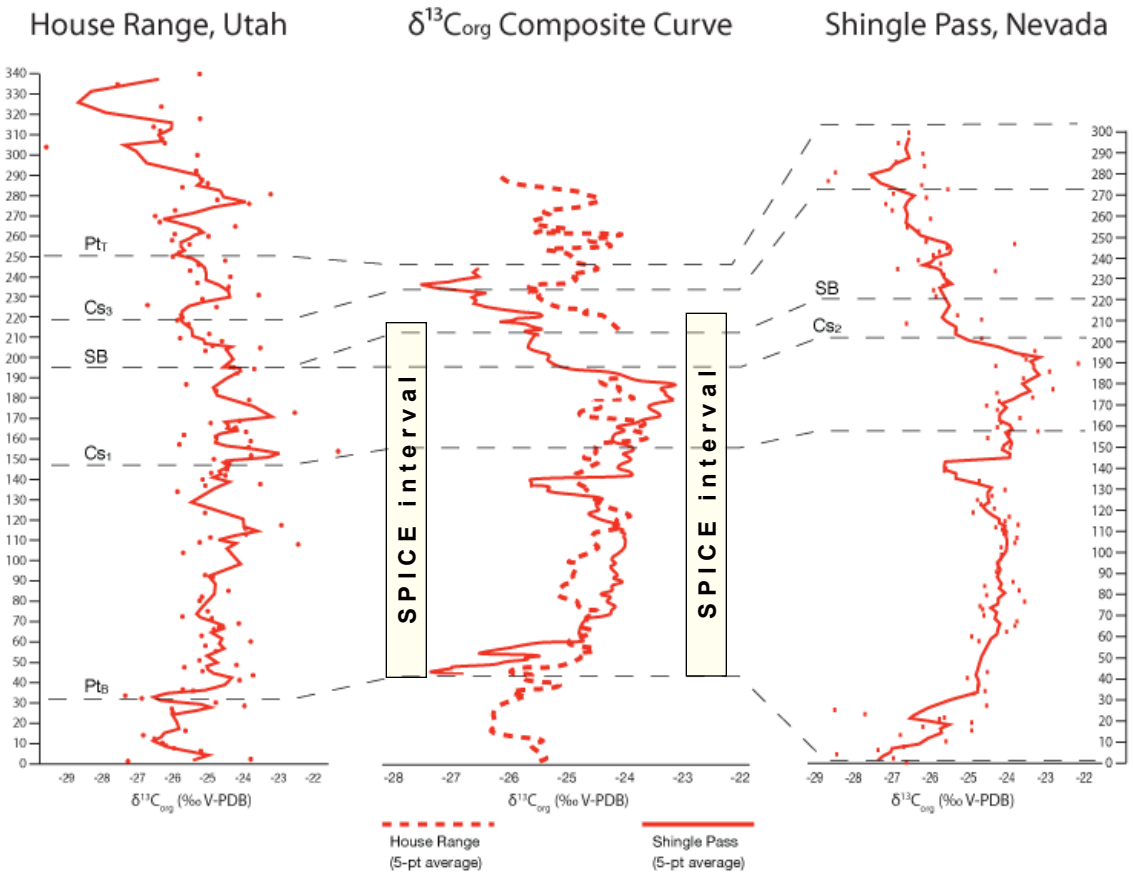

Figure 26: Time-equivalent overlay of $\delta^{13}C_{org}$ from each section, based on interpreted coeval boundaries: top (Pt_T) and base (Pt_B) of the Pterocephaliid biomere; Sauk II/III sequence boundary (SB); peak values of the SPICE event (Cs_1); base of the falling limb of the SPICE event (Cs_2); and a minor peak in the post-SPICE interval (Cs_3).

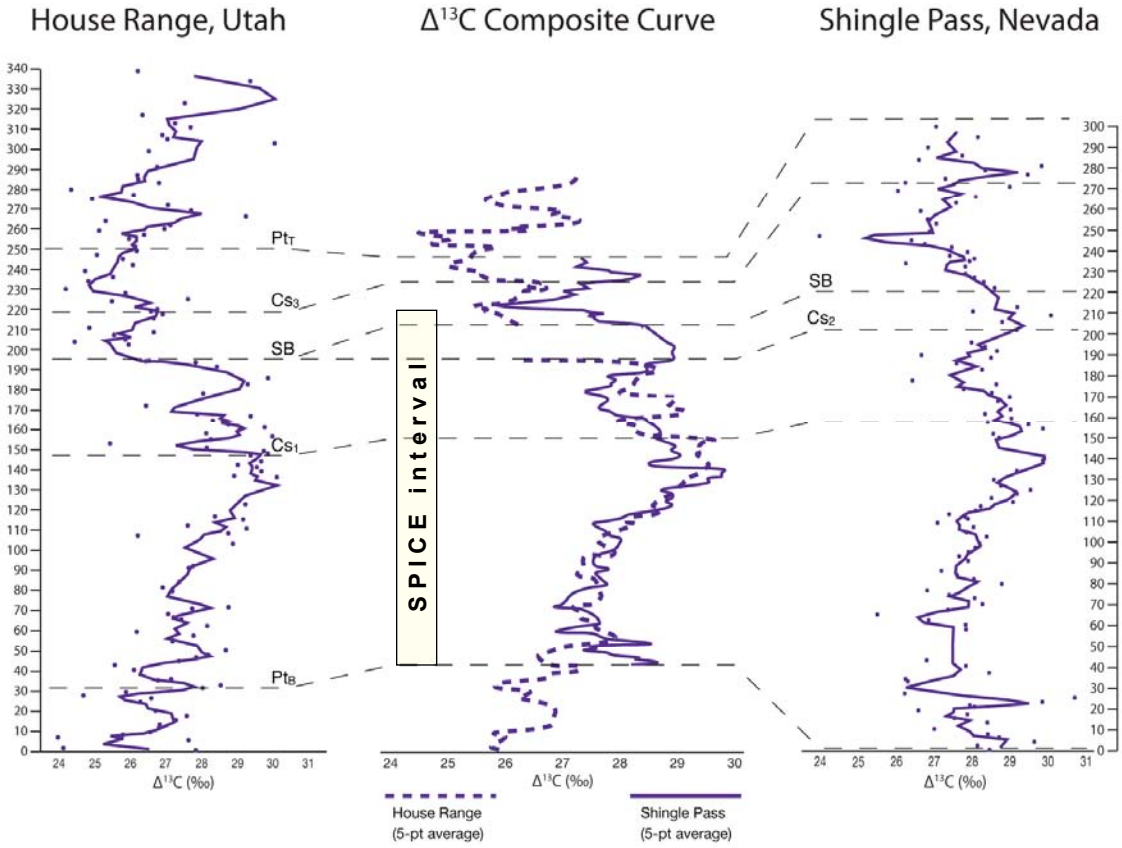

Figure 27: Time-equivalent overlay of $\Delta^{13}C$ from each section, based on interpreted coeval boundaries: top (Pt_T) and base (Pt_B) of the Pterocephaliid biomere; Sauk II/III sequence boundary (SB); peak values of the SPICE event (Cs_1); base of the falling limb of the SPICE event (Cs_2); and a minor peak in the post-SPICE interval (Cs_3).

trends in isotopic data was made for $\delta^{13}C_{org}$ (Fig. 26) and $\Delta^{13}C$ (Fig. 27). The overlay of $\Delta^{13}C$ trends within analytical reproducibility across the SPICE interval suggests a regional control on carbon isotopic fractionation, and confirms our suspicion that the discrepancy in $\delta^{13}C_{carb}$ between Pt_B and Cs_1 is due to a difference in sampling resolution. The only discordant interval lies between SB and Pt_T, which displays a parallel but offset trend in $\Delta^{13}C$. The difference is illustrated in Figure 27, where the House Range section records $\delta^{13}C_{org}$ values

approximately 1.5‰ higher (less negative) than at Shingle Pass. The exact origin for this difference is difficult to clarify, but higher $\delta^{13}C_{org}$ values in House Range is associated with a lithological change from carbonate to siliciclastics, likely recording an influence from ^{13}C-enriched detrital organic matter (e.g. Tribovillard et al., 2009).

7.3 Implications for organic carbon burial and feedbacks in marine geochemical cycles

The parallel positive excursion in $\delta\ ^{13}C_{org}$ is consistent with model predictions regarding enhanced organic burial as the primary forcing mechanism of the SPICE event (Saltzman et al., 1998; Glumac and Walker, 1998; Kump and Arthur, 1999). This model requires a significant amount of organic carbon to be buried beyond steady state, which may be explained by a moderate increase in the burial fraction of organic matter (f_{org}) over the SPICE interval (Kump and Arthur, 1999). Long-term sequestration of organic carbon would result in a reduction in atmospheric carbon dioxide (Siegenthaler and Sarmiento, 1993; Damsté et al., 2008) and presumably global temperatures (e.g. Pearson and Palmer, 2000; Yang et al., 2009). The preservation and burial of marine organic matter also provides a significant source of oxygen to the ocean-atmosphere system (Berner and Canfield, 1989; Hayes and Waldbauer, 2006). Implementing data from organic carbon isotopes allows us to more closely examine the marine geochemical implications of the SPICE event, and begin to quantify the effect.

Using the model of Kump and Arthur (1999), Saltzman et al. (2004) estimated that more than 120,000 Gt C (10^{19} mol C) may have been buried beyond steady state during the SPICE event. This assumes marine carbon reservoirs near modern values, a constant riverine input of carbon (δ_w = -5‰) and constant fractionation ($\Delta^{13}C$ = 30‰), and is calculated by doubling f_{org} over 3 million years. Adjusting for variable $\Delta^{13}C$ (from this study), the estimated range of organic carbon burial rates during the late Cambrian (2-4 x 10^{18} mol/m.y.; Berner and Canfield, 1989) and duration of the SPICE event (2-4 m.y.; Saltzman et al., 1998) yields a lower limit of approximately 60,000 Gt C (5 x 10^{19} mol C). However, even this value is nearly an order of magnitude larger than the average estimated mass of CO_2 in the late Cambrian atmosphere (~11,400 Gt C or 4,500 ppm; Berner et al., 2003; 2006) and nearly twice the size of the modern DIC reservoir (38,000 Gt C; Siegenthaler and Sarmiento, 1993), leaving an open question as to the source of excess carbon.

According to the same model, drawdown of atmospheric CO_2 could have been more than 6,500 Gt C, effectively reducing pCO_2 from ~4,500 ppm to less than 2,000 ppm. Such a reduction in pCO_2 may effectively increase oceanic pH by 0.2-0.3 units (Zeebe and Wolf-Gladrow, 2001), assuming a Ca^{2+} concentration near 13.4 mg/L (Berner et al., 1983; Berner, 2004) and DIC reservoir size of 38,000 Gt C. This change in oceanic pH is approximately the variation seen in recent glacial-interglacial cycles (Hönisch and Hemming, 2005; Foster, 2008) and translates to a ~33% reduction in the size of the DIC at equilibrium, based solely on the saturation state of calcite (Bristow and Kennedy, 2008). Though various

negative feedbacks may dampen the DIC size reduction, including the enhanced precipitation of calcite (Hönisch and Hemming, 2005), applying Kump and Arthur's (1999) model to the SPICE event implies that carbonate production could have remained healthy in the shallow shelf, despite enhanced anoxia in the deep ocean. Increasing pH would also increase Fe-availability, which is limiting in the modern equatorial surface ocean where nitrate and phosphate are abundant (Behrenfeld et al., 1996).

High marine productivity may contribute to ocean anoxia through the increased degradation of organic matter, thereby promoting the preservation of organic matter in the water column (Tribovillard et al., 2009). Paradoxically, most marine organic matter is buried in shallow, oxic environments along coastal margins (Berner and Canfield, 1989), but carbon burial may shift to the deeper ocean during periods of extensive anoxia (Arthur et al., 1988). Modern studies reveal that the O_2 content of the water column does not significantly affect the rate of organic burial in marine sediments since other oxidants (e.g. NO_3 and SO_4) are readily available, but that organic carbon burial is more closely tied to sedimentation rate through an exponential relationship at rates less than 4 cm/ kyr (Betts and Holland, 1991).

The long-term maxima in $^{87}Sr/^{86}Sr$ (Montañez et al., 2000) and minima in relative sea level over the craton (Saltzman et al., 2004) are consistent with the notion that continental weathering and sedimentation rates also peaked with the SPICE event. The $^{87}Sr/^{86}Sr$ isotopic composition of seawater increased steadily throughout the Neoproterozoic (Galindo et al., 2004), reaching a maximum value

of 0.7094 during the Steptoean stage (Montañez et al., 2000) before falling substantially toward the Cambro-Ordovician boundary (Ebneth et al., 2001). This ratio is inversely proportional to sea level (Montañez et al., 1996), since eustatic regression exposes a larger percentage of high-$^{87}Sr/^{86}Sr$ cratonic rocks. Supporting this interpretation, Saltzman et al. (1995) documented a rapid decrease in $^{87}Sr/^{86}Sr$ from 0.70925 to 0.7091 following the SPICE event, which coincided with a continent-wide transgression that immediately preceded the faunal turnover at the *Irvingella major* subzone. At the same time, the Alum Shale in Scandinavia provides at least one example of extensive carbon burial in the deep ocean over the SPICE interval (Ahlberg et al., 2009).

The expansion of O_2-minimum zones also contributes heavily to nitrate removal from surface waters (Betts and Holland, 1991) and provides a strong negative feedback on overall marine productivity. Thus Saltzman et al. (2005) hypothesized that large, positive $\delta^{13}C$ excursions result from periods of phosphate-limiting oceans, in which ocean anoxia provides a positive feedback to nutrient cycling and production. More reducing conditions would contribute to the preferential speciation of ferrous iron (Fe^{2+}), and since marine phosphate is typically buried through complexes with ferric hydroxide ($Fe(OH)_3$) and apatite (Bjerrum et al., 2002), a decrease in mineral-bound phosphate may suggest expanding anoxic conditions in the respective basin. Mort et al., (2007) documented this phenomenon during the Cretaceous oceanic anoxic event (OAE) 2, where a peak in sedimentary phosphate actually preceded the $\delta^{13}C_{carb}$ excursion. This model also implies that O_2 released as a result of excess carbon

burial could provide a viable negative feedback to marine productivity (by limiting phosphate availability) and excess carbon burial in the deep oceans.

Each mole of carbon sequestered through excess organic burial translates to one mol O_2 released according to general equation for organic carbon fixation/ degradation:

$$CO_2 + H_2O \leftrightarrow CH_2O + O_2$$

Thus more than 6 x 10^{18} mol O_2 (or ~15% the mass of atmospheric O_2; Berner et al., 2006) may have been released to the ocean-atmosphere system over the course of the SPICE event — a conservative estimate, which does not include the effect of excess pyrite burial (Berner and Canfield, 1989; Gill et al., 2007). While this potentially corresponds to a burst in atmospheric oxygen from ~20% to more than 23%, a significant portion of this mass would presumably be taken up by the changing redox state of the ocean (Hayes and Waldbauer, 2006). Significant cooling of the global oceans may also allow for additional oxygen storage up to 22 µmol kg-1 C-1 (Keeling and Garcia, 2002), though this only amounts to a negligible 4.7 x 10^{14} g O_2 per °C of cooling. Further investigations into the redox evolution of the late Cambrian ocean may help differentiate these respective effects on the ocean-atmosphere system. Nonetheless, our results to date have important implications for the modeling of CO_2 and O_2 over time.

7.4 Carbon isotopic fractionation during the SPICE event

The House Range and Shingle Pass sections document a significant increase (~2‰-3‰) in $\Delta^{13}C$ across the SPICE event, which is contrary to model

predictions citing CO_2-drawdown as a cause of decreased fractionation (Kump and Arthur, 1999). In modern experimental studies, increases in photosynthetic fractionation during carbon fixation have been shown to result from small cell diameter (or small V/S ratios; Hayes et al., 1999), low nutrient supply/growth rate (Bidigare et al., 1997), high $[O_2]/[CO_2]$ mixing ratios (Berner et al., 2003), and CO_2 cell entry by passive diffusion alone — concomitant with high $[CO_2]/[HCO_3^-]$ ratios in seawater resulting from low T and high pH (Goericke and Fry, 1994; Hollander and McKenzie, 1991) — or the lack of a carbon-concentrating mechanism within the cell (Raven et al., 2002). Before one considers environmental controls, however, it is important to establish whether the conflicting $\Delta^{13}C$ trend simply reflects a shift in biomass contribution or ecological restructuring of the planktonic community.

Damsté and Schouten (1997) concluded that despite the persistent presence of biomarkers from chemoautotrophic producers (including sulfur-reducing bacteria and methanogens) in Phanerozoic sediments, the biomass contribution is small and inconsequential to values of $\delta^{13}C_{org}$ from TOC, even where bacterial biomarker concentrations range over 2 orders of magnitude (Schouten et al., 1997; Gong and Hollander, 1997). Given that organic matter in chemoautotrophic organisms can be heavily depleted in ^{13}C when compared to the DOC reservoir (e.g. Sakata et al., 2008; Zyakun et al., 2009), the negligible effect on $\delta^{13}C_{org}$ is counterintuitive, but may be explained by modern analog to a restricted, anoxic basin. From 60-100 m depth in the Black Sea occurs a suboxic mixing zone, in which chemoautotrophic biomass production is approximately

15% that of surface photosynthetic production (Karl and Knauer, 1991), though contributions up to 50% or more have been observed in the Southwest Gyre (Morgan et al., 2006). Despite a relative depletion of 4‰ in particulate organic matter (POM) within this mixing zone (Freeman et al., 1994; Fontugne et al., 2009), however, $\delta^{13}C_{POM}$ increases with depth below the chemocline, resulting in $\delta^{13}C_{org}$ values that more closely resemble surface production (Schouten et al., 2000).

In ancient coastal marine and lacustrine settings with a well-developed chemocline, typically characterized by a peak in chemoautotrophic production, the remineralization of organic matter contributed to a ~5‰ depletion of ^{13}C in aqueous CO_2 (Van Breugel et al., 2005). However, this affects equally $\delta^{13}C$ from carbonate and organic carbon. Furthermore, the contribution of isotopically light (respired) CO_2 to the surface water is typically less than 30%, and then only in restricted environments. Thus in well oxygenated, shallow-shelf environments, the effect of chemoautotrophic production on the $\delta^{13}C_{org}$ signal should be negligible (Bekker et al., 2008).

Dramatic shifts in the ecological structure of phytoplankton communities may occur on the decadal scale (Karl et al., 2010), accompanying environmental changes in nutrient availability or ocean stratification. The restructuring may also result from changes in atmospheric composition or salinity, and induce a selective pressure on the planktonic biomass toward smaller (low V/S ratio) species (Li et al., 2009; Feng et al., 2010), though without much change in overall production (Karl et al., 2010). Such a shift in dominant biota could inflate

carbon isotope fractionation (Hayes et al., 1999) and explain the higher values documented across the SPICE interval. While this hypothesis is difficult to test, enhanced phosphate delivery and higher oceanic pH would predict sufficient nutrient availability during the SPICE event (Behrenfeld et al., 1996; Saltzman et al., 2005). Global cooling as a result of CO_2 drawdown would also predict stronger upwelling and thermohaline circulation (Broecker, 1997). In the absence of continental ice-sheet buildup, a long-term change in ocean salinity is also unlikely. Therefore, the most parsimonious conclusion is that an ecological restructuring of marine primary producers did not accompany the SPICE interval, notwithstanding future studies that may document contrary evidence from temporal changes in biomarkers.

It is possible that the Cambrian DIC was up to 40% larger than today, adjusting the equilibrium carbonate alkalinity based on higher estimates of pCO_2 and the Revelle factor (Zeebe and Wolf-Gladrow, 2001), but independent proxies are not available for that time period. Nonetheless, a larger DIC would merely imply an even larger reduction in pCO_2 and less sensitivity to changes in pH as a result of higher carbonate buffering (Kump and Arthur, 1999; Bristow and Kennedy, 2008). A much larger DOC reservoir, on the other hand, would be buffered from isotopic shifts during major excursions in $\delta^{13}C_{carb}$ (e.g. Rothman et al., 2003; Fike et al., 2006; Swanson-Hysell et al., 2010). This could explain the reduced magnitude of the documented excursion in $\delta^{13}C_{org}$ for the SPICE event, but only at a reservoir size greater than that of the DIC (i.e. more than 60 times larger than the modern DOC). However, the high short-term variability seen in the

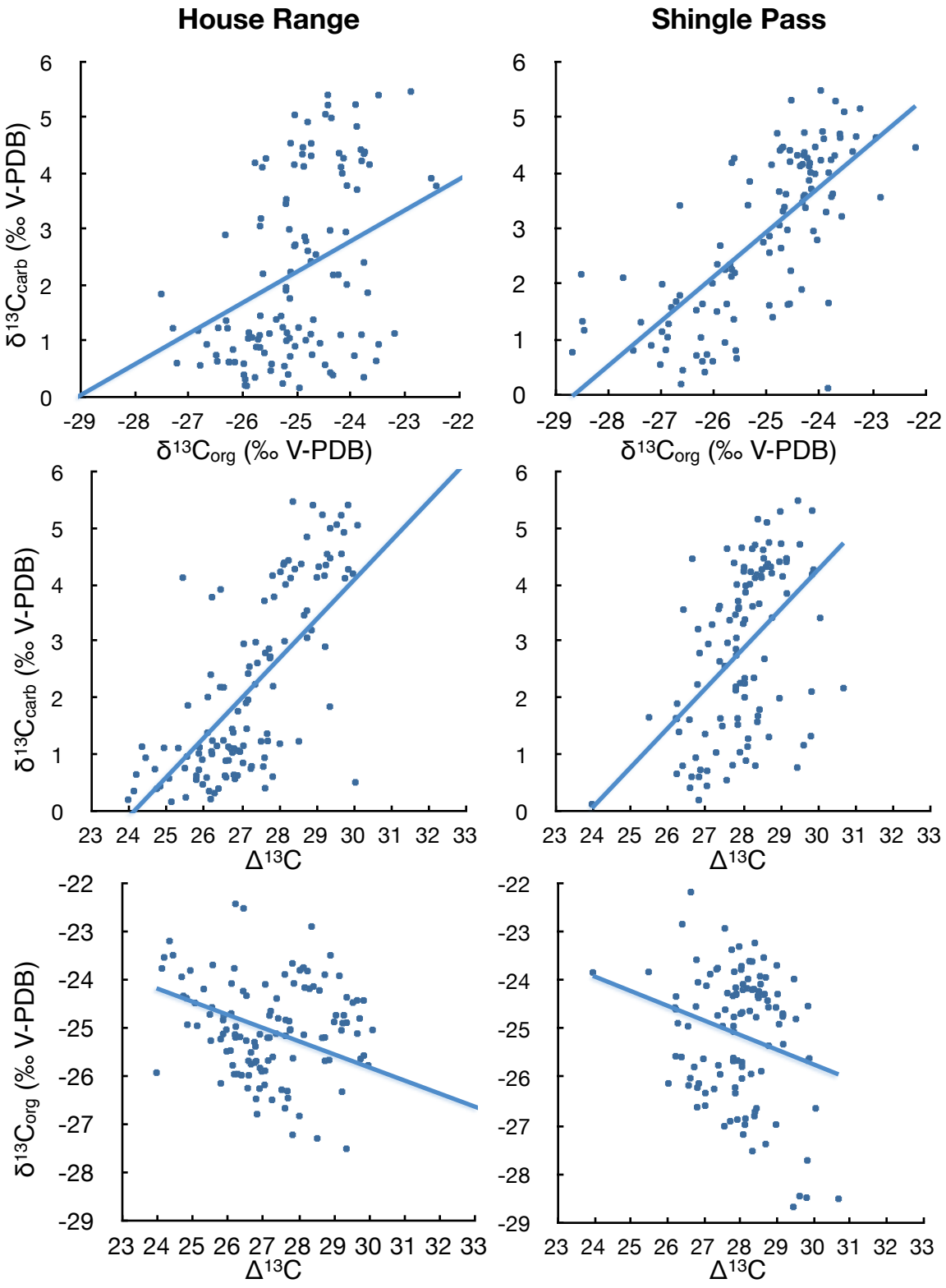

Figure 28: Cross plots of all carbon isotope data, illustrating a strong dependence of $\Delta^{13}C$ on both $\delta^{13}C_{carb}$ and $\delta^{13}C_{org}$. This represents a coupling of oceanic carbon reservoirs (DIC and DOC), and signifies that the respective reservoir sizes were near Cenozoic values (cf. Fig. 8 *in* Bekker et al., 2008).

$\delta^{13}C_{org}$ seems to contradict this notion. Furthermore, Figure 28 illustrates the strong dependence of $\Delta^{13}C$ on both carbon isotopic values, which Bekker et al. (2008) suggests is indicative of near-Cenozoic DIC and DOC reservoir sizes, in contrast to the much larger DOC reservoir of the Neoproterozoic (Fike et al., 2006; McFadden et al., 2008).

Phanerozoic trends in $\Delta^{13}C$ reveal higher values during geologic periods characterized by high O_2 and low CO_2, such as the Carboniferous (Berner et al., 2003). Long-term variation in $\Delta^{13}C$ has been interpreted to reflect the dependence of ε_p (photosynthetic fractionation) on the $[O_2]/[CO_2]$ mixing ratio in the atmosphere, since oxygen acts as a competitive inhibitor during carbon fixation in the Ribulose-1,5-bisphosphate carboxylase oxygenase (RuBisCO) cycle (Beerling et al., 2002). Saltzman et al. (2007) used the dependence to explain high fractionation values across the SPICE event as a result of increasing pO_2 in response to organic C burial (and pCO_2 drawdown). The explanation seems plausible, given a potential increase in $[O_2]/[CO_2]$ mixing ratio from ~40 to more than 180 (Fig. 29; compare to modern value of 600). However, Beerling et al. (2002) predicted a much lower effect at high pCO_2,

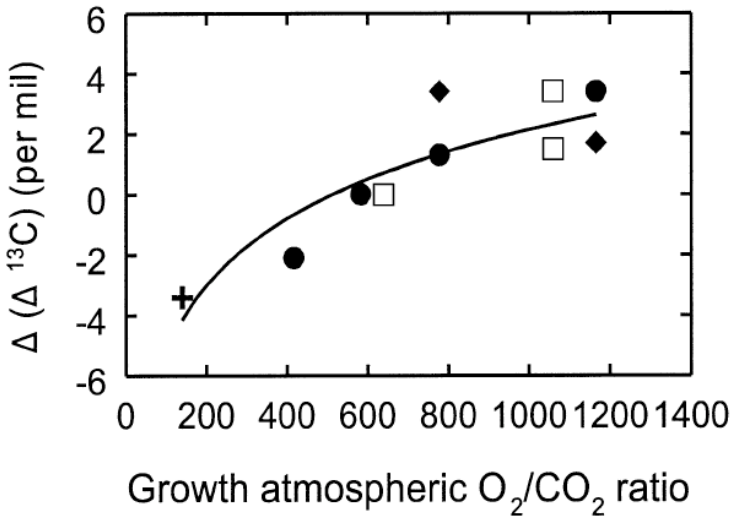

Figure 29: From Beerling et al. (2002), illustrating the sensitivity of $\Delta^{13}C$ to changes in the atmospheric mixing ratio of O_2 to CO_2.

when carbon is more readily available (see also Raven et al., 2005). Thus it is unlikely this effect could explain a 2-3‰ increase in fractionation during the greenhouse climate of the late Cambrian (Berner and Kothvala, 2001; Berner, 2006).

7.5 CO_2 limitation as a result of the SPICE event

Multiple lines of evidence from $\delta^{13}C$, $\delta^{34}S$, and $^{87}Sr/^{86}Sr$ suggest that high marine productivity characterized the onset of the SPICE event (Glumac and Walker, 1998; Gill et al., 2007; Montañez et al., 2000), as continental weathering input, enhanced ocean circulation, and feedbacks from ocean anoxia provided sufficient nutrient supply to the surface ocean (Saltzman et al., 2005). Furthermore, enhanced organic burial sequestered a significant amount of excess carbon from the ocean-atmosphere system over the 2.4 million-year interval, resulting in a major reduction of atmospheric CO_2. The abundance of inorganic carbon in the oceanic reservoir makes carbon an unusual suspect for growth limitation in photosynthetic organisms, but during productivity blooms or periods of low CO_2 (such as recent glacial cycles), CO_2 limitation may significantly decrease algal growth rates (Riebesell et al., 1993). Carbon isotopic fractionation in primary producers is strongly tied to growth rate (Bidigare et al., 1997; Hayes et al., 1999), which determines the relative intake of inorganic carbon species for photosynthesis (Raven et al., 2002). Furthermore, the large marine DIC allows for high sustainable production and biomass, which is rather limited by nitrate and phosphate availability (Riebesell et al., 1993; Marinov et al.,

2010), despite CO_2 limitation of individual cell growth, implying that CO_2 limitation may provide a viable explanation of isotopic data that is consistent with existing models of the SPICE event.

In nearly all modern photosynthetic organisms, a sufficient intracellular carbon pool is regulated by a carbon-concentrating mechanism (CCM) (Raven et al., 2008a; Badger et al., 2002). Organisms use CCM's to facilitate the intake of HCO_3^-, which is converted within the cell, or actively convert CO_2 that entered by diffusive entry (Tchernov et al., 1998; Diaz and Maberly, 2009). Raven et al. (2008a) noted that CCMs may have evolved independently at least 20 times in C3 organisms alone, possibly in response to periods of limited atmospheric CO_2. While the several glacial episodes in the Proterozoic were characterized by low CO_2/O_2, and may account for an early presence of CCMs in some cyanobacteria, most pathways evolved within the last 20-30 million years (Raven et al., 2008b). However, the absence of identifiable fossil evidence (including biomarkers) for the presence of various CCMs complicates the question of when such processes arose (Raven et al., 2008b). Low atmospheric oxygen, such as in the Paleoproterozoic, negates the selective pressure of CO_2 limitation that may have been seen during early glaciations (Raven et al., 2008b), thereby shifting the focus to oxidation events such as the Ediacaran (Bristow and Kennedy, 2008), or the Carboniferous (Badger et al., 2002).

Photosynthetic organisms have also developed Rubisco pathways with a high affinity for CO_2, more so when a CCM is not present (Badger et al., 1998), implying that all organisms are adapted to relatively low concentrations of CO_2 in

the modern atmosphere. Raven et al. (2005) speculate as to whether these pathways derive from a single ancestral point, given the widespread occurrence in higher orders of taxa, while Badger et al. (2002) suggest polyphyletic evolution, particularly near ~400 Ma, when CO_2 began to fall sharply at the diversification of early land plants (Berner and Kothvala, 2001). However, this hypothesis is predicated in that the Carboniferous atmosphere incurred selective pressure on the evolution of carbon-acquisition in primary producers, and does not consider earlier periods when perturbations in the carbon cycle, such as the SPICE event, may have produced similar conditions over several million years.

The potential absence of CCMs or lower CO_2 affinity of Rubisco cycles in many organisms before the Carboniferous has important implications for interpreting trends in carbon isotopic fractionation during the late Cambrian. If these organisms were adapted to the super greenhouse climate that preceded the SPICE event without having developed CCMs, then growth could have been limited by major reductions in CO_2, producing higher values of $\Delta^{13}C$ documented here for this interval. Photosynthetic discrimination of carbon isotopes (ε_p) is exponentially proportional to the C_e/C_i ratio, where C_e and C_i represent the extracellular and intercellular concentrations of CO_2, respectively (Farquhar et al., 1982). Depending on rates of photosynthesis, C_i can vary substantially in organisms acquiring CO_2 by passive diffusion alone (Badger et al., 1998). Experiments in acidophilic algae lacking a CCM show a strong dependence of growth rate on CO_2, with a relatively high half-saturation point ($K_{1/2}$) with respect to CO_2 availability (Diaz and Maberly, 2009). There is also some evidence that

marine and freshwater algae lacking a CCM do take in HCO_3^- alongside CO_2 by passive diffusion (Raven et al., 2005), which produces such a dependence of ε (and thus $\Delta^{13}C$) on growth rate. Even for organisms that may have developed CCMs by this time (such as cyanobacteria; Badger et al., 2002), however, periods of low CO_2 cause energy-demanding CCMs to detract from overall cell growth (Barcelos e Ramos et al., 2010; Krief et al., 2010). Thus while increasing values of $\delta^{13}C_{org}$ on long-term scales may have been related to higher utilization of CCMs in the marine biota, such as during the Cenozoic (Raven et al., 2008a), geologically short-term intervals of environmental stress through CO_2-limitation could have produced the opposite effect before the widespread development of such mechanisms in the Carboniferous.

CHAPTER 8

CONCLUSIONS

Paired $\delta^{13}C_{carb}$ and $\delta^{13}C_{org}$ data from the Great Basin reveal a moderately significant covariation of $\delta^{13}C_{carb}$ and $\delta^{13}C_{org}$ across the record of the SPICE event. The covariation is consistent with model predictions regarding enhanced organic carbon burial as the primary mechanism of the positive carbon isotope excursion. The dependence of temporal trends in $\Delta^{13}C$ on carbon isotope values from both carbonate and organic carbon signifies the coupling of oceanic carbon reservoirs (DIC and DOC), and also implies that the Cambrian ocean was transitional between that of the Proterozoic and later Phanerozoic with regard to the size of respective marine carbon reservoirs. Assuming near-modern carbon reservoir sizes, therefore, the amount of carbon sequestered from the ocean-atmosphere system during the ~2.4 million-year perturbation to the carbon cycle would have been sufficient to cause a major reduction in atmospheric CO_2 during the super-greenhouse climate of the late Cambrian. The sharp decrease in the difference between $\delta^{13}C$ values from carbonate and organic carbon ($\Delta^{13}C$) seen after the peak of the SPICE event is consistent with this hypothesis.

A 2-3‰ increase in the difference between carbonate and organic carbon isotopes ($\Delta^{13}C$) was recorded in the interval preceding the peak of the SPICE event. This trend, while paradoxical, helps to constrain the biotic response to major climatic and oceanographic changes resulting from enhanced organic burial during the early Paleozoic. While decreasing pCO_2 typically produces a decrease in carbon isotopic fractionation, due to the enhanced uptake of ^{13}C-

enriched HCO_3^-, the effect is negligible at very high (>2,000 ppm) concentrations of atmospheric CO_2. Rather, high marine productivity and organic burial that characterized the onset of the SPICE event may have caused CO_2-limitation of growth in photosynthetic organisms lacking a CCM, thereby producing the opposite effect. In the absence of supporting data from global, coeval sections, however, this interpretations is tentative upon further examination.

REFERENCES CITED

Ahlberg, P., Axheimer, N., Babcock, L.E., Eriksson, M.E., Schmitz, B., Terfelt, F., 2009, Cambrian high-resolution biostratigraphy and carbon isotope chemostratigraphy in Scania, Sweden: first record of the SPICE and DICE excursions in Scandinavia: Lethaia, v. 42, p. 2-16.

Allan, J.R., and Matthews, R.K., 1982, Isotope signatures associated with early meteoric diagenesis: Sedimentology, v. 29, p. 797-817.

Álvaro, J., Bauluz, B., Subías, I., Pierre, C., Vizcaïno, D., 2008, Carbon chemostratigraphy of the Cambrian-Ordovician transition in a midlatitude mixed platform, Montagne Noire, France: Geological Society of America Bulletin, v. 120, p. 962-975.

Amieux, P., Bernier, P., Dalongeville, R., Medwecki, V., 1989, Cathodoluminescence of carbonate-cemented Holocene beachrock from the Togo coastline (West Africa) an approach to early diagenesis: Sedimentary Geology, v. 65, p. 261-272.

Arthur, M.A., Dean, W.E., Pratt, L.M., 1988, Geochemical and climatic effects of increased marine organic burial at the Cenomanian/Turonian boundary: Nature, v. 335, p. 714-717.

Auerbach, D.J., 2004, The Steptoean Positive Isotopic Carbon Excursion (SPICE) in siliciclastic facies of the Upper Mississippi Valley: Implications for mass extinction and sea level change in the Upper Cambrian [B.A. Thesis]: Carleton College, 35 p.

Badger, M.R., Andrews, T.J., Whitney, S.M., Ludwig, M., Yellowlees, D.C., Leggat, W., Price, G.D., 1998, The diversity and coevolution of Rubisco, plastids, pyrenoids, and chloroplast-based CO_2-concentrating mechanisms in algae: Canadian Journal of Botany, v. 76, p. 1052-1071.

Badger, M.R., Hanson, D., Price, G.D., 2002, Evolution and diversity of CO_2 concentrating mechanisms in cyanobacteria: Functional Plant Biology, v. 29, p. 161-173.

Barcelos e Ramos, J., Mueller, M. N., Riebesell, U., 2010, Short-term response of the coccolithophore Emiliania huxleyi to an abrupt change in seawater carbon dioxide concentrations: Biogeosciences, v. 7, p. 177-186.

Behrenfeld, M.J., Bale, A.J., Kolber, Z.S., Aiken, J., Falkowski, P.G., 1996, Confirmation of iron limitation of phytoplankton photosynthesis in the equatorial Pacific Ocean: Nature, v. 383, p. 508-511.

Bekker, A., Holmden, C., Beukes, N.J., Kenig, F., Eglingtone, B., Patterson, W.P., 2008, Fractionation between inorganic and organic carbon during the Lomagundi (2.22–2.1 Ga) carbon isotope excursion: Earth and Planetary Science Letters, v. 271, p. 278-291.

Berger, A., 1978, Long-term variations of caloric insolation resulting from the earth's orbital elements: Quaternary Research, v. 9, p. 139-167.

Beerling, D.J., Lake, J.A., Berner, R.A., Hickey, L.J., Taylor, D.W., Royer, D.L., 2002, Carbon isotope evidence implying high O_2/CO_2 ratios in the Permo-Carboniferous atmosphere: Geochimica et Cosmochimica Acta, v. 66, p. 3757-3767.

Berner, R.A., and Canfield, D.E., 1989, A new model for atmospheric oxygen over Phanerozoic time: American Journal of Science, v. 289, p. 333-361.

Berner, R.A., and Kothavala, Z., 2001, GEOCARB III: a revised model of atmospheric CO_2 over Phanerozoic time: American Journal of Science, v. 301, p. 182–204.

Berner, R.A., Beerling, D.J., Dudley, R., Robinson, J.M., Wildman, R.A., 2003, Phanerozoic Atmospheric Oxygen: Annual Reviews in Earth and Planetary Science, v. 31, p. 105-134.

Betts, J. N., and Holland, H. D., 1991, The oxygen content of ocean bottom waters, the burial efficiency of organic carbon, and the regulation of atmospheric oxygen: Palaeogeography, Palaeoclimatology, Palaeoecology, v. 97, p. 5-18.

Bidigare, R.R., Fluegge, A., Freeman, K.H., Hanson, K.L., Hayes, J.M., Hollander, D., Jasper, J.P., King, L.L., Laws, E.A., Milder, J., Millero, F.J., Pancost, R., Popp, B.N., Steinberg, P.A., Wakeham, S.G., 1997, Consistent fractionation of ^{13}C in nature and in the laboratory: growth-rate effects in some haptophyte algae: Global Biogeochemical Cycles, v. 11, p. 279–292.

Bjerrum, C.J., and Canfield, D.E., 2002, Ocean productivity before about 1.9 Gyr ago limited by phosphorus adsorption onto iron oxides: Nature, v. 417, p. 159-162.

Bond, G.C., Kominz, M.A., Devlin, W.J., 1983, Thermal subsidence and eustasy in the Lower Paleozoic miogeocline of western North America: Nature, v. 306, p. 775-779.

Bond, G.C., Kominz, M.A., Grotzinger, J.P., 1988, Cambro-Ordovician Eustasy: evidence from geophysical modeling of subsidence in Cordilleran and Appalachian passive margins: New Perspectives in Basin Analysis, p. 129-161.

Brasier, M.D., 1993, Towards a carbon isotope stratigraphy of the Cambrian system: potential of the Great Basin succession, *in* Hailwood, E.A., and Kidd, R.B., eds., High Resolution Stratigraphy: Geological Society of London, Special Publication 70, p. 341–359.

Bristow, T.F., and Kennedy, M.J., 2008, Carbon isotope excursions and the oxidant budget of the Ediacaran atmosphere and ocean: Geology, v. 36, p. 863-866.

Broecker, W.S., 1997, Thermohaline Circulation, the Achilles Heel of Our Climate System: Will Man-Made CO_2 Upset the Current Balance?: Science, v. 278, p. 1582-1588.

Burns, F.E., Burley, S.D., Gawthorpe, R.L., Pollard, J.E., 2005, Diagenetic signatures of stratal surfaces in the Upper Jurassic Fulmar Formation, Central North Sea, UKCS: Sedimentology, v. 52, p. 1155-1185.

Catuneanu, O., Abreu, V., Bhattacharya, J.P., Blum, M.D., Dalrymple, R.W., Eriksson, P.G., Fielding, C.R., Fisher, W.L., Galloway, W.E., Gibling, M.R., Giles, K.A., Holbrook, J.M., Jordan, R., Kendall, C.G.St.C., Macurda, B.,

Martinsen, O.J., Miall, A.D., Neal, J.E., Nummedal, D., Pomar, L., Posamentier, H.W., Pratt, B.R., Sarg, J.F., Shanley, K.W., Steel, R.J., Strasser, A., Tucker, M.E., Winker, C., 2009, Towards the standardization of sequence stratigraphy: Earth Science Reviews, v. 92, p. 1-33.

Chen, F., Zhang, L., Yang, Y., Zhang, D., 2008, Chemical and isotopic alteration of organic matter during early diagenesis: Evidence from the coastal area off-shore the Pearl River estuary, south China: Journal of Marine Systems, v. 74, p. 372-380.

Cook, H.E., and Taylor, M.E., 1977, Comparison of continental slope and shelf environments in the upper Cambrian and lowest Ordovician of Nevada: The Society of Economic Paleontologists and Mineralogists, Special Publication No. 25, p. 51-81.

Cowan, C.A., Fox, D.L., Runkel, A.C., Saltzman, M.R., 2005, Terrestrial-marine carbon cycle coupling in ~500-m.y.-old phosphatic brachiopods: Geology, v. 33, p. 661-664.

Cramer, B.D., and Saltzman, M.R., 2007, Early Silurian paired $\delta^{13}C_{carb}$ and $\delta^{13}C_{org}$ analyses from the Midcontinent of North America: Implications for paleoceanography and paleoclimate: Palaeogeography, Palaeoclimatology, Palaeoecology, v. 256, p. 195-203.

Cramer, B.D., Salztman, M.R., Day, J.E., Witzke, B.J., 2008, Record of the Late Devonian Hangenberg global positive carbon isotope excursion in an epeiric sea setting: carbonate production, organic-carbon burial and

paleoceanography during the Late Famennian: Special Paper - Geological Association of Canada, v. 48, p. 103-118.

Damsté, J.S.S., and Schouten, S., 1997, Is there evidence for a substantial contribution of prokaryotic biomass to organic carbon in Phanerozoic carbonaceous sediments?: Organic Geochemistry, v. 26, p. 517-530.

Damsté, J.S.S., Kuypers, M.M.M., Pancost, R.D., Schouten, S., 2008, The carbon isotopic response of algae, (cyano)bacteria, archaea and higher plants to the late Cenomanian perturbation of the global carbon cycle: Insights from biomarkers in black shales from the Cape Verde Basin (DSDP Site 367): Organic Geochemistry, v. 39, p. 1703-1718.

Diaz, M., and Maberly, S.C., 2009, Carbon-concentrating mechanisms in acidophilic algae: Phycologia, v. 48, p. 77–85.

Dickinson, W.R., 2006, Geotectonic evolution of the Great Basin: Geosphere, v. 2, p. 353-368.

Ebneth, S., Shields, G. A., Veizer, J., Miller, J. F., Shergold, H., 2001, High-resolution strontium isotope stratigraphy across the Cambrian-Ordovician transition: Geochimica et Cosmochimica Acta, v. 65, no. 14, p. 2273–2292.

Evans, K.R., 1997, Stratigraphic expression of Middle and Late Cambrian sea-level changes: Examples from Antarctica and the Great Basin, USA [Ph.D. Dissertation]: Lawrence, Kansas, University of Kansas, 177 p.

Farquhar, G. D., O'Leary, M.H., Berry, J.A., 1982, On the relationship between carbon isotope discrimination and the intercellular carbon dioxide

concentration in leaves: Australian Journal of Plant Physiology, v. 13, p. 281-292.

Feng, R., Hare, C.E., Rose, J.M., Handy, S.M., DiTullio, G.R., Lee, P.A., Smith, Jr., W.O., Peloquin, J., Tozzi, S., Sun, J., Zhang, Y., Dunbar, R.B., Long, M.C., Sohst, B., Lohan, M., Hutchins, D.A., 2010, Interactive effects of iron, irradiance and CO_2 on Ross Sea phytoplankton: Deep-Sea Research Part I, v. 57, p. 368-383.

Fike, D.A., Grotzinger, J.P., Pratt, L.M., Summons, R.E., 2006, Oxidation of the Ediacaran Ocean: Nature, v. 444, p. 744–747.

Fontugne, M., Guichard, F., Bentaleb, I., Strechie, C., Lericolais, G., 2009, Variations in ^{14}C reservoir ages of Black Sea waters and sedimentary organic carbon during anoxic periods: influence of photosynthetic versus chemoautotrophic production: Radiocarbon, v. 51, p. 969-976.

Foster, G. L., 2008, Seawater pH, pCO_2 and $[CO_3^{2-}]$ variations in the Caribbean Sea over the last 130 kyr: A boron isotope and B/Ca study of planktic foraminifera: Earth and Planetary Science Letters, v. 271, p. 254-266.

Frank, T. D., and Bernet, K., 2000, Isotopic signature of burial diagenesis and primary lithological contrasts in periplatform carbonates (Miocene, Great Bahama Bank): Sedimentology, v. 47, p. 1119-1134.

Freeman, K.H., and Hayes, J.M., 1992, Fractionation of carbon isotopes by phytoplankton and estimates of ancient pCO_2 levels: Global Biogeochemical Cycles, v. 6, p.629–644.

Galindo, C., Casquet, C., Rapela, C., Pankhurst, R.J., Baldo, E., Saavedra, J., 2004, Sr, C and O isotope geochemistry and stratigraphy of Precambrian and lower Paleozoic carbonate sequences from the Western Sierras Pampeanas of Argentina: tectonic implications: Precambrian Research, v. 131, p. 55-71.

Galy, V., Bouchez, J., France-Lanord, C., 2007, Determination of Total Organic Carbon Content and $\delta^{13}C$ in Carbonate-Rich Detrital Sediments: Geostandards and Geoanalytical Research, v. 31, p. 199-207.

Gao, G., and Land, L. S., 1991, Geochemistry of Cambrian-Ordovician Arbuckle Limestone, Oklahoma: Implications for diagenetic $\delta^{18}O$ alteration and secular $\delta^{13}C$ and $^{87}Sr/^{86}Sr$ variation: Geochimica et Cosmochimica Acta, v. 55, p. 2911–2920.

Gill, B.C., Lyons, T.W., Saltzman, M.R., 2007, Parallel, high-resolution carbon and sulfur isotope records of the evolving Paleozoic marine sulfur reservoir: Palaeogeography, Palaeoclimatology, Palaeoecology, v. 256, p. 156–173.

Glumac, B., and Walker, K.R., 1998, A Late Cambrian positive carbon-isotope excursion in the southern Appalachians: relation to biostratigraphy, sequence stratigraphy, environments of deposition, and diagenesis: Journal of Sedimentary Research, v. 68, no. 6, p. 1212-1222.

Goericke, R., Fry, B., 1994, Variations of marine plankton $\delta^{13}C$ with latitude, temperature, and dissolved CO_2 in the world ocean: Global Biogeochemical Cycles, v. 8, p. 85–90.

Gong, C., and Hollander, D.J., 1997, Differential contribution of bacteria to sedimentary organic matter in oxic and anoxic environments, Santa Monica Basin, California: Organic Geochemistry, v. 26, p. 545-563.

González, L.A., and Lohmann, K.C., 1985, Carbon and oxygen isotopic composition of Holocene reefal carbonates, Geology, v. 13, p. 811–814.

Hayes, J.M., Kaplan, I.R., and Wedeking, K.W., 1983, Precambrian organic geochemistry, preservation of the record, in Schopf, J.W., ed., The Earth's Earliest Biosphere: Its Origin and Evolution: Princeton, N.J., Princeton University Press, p. 93–134.

Hayes, J.M., Strauss, H., Kaufman, A.J., 1999, The abundance of ^{13}C in marine organic matter and isotopic fractionation in the global biogeochemical cycle of carbon during the past 800 Ma: Chemical Geology, v. 161, p. 103-125.

Hayes, J.M., and Waldbauer, J.R., 2006, The carbon cycle and associated redox processes through time: Philosophical Transactions of the Royal Society B, v. 361, p. 931–950.

Hintze, L.F., and Palmer, A.R., 1976, Upper Cambrian Orr Formation: Its subdivisions and correlatives in western Utah: U.S. Geological Survey Bulletin 1405-G, p. 1–25.

Hollander, D.J., and McKenzie, J.A., 1991, CO_2 control on carbon-isotope fractionation during aqueous photosynthesis: A paleo-CO_2 barometer: Geology, v. 19, p. 929-932.

Hönisch, B., and Hemming, N. G., 2005, Surface ocean pH response to variations in pCO_2 through two full glacial cycles: Earth and Planetary Science Letters, v. 236, p. 305-314.

Hurtgen, M.T., Pruss, S.B., Knoll, A.H., 2009, Evaluating the relationship between the carbon and sulfur cycles in the later Cambrian ocean: An example from the Port au Port Group, western Newfoundland, Canada: Earth and Planetary Science Letters, v. 281, p. 288-297.

Jaffrés, J.B.D., Shields, G.A., Wallmann, K., 2007, The oxygen isotope evolution of seawater: A critical review of a long-standing controversy and an improved geological water cycle model for the past 3.4 billion years: Earth-Science Reviews, v. 83, p. 83–122.

Junium, C.K., and Arthur, M.A., 2007, Nitrogen cycling during the Cretaceous, Cenomanian-Turonian Oceanic Anoxic Event II: Geochemistry Geophysics Geosystems, v. 8, no. 3, pp. 18.

Karl, D.M., and Knauer, G.A., 1991, Microbial production and particle flux in the upper 350 m of the Black Sea: Deep-Sea Research Part A, v. 38, p. S921-S942.

Karl, D.M., Bidigare, R.R., Leteller, R.M., 2001, Long-term changes in plankton community structure and productivity in the north Pacific Subtropical Gyre: The domain shift hypothesis: Deep Sea Research Part II: Topical Studies in Oceanography, v. 48, p. 1449-1470.

Kaufman, A.J., Hayes, J.M., Knoll., A.H., Germs, G.J.B., 1991, Isotopic compositions of carbonates and organic carbon from upper Proterozoic

successions in Namibia: stratigraphic variation and the effects of diagenesis and metamorphism: Precambrian Research, v. 49, p. 301-327.

Kaufman, A.J., and Xiao, S., 2003, High CO_2 levels in the Proterozoic atmosphere estimated from analyses of individual microfossils: Nature, v. 425, p. 279-281.

Keeling, R.F., and Garcia, H.E., 2002, The change in oceanic O_2 inventory associated with recent global warming: Proceedings of the National Academy of Sciences, v. 99, p. 7848-7853.

Kellogg, H.E., 1963, Paleozoic Stratigraphy of the Southern Egan Range, Nevada: Geological Society of America Bulletin, v. 74, p. 685-708.

Krief, S., Hendy, E.J., Fine, M., Yam, R., Meibom, A., Foster, G.L., Shemesh, 2010, Physiological and isotopic responses of scleractinian corals to ocean acidification: Geochimica et Cosmochimica Acta, v. 74, p. 4899-5001.

Kroopnick, P., 1974, Correlations between ^{13}C and ΣCO_2 in surface waters and atmospheric CO_2: Earth and Planetary Science Letters, v. 22, p. 397-403.

Kump, L.R., and Arthur, M.A., 1999, Interpreting carbon-isotope excursions; carbonates and organic matter: Chemical Geology, v. 161, p. 181-198.

Lara, R.J., Alder, V., Franzosi, C.A., Kattner, G., 2010, Characteristics of suspended particulate organic matter in the southwestern Atlantic: Influence of temperature, nutrient and phytoplankton features on the stable isotope signature: Journal of Marine Systems, v. 79, p. 199-209.

Li, W.K., McLaughlin, F.A., Lovejoy, C., Carmack, E.C., 2009, Smallest algae thrive as the Arctic Ocean freshens: Science, v. 326, p. 539.

Lindsay, J.F., Kruse, P.D., Green, O.R., Hawkins, E., Brasier, M.D., Cartlidge, J., Corfield, R.M., 2005, The Neoproterozoic–Cambrian record in Australia: A stable isotope study: Precambrian Research, v. 143, p. 113-133.

Lochman-Balk, C., 1974, Late Dresbachian (Late Cambrian) Biostratigraphy of North America: Geological Society of America Bulletin, v. 85, p. 135-140.

Ludvigsen, R., and Westrop, S.R., 1985, Three new Upper Cambrian stages for North America: Geology, v. 13: p. 139-143.

Lund, K., 2008, Geometry of the Neoproterozoic and Paleozoic rift margin of western Laurentia: Implications for mineral deposit settings: Geosphere, v. 4, p. 429-444.

Marinov, I., Doney, S.C., Lima, I.D., 2010, Response of ocean phytoplankton community structure to climate change over the 21st century: partitioning the effects of nutrients, temperature and light: Biogeosciences Discussions, v. 7, p. 4565-4606.

Michaelis, J., Usdowski, E., Menschel, G., 1985, Partitioning of ^{13}C and ^{12}C on the degassing of CO_2 and the precipitation of calcite — Rayleigh-type fractionation and a kinetic model: American Journal of Science, v. 285, p. 318-327.

Montañez, I.P., Banner, J.L., Osleger, D.A., Borg, L.E., Bosserman, P.J., 1996, Integrated Sr isotope variations and sea-level history of Middle to Upper

Cambrian platform carbonates: Implications for the evolution of Cambrian seawater $^{87}Sr/^{86}Sr$: Geology, v. 10, p. 917-920.

Montañez, I.P., Osleger, D.A., Banner, J.L., Mack, L.E., Musgrove, M., 2000, Evolution of the Sr and C Isotope Composition of Cambrian Oceans: Geological Society of America Today, v. 10, p. 1-7.

Morgan, J.A., Quinby, H.L., Ducklow, H.W., 2006, Bacterial abundance and production in the western Black Sea: Deep-Sea Research Part II: Topical Studies in Oceanography, v. 53, p. 1945-1960.

Mort, H.P., Adatte, T., Föllmi, K.B., Keller, G., Steinmann, P., Matera, V., Berner, Z., Stüben, D., 2007, Phosphorus and the roles of productivity and nutrient recycling during oceanic anoxic event 2: Geology, v. 35, p. 483-486.

Osleger, D., 1991a, Cyclostratigraphy of Late Cambrian carbonate sequences: an interbasinal comparison of the Cordilleran and Appalachian passive margins *in* Cooper, J.D., and Stevens, C.H., eds., 1991, Paleozoic Paleogeography of the Western United States-II: Pacific Section Society for Sedimentary Geology, v. 67, p. 811-828.

Osleger, D., 1991b, Subtidal carbonate cycles: Implications for allocyclic vs. autocyclic controls: Geology, v. 19, p. 917-920.

Osleger, D., and Read, J.F., 1991, Relation of eustasy to stacking patterns of meter-scale carbonate cycles, Late Cambrian, U.S.A.: Journal of Sedimentary Petrology, v. 61, p. 1225-1252.

Osleger, D.A., and Read, J.F., 1993, Comparative analysis of methods used to define eustatic variations in outcrop: Late Cambrian intrabasinal sequence development: American Journal of Science, v. 293, p. 157–216.

Pagani, M., 2002, The alkenone-CO_2 proxy and ancient atmospheric carbon dioxide: Philosophical Transactions of the Royal Society A, v. 360, p. 609.

Palmer, A.R., 1962, Glyptagnostus and associated trilobites in the United States: United States Geological Survey Professional Paper 374-F, p. 1-49.

Palmer, A.R., 1965a, Biomere — a new kind of biostratigraphic unit: Journal of Paleontology, v. 39, p. 149-153.

Palmer, A.R., 1965b, Trilobites of the Late Cambrian Pterocephaliid biomere in the Great Basin, United States: U.S. Geological Survey Professional Paper 493, p. 105.

Palmer, A.R., 1974, Search for the Cambrian world: American Scientist, v. 62, p. 216-224.

Palmer, A.R., 1981, Subdivision of the Sauk Sequence *In* Short Papers for the Second International Symposium on the Cambrian System: United States Geological Survey, Open-file Report 81-743, p. 160-162.

Palmer, A.R., 1984, The biomere problem — evolution of an idea: Journal of Paleontology, v. 58, p. 599-611.

Palmer, A.R., 1998, A proposed nomenclature for stages and series for the Cambrian of Laurentia: Canadian Journal of Earth Science, v. 35, p. 323-328.

Panchuk, K.M., Holmden, C.E., Leslie, S.A., 2006, Local controls on carbon cycling in the Ordovician midcontinent region of North America, with implications for carbon isotope secular curves: Journal of Sedimentary Research, v. 76, p. 200-211.

Patterson, W.P., and Walter, L.M., 1994, Depletion of ^{13}C in seawater ΣCO_2 on modern carbonate platforms: Significance for the carbon isotope record of carbonates: Geology, v. 22, p. 885–888.

Pearson, P.N., and Palmer, M.R., 2000, Atmospheric carbon dioxide concentrations over the past 60 million years: Nature, v. 406, p. 695-699.

Peng, S., Babcock, L.E., Robison, R.A., Lin, H., Rees, M.N., Saltzman, M.R., 2004, Global Standard Stratotype-section and Point (GSSP) of the Furongian Series and Paibian Stage (Cambrian): Lethaia, v. 37, p. 365-379.

Perfetta, P. J., Shelton, K. L., Stitt, J. H., 1999, Carbon isotope evidence for deepwater invasion at the Marjumiid-Pterocephaliid biomere boundary, Black Hills, USA: A common origin for biotic crises on Late Cambrian shelves: Geology, v. 27, p. 403-406.

Popp, B.N., Laws, E.A., Bidigare, R.R., Dore, J.E., Hanson, K.L., Wakeham, S.G., 1998, Effect of phytoplankton cell geometry on carbon isotopic fractionation: Geochimica et Cosmochimica Acta, v. 62, p. 69-77.

Prahl, F.G., De Lange, G.T., Scholten, S., Cowie, G.L., 1997, A case of postdepositional aerobic degradation of terrestrial organic matter in

turbidite deposits from the Madeira Abyssal Plain: Organic Geochemistry, v. 27, p. 141-152.

Price, G.D., 2010, Carbon-isotope stratigraphy and temperature change during the Early–Middle Jurassic (Toarcian–Aalenian), Raasay, Scotland, UK: Palaeogeography, Palaeoclimatology, Palaeoecology, v. 285, p. 255–263.

Pufahl, P. K., James, N.P., Kyser, T.K., Lukasik, J.J., Bone, Y., 2006, Brachiopods in epeiric seas as monitors of secular changes in ocean chemistry: a Miocene example from the Murray Basin, South Australia: Journal of Sedimentary Research, v. 78, p. 926-941.

Raven, J.A., Johnston, A.M., Kübler, J.E., Korb, R., McInroy, S.G., Handley, L.L., Scrimgeour, C.M., Walker, D.I., Beardall, J., Clayton, M.N., Vanderklift, M., Fredriksen, S., Dunton, K.H., 2002, Seaweeds in Cold Seas: Evolution and Carbon Acquisition: Annals of Botany, v. 90, p. 525-536.

Raven, J.A., Ball, L.A., Beardall, J., Giordano, M., Maberly, S.C., 2005, Algae lacking carbon-concentrating mechanisms: Canadian Journal of Botany, v. 83, p. 879-890.

Raven, J.A., Cockell, C.S., De La Rocha, C.L., 2008a, The evolution of inorganic carbon concentrating mechanisms in photosynthesis: Philosophical Transactions of the Royal Society B, v. 363, p. 2641-2650.

Raven, J.A., Giordano, M., Beardall, J., 2008b, Insights into the evolution of CCMs from comparisons with other resource acquisition and assimilation processes: Physiologia Plantarum, v. 133, p. 4–14.

Rees, M.N., Brady, M.J., Rowell, A.J., 1976, Depositional Environments of the Upper Cambrian Johns Wash Limestone (House Range, Utah): Journal of Sedimentary Petrology, v. 46, p. 38-47.

Rees, M.N., 1986, A fault-controlled trough through a carbonate platform: The Middle Cambrian House Range embayment: Geological Society of America Bulletin, v. 97, p. 1054–1069.

Riccardi, A., Kump, L.R., 2007, Carbon isotopic evidence for chemocline upward excursions during the end-Permian event: Palaeogeography, Palaeoclimatology, Palaeoecology, v. 248, p.73-81.

Riebesell, U., Wolf-Gladrow, D.A., Smetacek, V., 1993, Carbon dioxide limitation of marine phytoplankton growth rates: Nature, v. 361, p. 249-251.

Rothman, D.H., Hayes, J.M., Summons, R.E., 2003, Dynamics of the Neoproterozoic carbon cycle: Proceedings of the National Academy of Science, v. 100, p. 8124–8129.

Rowell, A.J. and Brady, M.J., 1976, Brachiopods and biomeres: Brigham Young University Geology Studies, v. 23, p. 165–180.

Sakata, S., Hayes, J.M., Rohmer, M., Hooper, A.B., Seemann, M., 2008, Stable carbon-isotopic compositions of lipids isolated from the ammonia-oxidizing chemoautotroph Nitrosomonas europaea: Organic Geochemistry, v. 39, p. 1725-1734.

Saltzman, M.R., Davidson, J.P., Holden, P., Runnegar, B., Lohmann, K.C., 1995, Sea-level-driven changes in ocean chemistry at an Upper Cambrian extinction horizon: Geology, v. 23, p. 893-896.

Saltzman, M.R., Runnegar, B., Lohmann, K.C., 1998, Carbon isotope stratigraphy of Upper Cambrian (Steptoean Stage) sequences of the eastern Great Basin; record of a global oceanographic event: Geological Society of America Bulletin, v. 110, p. 285-297.

Salztman, M.R., 1999, Upper Cambrian platform evolution, *Elvinia* and *Taenicephalus* zones (Pterocephaliid-Ptychaspid biomere boundary), northwestern Wyoming: Journal of Sedimentary Research, v. 69, p. 926-938.

Saltzman, M.R., Cowan, C.A., Runkel, A.C., Runnegar, B., Stewart, M.C., Palmer, A.R., 2004, The Late Cambrian SPICE $\delta^{13}C$ event and the Sauk II-Sauk III regression; new evidence from Laurentian basins in Utah, Iowa, and Newfoundland: Journal of Sedimentary Research, v. 74, p. 366-377.

Saltzman, M.R., 2005, Phosphorus, nitrogen, and the redox evolution of the Paleozoic oceans: Geology, v. 33, p. 573-576.

Saltzman, M.R., Young, S., Gill, B., Lyons, T., Kump, L., Runnegar, B., 2007, Increased carbon isotopic fractionation during the Late Cambrian SPICE event and a pulse of atmospheric oxygen: Abstracts with Programs - Geological Society of America, v. 39, pp. 24.

Schouten, S., Schoell, M., Rijpstra, W.I.C., Damsté, J.S.S., De Leeuw, J.W., 1997, A molecular stable carbon isotope study of organic matter in immature Miocene Monterey sediments, Pismo basin: Geochimica et Cosmochimica Acta, v. 61, p. 2065-2082.

Schouten, S., Van Kaam-Peters, H.M.E., Rijpstra, W.I.C., Schoell, M., Damsté, J.S.S., 2000, Effects of an oceanic anoxic event on the stable carbon isotopic composition of early Toarcian carbon: American Journal of Science, v. 300, p. 1-22.

Scotese, C.R., and McKerrow, W.S., 1990, Revised World maps and introduction: Palaeozoic Palaeogeography and Biogeography, Geological Society Memoir 12, p. 1–21.

Siegenthaler, U., and Sarmiento, J.L., 1993, Atmospheric carbon dioxide and the ocean: Nature, v. 365, p. 119-125.

Summons, R., Franzmann, P.D., and Nichols, P.D., 1998, Carbon isotopic fractionation associated with methylotrophic methanogenesis: Organic Geochemistry, v. 28, p. 465-475.

Swanson-Hysell, N.L., Rose, C.V., Calmet, C.C., Halverson, G.P., Hurtgen, M.T., Maloof, A.C., 2010, Cryogenian glaciation and the onset of carbon-isotope decoupling: Science, v. 328, p. 608-611.

Tang, Y., Huang, Y., Ellis, G.S., Wang, Y., Kralert, P.G., Gillaizeau, B., Ma, Q., Hwang, R., 2005, A kinetic model for thermally induced hydrogen and carbon isotope fractionation of individual n-alkanes in crude oil: Geochimica et Cosmochimica Acta, v. 69, p. 4505–4520.

Tchernov, D., Hassidim, M., Vardi, A., Luz, B., Sukenik, A., Reinhold, L., Kaplan, A., 1998, Photosynthesizing marine microorganisms can constitute a source of CO_2 rather than a sink: Canadian Journal of Botany, v. 76., p. 949-953.

Teece, M.A., and Fogel, M.L., 2007, Stable carbon isotope biogeochemistry of monosaccharides in aquatic organisms and terrestrial plants: Organic Geochemistry, v. 38, p. 458-473.

Theiling, B.P., Railsback, L.B., Holland, S.M., Crowe, D.E., 2007, Heterogeneity in Geochemical Expression of Subaerial Exposure in Limestones, and Its Implications for Sampling to Detect Exposure Surfaces: Journal of Sedimentary Research, v. 77, p. 159-169.

Tribovillard, N., Bout-Roumazeilles, V., Sionneau, T., Serrano, J.C.M., Riboulleau, A., Baudin, F., 2009, Does a strong pycnocline impact organic-matter preservation and accumulation in an anoxic setting? The case of the Orca Basin, Gulf of Mexico: Comptes Rendus - Geoscience, v. 341, p. 1-9.

Torsvik, T.H., Smethurst, M.A., Meert, J.G., Van der Voo, R., McKerro, W.S., Brasier, M.D., Sturt, B.A., Walderhaug, H.J., 1996, Continental break-up and collision in the Neoproterozoic and Palaeozoic — A tale of Baltica and Laurentia: Earth-Science Reviews, v. 40, p. 229-258.

Van Breugel, Y., Schouten, S., Paetzel, M., Ossebaar, J., Damsté, J.S.S., 2005, Reconstruction of $\delta^{13}C$ of chemocline CO_2 (aq) in past oceans and lakes using the $\delta^{13}C$ of fossil isorenieratene: Earth and Planetary Science Letters, v. 235, p. 421-434.

Wang, J., Jiang, G., Xiao, S., Li, Q., and Wei, Q., 2008, Carbon isotope evidence for widespread methane seeps in the ca. 635 Ma Doushantuo cap carbonate in south China: Geology, v. 36, p. 347-350.

Yang, H., Wang, F., Sun, A., 2009, Understanding the ocean temperature change in global warming: the tropical Pacific: Tellus, v. 61A, p. 371-380.

Young, S.A., Saltzman, M.R., Bergström, S.M., Leslie, S.A., Xu, C., 2008, Paired $\delta^{13}C_{carb}$ and $\delta^{13}C_{org}$ records of Upper Ordovician (Sandbian–Katian) carbonates in North America and China: Implications for paleoceanographic change: Palaeogeography, Palaeoclimatology, Palaeoecology, v. 270, p. 166-178.

Zeebe, R.E., and Wolf-Gladrow, D., 2001, CO_2 in seawater: Equilibrium, kinetics, isotopes: Amsterdam, Elsevier, 345 p.

Zhu, M.Y., Zhang, J.M., Li, G.X., Yang, A.H., 2004, Evolution of C isotopes in the Cambrian of China: implications for Cambrian subdivision and trilobite mass extinctions: Geobios, v. 37, p. 287–301.

Zhu, M.Y., Babcock, L.E., Peng, S.C., 2006, Advances in Cambrian stratigraphy and paleontology: Integrating correlation techniques, paleobiology, taphonomy and paleoenvironmental reconstruction: Palaeoworld, v. 15, p. 217–222.

Zyakun, A.M., Lunina, O.N., Prusakova, T.S., Pimenov, N.V., Ivanov, M.V., 2009, Fractionation of stable carbon isotopes by photoautotrophically growing anoxygenic purple and green sulfur bacteria: Microbiology, v. 78, p. 757-768.

APPENDIX

SUMMARY OF ISOTOPIC DATA

Stratigraphic Unit	Sample No.	Strat. Height	Lithology	$\delta^{13}C$ (‰, VPDB)	σ (‰)	$\delta^{18}O$(‰, VPDB)	TOC%	$\delta^{13}C_{org}$ (‰, VPDB)	Δδ
Section 1: Shingle Pass, Nevada (GPS coordinates: N 38°31'15.44" W 114°58'10.03")									
Emigrant Springs Member B	SP0	0	Bioclastic wackestone	1.79	0.03	-7.51	0.06	-26.64	28.44
Emigrant Springs Member B	SP2	2	Bioclastic wackestone	1.14	0.01	-9.40	0.04	-26.98	28.12
Emigrant Springs Member B	SP4	3.9	Bioclastic wackestone	1.16	0.02	-9.87	0.05	-28.45	29.62
Emigrant Springs Member B	SP6	5.9	Bioclastic wackestone	1.31	0.01	-9.97	0.05	-27.38	28.69
Emigrant Springs Member B	SP7	7.5	Bioclastic wackestone	1.68	0.01	-9.70	0.06	-26.71	28.39
Emigrant Springs Member B	SP10	10	Wavy microbial boundstone	1.36	0.01	-9.54	0.03	-25.62	26.98
Emigrant Springs Member B	SP13	13	Wavy microbial boundstone	1.58	0.01	-9.86	0.04	-26.80	28.38
Emigrant Springs Member B	SP15	15.2	Wavy microbial boundstone	2.56	0.01	-10.26	0.06	-24.95	27.51
Emigrant Springs Member B	SP17	17	Wavy microbial boundstone	1.64	0.01	-9.98	0.03	-26.21	27.85
Emigrant Springs Member B	SP19	19	Wavy microbial boundstone	1.61	0.02	-10.57	0.05	-24.95	26.57
Emigrant Springs Member B	SP20.5	20.6	Wavy microbial boundstone	2.26	0.01	-9.64	0.04	-25.78	28.04
Emigrant Springs Member B	SP21	21.4	Wavy microbial boundstone	2.26	0.02	-10.32	0.04	-25.66	27.92
Emigrant Springs Member B	SP23	23	Thin-bedded grainstone	2.11	0.01	-12.58	0.03	-27.72	29.83
Emigrant Springs Member B	SP25	25	Thin-bedded grainstone	2.17	0.01	-10.50	0.05	-28.51	30.68
Emigrant Springs Member B	SP27	27	Wavy microbial boundstone	1.64	0.02	-9.37	0.03	-24.57	26.21
Emigrant Springs Member B	SP33	32.8	Wavy microbial boundstone	1.40	0.03	-10.08	0.02	-24.89	26.29
Emigrant Springs Member B	SP34	34	Wavy microbial boundstone	1.63	0.05	-10.03	0.02	-24.60	26.23
Emigrant Springs Member B	SP37	37	Thin-bedded grainstone	3.66	0.03	-8.16	0.08	-24.76	28.43
Emigrant Springs Member B	SP40	40.2	Wavy microbial boundstone	2.75	0.01	-9.30	0.04	-25.06	27.81
Emigrant Springs Member B	SP43	43	Wavy microbial boundstone	2.24	0.01	-13.28	0.04	-24.54	26.78
Emigrant Springs Member B	SP58	57.8	Wavy microbial boundstone	3.06	0.01	-8.59	0.04	-24.76	27.82
Emigrant Springs Member B	SP60	60	Wavy microbial boundstone	2.86	0.02	-8.86	0.02	-24.95	27.81
Emigrant Springs Member B	SP62	62.2	Fenestral wackestone	2.79	0.01	-9.50	0.03	-24.04	26.84
Emigrant Springs Member C	SP65	65	Oolitic grainstone	1.66	0.01	-9.40	0.04	-23.83	25.49
Emigrant Springs Member C	SP67	67.2	Oolitic grainstone	3.57	0.02	-12.67	0.07	-23.78	27.35
Emigrant Springs Member C	SP70	70	Oolitic grainstone	3.62	0.03	-9.64	0.04	-24.64	28.25
Emigrant Springs Member C	SP72.9	72.9	Bioclastic grainstone	3.38	0.02	-9.84	0.05	-24.66	28.05
Emigrant Springs Member C	SP74	74.4	Oolitic grainstone	2.64	0.01	-13.44	0.04	-24.73	27.37
Emigrant Springs Member C	SP77	76.6	Oolitic grainstone	3.22	0.01	-9.77		-23.58	26.80
Emigrant Springs Member C	SP80	79.6	Bioclastic grainstone	4.20	0.03	-9.50	0.04	-24.56	28.76
Emigrant Springs Member C	SP82	81.9	Bioclastic grainstone	4.31	0.01	-9.85	0.05	-23.71	28.02
Emigrant Springs Member C	SP84	84	Oolitic grainstone	2.97	0.02	-9.55	0.05	-24.61	27.58

Stratigraphic Unit	Sample No.	Strat. Height	Lithology	$\delta^{13}C$ (‰, VPDB)	σ (‰)	$\delta^{18}O$(‰, VPDB)	TOC%	$\delta^{13}C_{org}$ (‰, VPDB)	Δδ
Emigrant Springs Member C	SP86	86	Oolitic grainstone	3.29	0.01	-9.70	0.03	-23.88	27.17
Emigrant Springs Member C	SP91	90.8	Oolitic grainstone	3.57	0.02	-10.07	0.03	-24.30	27.87
Emigrant Springs Member C	SP93	93	Oolitic grainstone	3.37	0.02	-10.38	0.05	-24.27	27.64
Emigrant Springs Member C	SP95	95	Oolitic grainstone	3.60	0.01	-9.91	0.05	-24.28	27.88
Emigrant Springs Member C	SP97	97	Oolitic grainstone	3.87	0.02	-9.72	0.02	-24.20	28.06
Emigrant Springs Member C	SP99	99	Shelly bioclastic grainstone	4.01	0.03	-9.67	0.04	-24.17	28.18
Emigrant Springs Member C	SP102	102.5	Shelly bioclastic grainstone	4.18	0.01	-9.83	0.04	-24.19	28.36
Emigrant Springs Member C	SP105	104.6	Shelly bioclastic grainstone	4.00	0.02	-9.57	0.05	-23.83	27.83
Emigrant Springs Member C	SP107	107	Shelly bioclastic grainstone	4.24	0.02	-9.66	0.04	-23.78	28.02
Emigrant Springs Member C	SP109	109	Shelly bioclastic grainstone	2.95	1.10		0.05	-24.12	27.07
Emigrant Springs Member C	SP111	111	Bioclastic wackestone	3.71	0.01	-11.45	0.05	-24.16	27.87
Emigrant Springs Member C	SP112	112	Bioclastic wackestone	3.47	0.02	-13.84	0.03	-24.33	27.79
Emigrant Springs Member C	SP113	113.2	Bioclastic wackestone	3.62	0.01	-12.88	0.06	-23.75	27.37
Emigrant Springs Member C	SP115	114.8	Bioclastic wackestone	3.98	0.01	-10.56	0.05	-24.09	28.07
Emigrant Springs Member C	SP117	117	Skeletal grainstone	4.23	0.01	-10.54	0.04	-23.98	28.20
Emigrant Springs Member C	SP119	119	Skeletal grainstone	4.15	0.01	-10.79	0.04	-24.91	29.05
Emigrant Springs Member C	SP121	121	Skeletal grainstone	4.12	0.01	-10.49	0.05	-24.37	28.49
Emigrant Springs Member C	SP123	123	Skeletal grainstone	4.45	0.01	-11.01	0.03	-24.71	29.16
Emigrant Springs Member C	SP125	125	Skeletal grainstone	4.71	0.02	-9.70	0.02	-24.80	29.51
Emigrant Springs Member C	SP127	127	Skeletal grainstone	4.32	0.02	-10.40	0.03	-24.42	28.74
Emigrant Springs Member C	SP130	129.8	Bioclastic grainstone	4.47	0.01	-9.02	0.03	-24.08	28.55
Emigrant Springs Member C	SP132	132	Bioclastic grainstone	3.88	0.02	-9.67			
Emigrant Springs Member C	SP134	134.1	Bioclastic packstone	4.41	0.02	-9.60	0.03	-24.75	29.15
Emigrant Springs Member C	SP136	136.4	Oncoidal/intraclastic grainstone	4.14	0.01	-9.85			
Emigrant Springs Member C	SP139	139	Intraclastic grainstone	4.18	0.01	-9.46	0.05	-25.66	29.84
Emigrant Springs Member C	SP140	140	Intraclastic grainstone	4.27	0.01	-9.51	0.04	-25.61	29.88
Emigrant Springs Member C	SP142	142.2	Oncoidal/intraclastic grainstone	3.74	0.02	-9.38			
Emigrant Springs Member C	SP144	144.3	Intraclastic grainstone	3.91	0.02	-9.77			
Emigrant Springs Member C	SP146	146	Bioclastic grainstone	4.06	0.01	-9.66			
Emigrant Springs Member C	SP148	148	Thin-bedded grainstone	5.30	0.01	-9.65			
Emigrant Springs Member C	SP150	150	Intraclastic grainstone	4.75	0.01	-9.98	0.05	-23.94	28.69
Emigrant Springs Member C	SP152	152	Intraclastic grainstone	4.62	0.02	-9.53	0.05	-23.92	28.53
Emigrant Springs Member C	SP154.5	154.5	Thin-bedded grainstone	5.31	0.01	-10.69	0.05	-24.54	29.84

Stratigraphic Unit	Sample No.	Strat. Height	Lithology	$\delta^{13}C$ (‰, VPDB)	σ (‰)	$\delta^{18}O$(‰, VPDB)	TOC%	$\delta^{13}C_{org}$ (‰, VPDB)	Δδ
Emigrant Springs Member C	SP156	156.6	Thin-bedded grainstone	5.49	0.02	-9.45	0.05	-23.98	29.46
Emigrant Springs Member C	SP157	157.7	Thin-bedded grainstone	5.16	0.02	-10.60	0.09	-23.23	28.39
Emigrant Springs Member C	SP159.5	159.6	Oolitic grainstone	4.73	0.01	-9.49	0.04	-24.29	29.01
Emigrant Springs Member C	SP162	161.9	Oolitic grainstone	4.12	0.03	-9.54	0.03	-24.20	28.32
Emigrant Springs Member C	SP164	164	Oolitic grainstone	5.29	0.01	-7.04	0.03	-23.70	28.99
Emigrant Springs Member C	SP168	168	Oolitic grainstone	4.37	0.01	-9.02	0.05	-24.29	28.66
Emigrant Springs Member C	SP170	170	Oolitic grainstone	4.41	0.01	-9.21	0.04	-24.56	28.97
Emigrant Springs Member C	SP172	172	Oolitic grainstone	4.27	0.02	-9.10	0.05	-24.23	28.50
Emigrant Springs Member C	SP174	173.8	Oolitic grainstone	4.38	0.02	-8.85	0.03	-23.37	27.76
Dunderberg Formation	SP176	176	Bioclastic packstone	4.32	0.02	-9.66	0.03	-24.30	28.62
Dunderberg Formation	SP178	177.8	Bioclastic packstone	3.56	0.01	-8.85	0.02	-22.85	26.41
Dunderberg Formation	SP183	183	Bioclastic wackestone	4.63	0.00	-9.12	0.04	-23.61	28.24
Dunderberg Formation	SP186	186.2	Bioclastic packstone	4.64	0.01	-9.27	0.05	-22.93	27.57
Dunderberg Formation	SP188	188.8	Domal/stromatolitic boundstone	4.16	0.02	-9.81	0.04	-24.32	28.48
Dunderberg Formation	SP190	190	Domal/stromatolitic boundstone	4.46	0.02	-9.47	0.06	-22.18	26.64
Dunderberg Formation	SP192	192	Oncoidal/intraclastic grainstone	5.10	0.04	-7.97	0.03	-23.53	28.63
Dunderberg Formation	SP194	194	Oncoidal/intraclastic grainstone	4.70	0.01	-9.59	0.04	-23.62	28.32
Dunderberg Formation	SP196	196	Oolitic grainstone	4.65	0.02	-10.99	0.04	-23.31	27.96
Dunderberg Formation	SP200	200	Oolitic grainstone	4.48	0.01	-10.72			
Dunderberg Formation	SP202	202	Wavy microbial boundstone	4.47	0.01	-10.10	0.02	-24.69	29.16
Dunderberg Formation	SP206	206	Wavy microbial boundstone	3.42	0.02	-12.41	0.03	-25.35	28.77
Dunderberg Formation	SP209	209	Intraclastic grainstone	3.41	0.02	-9.52	0.05	-26.64	30.06
Dunderberg Formation	SP211	211	Shelly bioclastic grainstone	3.31	0.01	-10.36	0.04	-24.69	28.00
Dunderberg Formation	SP213	213	Bioclastic wackestone	3.85	0.01	-10.53	0.03	-25.32	29.17
Dunderberg Formation	SP222	222	Thin-bedded grainstone	2.69	0.02	-9.29	0.03	-25.88	28.57
Dunderberg Formation	SP225	225	Oolitic grainstone	2.35	0.03	-9.19	0.03	-25.93	28.29
Dunderberg Formation	SP227	227	Oolitic grainstone	2.35	0.02	-9.42	0.02	-25.69	28.04
Dunderberg Formation	SP229	229	Oolitic grainstone	2.20	0.01	-9.97	0.03	-25.61	27.80
Dunderberg Formation	SP232	232.4	Oolitic grainstone	2.13	0.01	-10.26	0.02	-25.67	27.80
Dunderberg Formation	SP234	234	Bioclastic grainstone	1.90	0.02	-9.22	0.03	-24.34	26.24
Dunderberg Formation	SP235	235	Bioclastic wackestone	1.04	0.05	-8.31	0.03	-26.87	27.91
Dunderberg Formation	SP236	236.2	Thin-bedded grainstone	2.01	0.01	-9.10	0.03	-26.03	28.04
Dunderberg Formation	SP237	237.6	Thin-bedded grainstone	1.64	0.02	-9.42	0.03	-25.76	27.39

Stratigraphic Unit	Sample No.	Strat. Height	Lithology	$\delta^{13}C$ (‰, VPDB)	σ (‰)	$\delta^{18}O$(‰, VPDB)	TOC%	$\delta^{13}C_{org}$ (‰, VPDB)	Δδ
Dunderberg Formation	SP239	239.2	Bioclastic wackestone	1.53	0.02	-9.85	0.02	-26.33	27.86
Dunderberg Formation	SP241	241.6	Oolitic grainstone	1.50	0.02	-10.11	0.02	-25.94	27.44
Dunderberg Formation	SP243	243.2	Bioclastic wackestone	0.94	0.02	-9.54	0.03	-25.79	26.73
Dunderberg Formation	SP245	245	Bioclastic packstone	0.80	0.01	-10.02	0.02	-25.59	
Whipple Cave Formation	SP247	247	Bioclastic wackestone	0.12	0.02	-10.94	0.08	-23.84	23.96
Whipple Cave Formation	SP248	248	Bioclastic wackestone				0.01	-26.14	
Whipple Cave Formation	SP249	249	Bioclastic packstone	0.73	0.02	-11.22	0.03	-26.13	26.86
Whipple Cave Formation	SP253	253	Argillaceous wackestone	0.71	0.02	-11.45	0.02	-26.33	27.04
Whipple Cave Formation	SP255	255	Argillaceous wackestone	0.19	0.02	-10.54	0.02	-26.62	26.81
Whipple Cave Formation	SP259	259	Oolitic grainstone	0.61	0.04	-10.55	0.02	-26.02	26.63
Whipple Cave Formation	SP263	263	Argillaceous wackestone	0.55	0.02	-13.32	0.03	-27.01	27.56
Whipple Cave Formation	SP266	266	Argillaceous wackestone	0.89	0.35	-12.02	0.03	-27.18	28.07
Whipple Cave Formation	SP269	269	Argillaceous wackestone	-0.10	0.04	-13.43	0.02	-26.13	26.03
Whipple Cave Formation	SP271	271	Argillaceous wackestone	1.99	0.09	-9.26	0.02	-26.98	28.97
Whipple Cave Formation	SP273	273	Argillaceous wackestone	0.66	0.06	-11.35	0.02	-25.57	26.23
Whipple Cave Formation	SP275	275	Argillaceous wackestone	1.03	0.10	-9.15	0.02	-26.24	27.28
Whipple Cave Formation	SP277	277	Argillaceous wackestone	0.77	0.02	-9.92	0.02	-28.68	29.44
Whipple Cave Formation	SP279	279	Wavy microbial boundstone	0.80	0.01	-10.11	0.03	-27.52	28.33
Whipple Cave Formation	SP281	281	Wavy microbial boundstone	1.32	0.06	-9.40	0.04	-28.48	29.81
Whipple Cave Formation	SP284	284	Wavy microbial boundstone	0.41	0.03	-10.16	0.02	-26.17	26.58
Whipple Cave Formation	SP286	286	Wavy microbial boundstone	0.81	0.02	-10.86	0.03	-26.91	27.72
Whipple Cave Formation	SP290	290	Wavy microbial boundstone	0.60	0.03	-14.19	0.02	-26.22	26.82
Whipple Cave Formation	SP295	295	Wavy microbial boundstone	1.28	0.02	-9.01	0.03	-26.86	28.13
Whipple Cave Formation	SP300	300	Wavy microbial boundstone	0.44	0.05	-9.26	0.03	-26.59	27.03
Section 2: House Range, Utah (GPS coordinates: N 39°11'56.47" W 113°18'54.07")									
Big Horse Limestone	HR121	121	Oolitic grainstone	0.61	0.01	-9.84	0.08	-27.22	27.83
Big Horse Limestone	HR122	122	Bioclastic wackestone	0.35	0.02	-9.00	0.03	-23.77	24.12
Big Horse Limestone	HR126	126	Skeletal grainstone	0.40	0.02	-9.78	0.04	-25.16	25.57
Big Horse Limestone	HR127	127.4	Bioclastic packstone	0.20	0.01	-10.03	0.06	-25.93	26.13
Big Horse Limestone	HR129	128.7	Bioclastic packstone	0.63	0.02	-9.64	0.03	-26.15	26.78
Big Horse Limestone	HR130	130	Shelly bioclastic grainstone	0.62	0.02	-10.08	0.04	-26.25	26.88

Stratigraphic Unit	Sample No.	Strat. Height	Lithology	$\delta^{13}C$ (‰, VPDB)	σ (‰)	$\delta^{18}O$(‰, VPDB)	TOC%	$\delta^{13}C_{org}$ (‰, VPDB)	Δδ
Big Horse Limestone	HR132	132	Shelly bioclastic grainstone	0.64	0.03	-9.91	0.05	-26.47	27.11
Big Horse Limestone	HR134	133.8	Bioclastic wackestone	0.57	0.03	-9.95	0.03	-26.79	27.36
Big Horse Limestone	HR136	136	Bioclastic wackestone	0.79	0.02	-9.81	0.03	-25.60	26.39
Big Horse Limestone	HR138	138	)omal/stromatolitic boundston	0.79	0.02	-9.29			
Big Horse Limestone	HR141	140.7	Intraclastic grainstone	1.10	0.02	-9.57			
Big Horse Limestone	HR143	142.9	Intraclastic grainstone	0.69	0.02	-10.18			
Big Horse Limestone	HR145	145	Oolitic grainstone	0.32	0.02	-10.39	0.04	-25.96	26.27
Big Horse Limestone	HR147	146.9	Oolitic grainstone	0.60	0.02	-9.92	0.03	-25.98	26.58
Big Horse Limestone	HR148	148.3	Oncoidal packstone	0.74	0.03	-10.31	0.04	-23.94	24.68
Candland Shale	HR150	149.9	Intraclastic grainstone	1.13	0.01	-9.58	0.03	-24.75	25.87
Candland Shale	HR152	152	Shelly bioclastic grainstone	1.19	0.02	-9.65	0.05	-26.83	28.02
Candland Shale	HR154	153.3	Intraclastic grainstone	1.23	0.01	-9.53	0.03	-27.29	28.53
Candland Shale	HR156	155.7	Oolitic grainstone	1.39	0.02	-9.57	0.03	-25.38	26.77
Candland Shale	HR157	156.4	Bioclastic wackestone	1.45	0.01	-9.74	0.06	-25.68	27.13
Candland Shale	HR161	161	Bioclastic grainstone	2.01	0.02	-9.51	0.04	-24.08	26.09
Candland Shale	HR163	163.4	Bioclastic packstone	1.87	0.01	-9.35	0.10	-23.69	25.56
Candland Shale	HR165	165.4	Bioclastic wackestone	2.24	0.01	-9.44	0.05	-25.12	27.36
Candland Shale	HR167	167.3	Bioclastic wackestone	2.21	0.03	-9.57	0.05	-25.63	27.84
Candland Shale	HR168	168.5	Shaly mudstone	4.00	0.01	-9.40	0.03	-24.17	28.17
Candland Shale	HR171	170.8	Bioclastic wackestone	3.46	0.01	-9.77	0.06	-25.21	28.67
Candland Shale	HR175	175.2	Bioclastic wackestone	2.43	0.02	-9.90	0.05	-24.74	27.17
Candland Shale	HR178	178	Oncoidal packstone	2.73	0.01	-9.74	0.06	-25.03	27.76
Candland Shale	HR180	180	Bioclastic grainstone	2.41	0.00	-9.99	0.05	-23.76	26.17
Candland Shale	HR183	182.9	Bioclastic wackestone	3.00	0.02	-10.77	0.07	-25.14	28.14
Candland Shale	HR186	186	Bioclastic wackestone	2.62	0.02	-10.41	0.04	-24.80	27.42
Candland Shale	HR187	187.1	Bioclastic wackestone	2.55	0.01	-10.41	0.03	-24.65	27.20
Candland Shale	HR189	188.9	Skeletal packstone	2.96	0.01	-10.65	0.04	-24.10	27.05
Candland Shale	HR191	191.5	Shaly mudstone	2.87	0.02	-10.74	0.02	-24.86	27.73
Candland Shale	HR192	192.3	Bioclastic packstone	3.06	0.02	-10.80	0.03	-25.68	28.74
Candland Shale	HR195	195	Calcareous shale				0.09	-24.98	
Candland Shale	HR200	200.2	Bioclastic wackestone	1.97	0.02	-10.44	0.06	-25.20	27.17
Candland Shale	HR202	202.1	Intraclastic grainstone	1.76	0.02	-10.79	0.05	-25.13	26.90

Stratigraphic Unit	Sample No.	Strat. Height	Lithology	$\delta^{13}C$ (‰, VPDB)	σ (‰)	$\delta^{18}O$(‰, VPDB)	TOC%	$\delta^{13}C_{org}$ (‰, VPDB)	Δδ
Candland Shale	HR205	205.1	Skeletal grainstone	2.98	0.02	-9.75	0.04	-24.39	27.37
Candland Shale	HR212	211.8	Bioclastic packstone	2.79	0.03	-10.45	0.03	-24.84	27.63
Candland Shale	HR213	212.8	Bioclastic packstone	2.70	0.01	-10.77	0.10	-25.05	27.75
Candland Shale	HR220	220	Bioclastic wackestone	2.66	0.01	-10.39			
Candland Shale	HR224	223.8	Intraclastic grainstone	3.20	0.02	-10.65	0.02	-25.67	28.86
Candland Shale	HR228	228	Oncoidal packstone	3.78	0.01	-10.07	0.05	-22.43	26.21
Candland Shale	HR229	229	Bioclastic wackestone	3.54	0.01	-10.49	0.06	-25.20	28.74
Candland Shale	HR231	231.4	Skeletal packstone	4.35	0.02	-10.33	0.03	-24.90	29.25
Candland Shale	HR233	233	Skeletal packstone	3.71	0.01	-9.54	0.03	-23.89	27.61
Candland Shale	HR236	236	Bioclastic wackestone	5.24	0.01	-10.25	0.06	-23.92	29.15
Candland Shale	HR238	237.5	Bioclastic wackestone	5.47	0.01	-10.57	0.04	-22.90	28.37
Candland Shale	HR244	243.5	Bioclastic packstone	4.16	0.01	-10.10	0.04	-25.05	29.21
Candland Shale	HR252	252	Skeletal grainstone	4.67	0.01	-9.85			
Candland Shale	HR254	254	Bioclastic wackestone				0.02	-25.83	
Candland Shale	HR257	257	Bioclastic wackestone	5.05	0.03	-10.09	0.06	-25.04	30.09
Candland Shale	HR258	257.7	Oncoidal packstone	5.41	0.01	-9.96	0.05	-23.49	28.90
Candland Shale	HR260	260	Oncoidal packstone	4.54	0.02	-9.78	0.06	-25.12	29.66
John's Wash Limestone	HR262	262	Bioclastic wackestone	5.06	0.02	-10.29	0.05	-24.47	29.54
John's Wash Limestone	HR263	263.2	Oolitic packstone	4.13	0.01	-10.22	0.05	-24.88	29.01
John's Wash Limestone	HR265	264.9	Oolitic grainstone	5.23	0.02	-10.45	0.03	-24.43	29.66
John's Wash Limestone	HR267	267	Oolitic grainstone	5.32	0.01	-10.35			
John's Wash Limestone	HR268	267.9	Oolitic grainstone	5.00	0.02	-10.62	0.07	-24.37	29.36
John's Wash Limestone	HR269	268.9	Oolitic grainstone	5.41	0.01	-10.16	0.04	-24.43	29.84
John's Wash Limestone	HR270	270	Oolitic grainstone	4.92	0.02	-10.47	0.07	-24.80	29.73
John's Wash Limestone	HR272	271.8	Oolitic grainstone	4.39	0.02	-10.47	0.05	-23.75	28.14
John's Wash Limestone	HR274	273.9	Oolitic grainstone	4.12	0.01	-10.30	0.08	-21.30	25.43
John's Wash Limestone	HR276	275.9	Oolitic grainstone	4.43	0.01	-9.99	0.03	-23.82	28.25
John's Wash Limestone	HR277	277.3	Oolitic grainstone	4.19	0.01	-10.39	0.02	-25.78	29.97
John's Wash Limestone	HR279	279	Intraclastic grainstone	4.36	0.04	-10.63	0.03	-23.76	28.12
John's Wash Limestone	HR281	280.8	Intraclastic grainstone	4.32	0.02	-11.58	0.03	-24.74	29.06
John's Wash Limestone	HR282	282	Oolitic grainstone	4.11	0.02	-12.59	0.03	-25.64	29.76
John's Wash Limestone	HR283	283.5	Oolitic grainstone	4.84	0.01	-10.19	0.03	-23.90	28.74

Stratigraphic Unit	Sample No.	Strat. Height	Lithology	$\delta^{13}C$ (‰, VPDB)	σ (‰)	$\delta^{18}O$(‰, VPDB)	TOC%	$\delta^{13}C_{org}$ (‰, VPDB)	Δδ
John's Wash Limestone	HR285	284.9	Oolitic grainstone	4.37	0.02	-10.32	0.03	-24.22	28.59
John's Wash Limestone	HR285.5	285.5	Oncoidal wackestone	4.12	0.02	-10.22	0.04	-24.19	28.31
John's Wash Limestone	HR288	287.8	Oolitic grainstone	4.47	0.01	-9.72	0.03	-24.89	29.36
John's Wash Limestone	HR290	288.9	Skeletal grainstone	3.79	0.07	-10.64	0.02	-24.08	27.86
John's Wash Limestone	HR293	293	Bioclastic wackestone	3.92	0.05	-12.88	0.04	-22.52	26.44
John's Wash Limestone	HR299	299.2	Wavy microbial boundstone	4.23	0.01	-9.72	0.03	-23.81	28.03
John's Wash Limestone	HR304	303.8	Wavy microbial boundstone	4.54	0.95		0.02	-24.74	29.28
John's Wash Limestone	HR307	306.9	Wavy microbial boundstone	4.27	0.03	-9.69	0.04	-25.58	29.85
John's Wash Limestone	HR312.5	312.5	Wavy microbial boundstone	4.28	0.01	-9.52	0.02	-24.14	28.42
John's Wash Limestone	HR315	314.6	Wavy microbial boundstone	4.16	0.01	-8.74	0.02	-23.66	27.82
John's Wash Limestone	HR315.5	315.4	Shelly bioclastic grainstone	2.19	0.03	-10.09	0.02	-24.33	26.52
John's Wash Limestone	HR316	315.2	Oncoidal wackestone	2.19	0.02	-10.12	0.03	-24.24	26.43
Corset Springs Shale	HR324	323.5	Bioclastic wackestone	0.91	0.06	-10.99	0.03	-25.04	25.95
Corset Springs Shale	HR325	324.9	Bioclastic wackestone	0.94	0.01	-10.89	0.03	-23.49	24.43
Corset Springs Shale	HR326	326	Bioclastic wackestone	1.02	0.01	-10.83	0.02	-24.84	25.86
Corset Springs Shale	HR328	328.2	Bioclastic wackestone	0.96	0.05	-10.86		-24.58	25.54
Corset Springs Shale	HR330	329.7	Shelly bioclastic grainstone	0.90	0.04	-10.85	0.02	-25.75	26.65
Corset Springs Shale	HR332	331.8	Bioclastic packstone	-0.09	0.03	-9.14	0.02	-24.93	24.84
Corset Springs Shale	HR337	336.6	Bioclastic wackestone	1.14	0.41	-10.61	0.04	-25.51	26.65
Corset Springs Shale	HR339	338.5	Bioclastic wackestone	1.07	0.03	-10.60	0.03	-25.83	26.90
Corset Springs Shale	HR340	340	Skeletal packstone	0.89	0.02	-10.31	0.04	-25.69	26.57
Corset Springs Shale	HR341	341	Skeletal packstone	1.03	0.01	-10.05	0.03	-25.72	26.75
Corset Springs Shale	HR343	343.2	Bioclastic/oncoidal wackeston	0.67	0.15	-10.15			
Corset Springs Shale	HR345	345	Bioclastic/oncoidal wackeston	0.76	0.03	-10.34	0.04	-24.72	25.48
Corset Springs Shale	HR346	346	Bioclastic/oncoidal wackeston	0.94	0.02	-9.87	0.04	-26.67	27.61
Corset Springs Shale	HR349	349	Bioclastic/oncoidal wackeston	0.73	0.02	-9.56	0.03	-25.13	25.85
Corset Springs Shale	HR351	351	Wavy microbial boundstone	0.65	0.03	-9.45	0.04	-23.54	24.18
Corset Springs Shale	HR355	355	Wavy microbial boundstone	0.44	0.39	-10.15	0.03	-24.38	24.82
Corset Springs Shale	HR357	357	Bioclastic/oncoidal wackeston	0.24	0.59	-10.18	0.02	-25.26	25.51
Corset Springs Shale	HR360	360	Bioclastic/oncoidal wackeston	0.39	0.02	-9.71	0.02	-24.34	24.73
Corset Springs Shale	HR363	363	Bioclastic/oncoidal wackeston	0.59	0.02	-9.62	0.03	-25.47	26.06
Corset Springs Shale	HR366	366	Bioclastic/oncoidal wackeston	0.55	0.02	-9.49	0.03	-25.23	25.79

Stratigraphic Unit	Sample No.	Strat. Height	Lithology	$\delta^{13}C$ (‰, VPDB)	σ (‰)	$\delta^{18}O$(‰, VPDB)	TOC%	$\delta^{13}C_{org}$ (‰, VPDB)	Δδ
Corset Springs Shale	HR368	368	Bioclastic/oncoidal wackeston	0.58	0.01	-9.30	0.02	-24.48	25.06
Sneakover Limestone	HR370	370	Oncoidal wackestone	0.21	0.02	-9.35	0.03	-25.96	26.17
Sneakover Limestone	HR372	372	Wavy microbial boundstone	0.35	0.02	-9.20	0.02	-25.78	26.13
Sneakover Limestone	HR374	374	Wavy microbial boundstone	0.51	0.02	-8.96	0.04	-20.09	20.59
Sneakover Limestone	HR376	376	Wavy microbial boundstone	0.47	0.02	-9.21	0.03	-25.49	25.96
Sneakover Limestone	HR378	378	Wavy microbial boundstone	0.40	0.02	-9.39	0.03	-25.98	26.38
Sneakover Limestone	HR379	379	Wavy microbial boundstone	0.24	0.03	-9.61			
Sneakover Limestone	HR380	380	Wavy microbial boundstone	0.16	0.01	-9.79	0.04	-24.96	25.12
Sneakover Limestone	HR381	381	Bioclastic/oncoidal wackeston	1.05	0.02	-9.13	0.04	-25.90	26.95
Sneakover Limestone	HR383	382.8	Bioclastic/oncoidal wackeston	1.91	0.02	-11.10	0.03	-25.20	27.11
Sneakover Limestone	HR385	384.8	Wavy microbial boundstone	1.11	0.01	-9.39	0.02	-24.19	25.31
Sneakover Limestone	HR387	387	Wavy microbial boundstone	2.90	0.01	-4.30	0.04	-26.33	29.23
Sneakover Limestone	HR390	390	Wavy microbial boundstone	1.24	0.02	-8.09	0.05	-26.46	27.70
Sneakover Limestone	HR393	392.8	Bioclastic wackestone	1.15	0.02	-8.88	0.03	-25.89	27.04
Sneakover Limestone	HR396	396	Wavy microbial boundstone	1.12	0.01	-8.79	0.04	-23.81	24.92
Sneakover Limestone	HR398	398	Bioclastic wackestone	1.38	0.02	-8.81	0.03	-24.70	26.08
Sneakover Limestone	HR401	400.8	Wavy microbial boundstone	1.14	0.02	-9.06	0.05	-23.20	24.34
Sneakover Limestone	HR404	404.2	Bioclastic wackestone	1.10	0.03	-11.47	0.02	-25.69	26.79
Sneakover Limestone	HR406	406	Wavy microbial boundstone	1.24	0.01	-9.59	0.03	-24.97	26.22
Sneakover Limestone	HR408	408	Wavy microbial boundstone	1.05	0.02	-9.27	0.03	-25.14	26.19
Sneakover Limestone	HR412	412.2	Wavy microbial boundstone	1.45	0.01	-8.83	0.02	-25.29	26.74
Sneakover Limestone	HR420	420	Wavy microbial boundstone	1.25	0.01	-9.15	0.03	-25.26	26.51
Sneakover Limestone	HR424	424	Bioclastic wackestone	0.51	0.01	-9.26	0.05	-29.53	30.03
Sneakover Limestone	HR426	426	Bioclastic packstone	0.85	0.01	-8.94	0.05	-26.18	27.03
Sneakover Limestone	HR428	428	Wavy microbial boundstone	0.63	0.02	-8.81	0.03	-26.26	26.89
Sneakover Limestone	HR432	432	Bioclastic wackestone	1.37	0.02	-7.68	0.05	-26.31	27.68
Sneakover Limestone	HR434	434	Wavy microbial boundstone	0.75	0.01	-9.06	0.05	-26.49	27.24
Sneakover Limestone	HR438	438	Wavy microbial boundstone	1.15	0.02	-8.90	0.03	-25.19	26.34
Sneakover Limestone	HR444	444	Bioclastic wackestone	1.23	0.01	-8.96	0.03	-26.28	27.52
Sneakover Limestone	HR448	448	Bioclastic/oncoidal wackeston	1.19	0.02	-8.98		-32.06	33.26
Sneakover Limestone	HR455	455	Bioclastic wackestone	1.84	0.02	-8.94	0.04	-27.51	29.35
Sneakover Limestone	HR460	460	Bioclastic wackestone	1.01	0.02	-8.76	0.03	-25.20	26.21

VITA

Graduate College
University of Nevada, Las Vegas

Jonathan Lloyd Baker

Degrees:

Bachelor of Science, Geology, 2008
Weber State University

Publications:

Baker, J., Jiang, G., Zeiza, A., 2010, Carbon isotopic fractionation across a late Cambrian carbonate platform: a regional response to the SPICE event as recorded in the Great Basin, United States: Geological Society of America Abstracts with Programs, v. 42, p. 44.

Barwick, C., Baker, J., Jenkins, J., Hawkins, K., Waite, C., 2008, Faunal analysis of five nonmarine microvertebrate localities, Late Cretaceous, southern Utah: Geological Society of America Abstracts with Programs, v. 40, p. 69.

Thesis Title: Carbon isotopic fractionation across a late Cambrian carbonate platform: a regional response to the SPICE event as recorded in the Great Basin, United States

Thesis Examination Committee:

Chairperson, Ganqing Jiang, Ph. D.
Committee Member, Matthew Lachniet, Ph. D.
Committee Member, Rodney Metcalf, Ph.D.
Graduate Faculty Representative, Peter Starkweather, Ph. D.